

CZECH TECHNICAL UNIVERSITY IN PRAGUE  
FACULTY OF ELECTRICAL ENGINEERING  
DEPARTMENT OF ELECTROMAGNETIC FIELD



# New Microwave Components for Distance and Imaging Measurement

---

DOCTORAL THESIS BY ALEKSANDRA BASKAKOVA

Ph.D. PROGRAMME: ELECTRICAL ENGINEERING AND  
INFORMATION TECHNOLOGY [P2612]  
BRANCH OF STUDY: RADIOELECTRONICS [2601V010]

SUPERVISOR: prof. Ing. KAREL HOFFMANN, CSc.  
CO-SUPERVISOR: doc. Ing. PŘEMYSL HUDEC, CSc.

APRIL 2022



---

## **Declaration of Originality**

I, the undersigned, hereby declare that I have written this doctoral thesis independently and quoted all the sources of information used in accordance with methodological instructions on ethical principles for writing an academic thesis. The thesis was written under the professional supervision of Prof. Karel Hoffmann, using the literature and resources listed in the References.

In Prague, 2022

.....  
Mgr. Aleksandra Baskakova

---

## **Acknowledgement**

I sincerely would like to thank my supervisor professor Karel Hoffmann for his bright ideas, continued support in my research and all the career opportunities he opened up for me. Many thanks also belong to my colleagues from the Department of Electromagnetic Field. It was a great pleasure to work alongside such responsive, talented and intelligent people.

With grateful regards I thank my friends Alexander Glubokov, Andreas Wentzel and Leslie Francis Ryan for their time and advice on my publications. I also would like to thank Dr. Vratislav Sokol, Dr. Milan Prihoda and Dr. Jan Eichler for sharing their outstanding experience in electromagnetic simulations with me.

Last but not least, I would like to thank my wonderful family and my boyfriend Alexander for their endless support and encouragement. I dedicate this work to my beloved grandfather Anatoly N. Sidorov.

---

# Abstract

The thesis focuses on the design of microwave components for accurate distance and high-resolution imaging measurement which can be utilized in a number of applications in the automotive, mechanical engineering, and robotics industries.

Novel sensors for ultrashort-distance measurement in the X- and W- bands have been designed, fabricated and experimentally verified. The fundamental problematic of reflection measurements in the near-field zone of an antenna has been solved using specific choke flanges applied at the open ends of the R100 and WR10 waveguides, as well as a circular waveguide, featuring a radius of 1.42 mm. Field distributions between the sensors and a target have been analyzed and explained on the basis of higher order modes of a radial line formed by the sensors and a planar reflective target. A robust equivalent circuit using a cascade of lossy waveguides is proposed and a new calibration/correction method is derived. The new sensors make possible to achieve about ten times smaller distance measurement errors in comparison with the state-of-the-art sensors.

The sensor based on the WR10 waveguide with a choke flange is successfully used in W-band imaging. Due to the developed calibration/correction method, the sensor can deliver contrast of imaging greater than 26 dB, and spatial resolution of 1.9 mm at a 2-mm standoff distance, which is better than parameters of state-of-the art sensors.

For the characterization of materials with greater spatial resolution based on the scanning microwave microscopy a new interferometric sensor using multistage sections of microstrip lines and resistors and working in the frequency band 45 MHz – 26 GHz is proposed. The sensor can be further improved utilizing coupled lines instead of sections of microstrip lines. An original four-port component, dual-mode impedance transformer was developed for this concept. The component enables to achieve deeper interferometric minima in a wider frequency band. After solving of technological problems with the thin resistive layer application it can be applied for further development of the interferometric sensor.

## Key Words

Distance measurement, microwave measurement, mm-wave measurement, waveguide sensor, mm-wave imaging, interferometry, impedance matching, transformer, scanning microwave microscopy

---

# Abstrakt

Tato práce je zaměřena na návrh součástí v pásmu mikrovln a mm vln pro přesné měření vzdálenosti a zobrazování s vysokým rozlišením, což může být využito v řadě aplikací v automobilovém i strojírenském průmyslu a robotice.

Jsou navrženy vyrobeny a experimentálně ověřeny nové senzory pro měření ultrakrátkých vzdáleností pracující v pásmech X a W. Hlavní problém měření koeficientu odrazu v blízkém poli antény je vyřešen použitím speciální tlumivkové příruby na otevřeném konci vlnovodu R100 a WR10 a kruhového vlnovodu s poloměrem 1,42 mm. Rozložení pole mezi senzorem a terčem je analyzováno a vysvětleno pomocí vyšších vidů v radiálním vedení tvořeným senzorem a rovinným odrazným terčem. Je navržen robustní náhradní obvod tvořený kaskádou ztrátových vlnovodů a je odvozena nová kalibračně/korekční metoda. Tato metoda umožňuje dosáhnout desetkrát menší chyby v měřené vzdálenosti v porovnání s dosud známými senzory.

Senzor s vlnovodem WR10 a tlumivkovou přírubou je úspěšně použit pro zobrazování v pásmu W. Díky vyvinuté kalibračně/korekční metodě umožňuje senzor dosáhnout kontrastu zobrazení většího než 26 dB a prostorového rozlišení 1,9 mm při vzdálenosti vzorku 2 mm, což je lepší než parametry dosud známých senzorů.

Pro charakterizaci materiálů s větším prostorovým rozlišením pomocí skenovacího mikrovlnného mikroskopu byl navržen nový interferometrický senzor. používající vícestupňové sekce mikropáskových vedení a rezistorů a pracující ve frekvenčním pásmu 45 MHz – 26 GHz. Senzor může být dále vylepšen použitím vázaných vedení místo sekcí mikropáskových vedení. Je navržena a experimentálně ověřena nová součástka typu čtyřbran, dvojvidový impedanční transformátor, umožňující tento koncept. Tato součástka umožňuje dosáhnout hlubších interferenčních minim v širším kmitočtovém pásmu. Po zvládnutí technologických problémů s nanášením tenké odporové vrstvy může být použita při dalším vývoji interferometrického senzoru.

## Klíčová Slova

Měření vzdálenosti, mikrovlnné měření, měření mm-vlny, vlnovodný senzor, mm-vlnové zobrazování, interferometrie, impedanční přizpůsobení, transformátor, skenovací mikrovlnná mikroskopie



# Contents

	<b>Page</b>
<b>1 Introduction</b>	<b>1</b>
<b>2 State-of-the-Art</b>	<b>5</b>
2.1 Distance Measurement . . . . .	5
2.2 Imaging Measurement . . . . .	9
2.3 Scanning Microwave Microscopy . . . . .	12
<b>3 Objectives of the Thesis</b>	<b>15</b>
<b>4 Achieved Results</b>	<b>17</b>
4.1 Investigation of Waveguide Sensors for Ultra-Short-Distance Measurements	19
4.2 Novel Waveguide Sensors for Contactless Ultrashort-Distance Measurements	24
4.3 W-Band Imaging Sensor Using a Rectangular Waveguide Structure With Choke . . . . .	36
4.4 An Interferometric Sensor for Scanning Microwave Microscopy Application	41
4.5 Design of Microstrip Dual-Mode Impedance Transformers . . . . .	45
4.6 Advanced Configuration of the Interferometric Sensor . . . . .	49
<b>5 Conclusion</b>	<b>53</b>
<b>References</b>	<b>55</b>
<b>Author's Publications</b>	<b>59</b>
<b>Curriculum Vitae</b>	<b>60</b>







# Abbreviations

AD	Analog-to-digital converter
AWR	Advancing the Wireless Revolution
CST	Computer Simulation Technology
CW	Continuous Wave
DSP	Digital Signal Processing
EDM	Electronic Distance Measurement
EM	Electromagnetic
FET	Field Effect Transistors
FMCW	Frequency Modulated Continuous Wave
IF	Intermediate Frequency
IoT	Internet of Things
Q-factor	Quality Factor
RF	Radio Frequency
SFCW	Stepped Frequency Continuous Wave
SMD	Surface-Mount Device
SMM	Scanning Microwave Microscopy
SNR	Signal-to-Noise Ratio
SSS	Triple Offset Shorts
SUT	Sample under Test
VNA	Vector Network Analyzer
VWG	Virtual Waveguide



Technical and technological progress does not stand still, but rather introduces new inventions to a variety of industries and fields of application. The Fourth Industrial Revolution or Industry 4.0 [1] with its global automation of traditional manufacturing and industrial practices is surging at the moment. The concept of Industry 4.0 includes manufacturing digitization, advanced robotics, internet of things (IoT), and demands the employment of modern smart technologies and solutions. As a result, operational frequency bands are expanding, non-conventional materials are starting to be utilized, and demands on the accuracy of standards are increasing. All these factors indicate the need to develop new microwave and mm-wave devices and techniques for more accurate measurements of certain system and material parameters.

Nowadays, industrial production devices, such as those in the automotive industry or rolling mills, demand highly precise, small distance measurements to control the manufacturing process and to inspect final products to assure top quality. These measurements can be applied in material properties measurement [2], microwave imaging [3], and mechanical engineering to measure not only distances of mechanical components, but also their surface deformations or vibrations.

The design of a non-contacting measurement system, for short or ultrashort-distance measurements, is a fundamental task. In principle, these measurements correspond to the measurement of the reflection coefficients of targets placed in a near-field zone of a measurement device, such as an antenna or sensor. This kind of measurement suffers from one drawback. The parameters of the antenna change due to the presence of the target close to the antenna resulting in strongly nonlinear dependence of the measured phase on the target distance. Those non-linear near-field effects corrupt the measured signal and increase the distance determination error.

Some techniques for such measurements in optics exist. However, distance sensors should not only measure precisely, but also be adapted for industrial environments where dust surrounds a target. Therefore, a laser solution is not suitable.

Moreover, modern car manufacturing processes include robotics with various sensors located on one platform. It is important that distance sensors can coexist with other sensors without causing interference. That can be achieved by designing them on the least occupied frequency bands.

---

Development of a mm-wave solution, while eliminating the non-linear effects, is highly advantageous and will solve all limitations arising in a particular application.

As mentioned above, such sensors can be applied not only in distance measurements, but also in imaging use. Near-field imaging is widely utilized for many biological, as well as industrial, applications, such as noninvasive sensing, the characterization of biological samples [4], material characterization [5], the detection of surface defects [6], the evaluation of different surfaces [7],[8],[9], the inspection of composite materials [10], etc. In the microwave and mm-wave region, near-field imaging is an accurate tool which does not require special measurement conditions and is hazard-free.

One particular application of near-field imaging features new automotive radar systems operating at 76–81 GHz [11] for detecting the speed and range of objects in the vicinity of a car. The radar antennas are located behind a plastic bumper, or the nameplate of the producer, often in the form of the corporate logo. It is important to measure the bumper or the nameplate properties to determine their impact on the radar antenna radiation patterns. Nowadays, it can be measured, approximately, with a far-field approach using a vector network analyzer (VNA) with two horn antennas and lenses. However, a proper near-field mm-wave imaging sensor would be more advantageous as it provides local properties of the obstacles.

Moreover, a correction/calibration method can be developed and applied to make the measurements simpler and more precise. It enables measurement uncertainties to be suppressed and provides a high-contrast of the image and high spatial resolution.

On the other hand, decreasing the dimensions of electronic devices into the nanoscale brings traditional materials to their applicable limits. Materials based on nanostructures are starting to be commonly used. Due to their special properties, they utilize a wide range of applications such as optics, electronics, material application, nanotechnology etc. One promising application is to use such materials in field effect transistors (FET) or in heterojunction diodes.

New materials and device structures based on nanostructures require precise broadband measurement and imaging of their electromagnetic properties. However, the impedances of these materials are much larger than the conventional reference impedance of a measurement system (usually 50  $\Omega$ ) which leads to the problem of mismatching and poor accuracy of measurement.

Generally, imaging sensors are unable to detect details not smaller than the shortest side of their aperture. For imaging of tiny parts or nanostructures, a near-field probe must be used.

Scanning microwave microscopes consist of a near-field probe and a microwave measurement system which makes it possible to determine the impedance between the tip of the probe and a scanned sample. The distance between the tip and the sample is much smaller than the wavelength of the electromagnetic field and the field confines in space

close to the tip of the probe. Therefore, the technique provides high spatial resolution [12].

This doctoral thesis focuses on the development of new microwave and mm-wave circuits, components and techniques for the precise measurement of distances in a near-field zone from a reflective surface, high-contrast imaging of metal/dielectric samples and the scanning of extremely high-impedance materials.

In the first part of the doctoral thesis, state-of-the-art distance, imaging and scanning microwave microscopy (SMM) measurements are presented in [chapter 2](#) and describe modern solutions for measurements with different approaches and calibration techniques. The objectives of the thesis are given in [chapter 3](#). Then, the thesis core is demonstrated in [chapter 4](#) by a collection of journal papers presenting a description of their contributions and relevance to the thesis topic. At the end, the achieved results, conclusions and future research topics are summarized in [chapter 5](#).



In this chapter an overview of different approaches for distance, imaging measurements and scanning microwave microscopy are presented. A synopsis of correction/calibration techniques for increasing the accuracy of measurements is introduced. Major challenges of the measurement techniques are discussed.

## 2.1 Distance Measurement

Distance (length) is one of the oldest measures that humans use. Historically it began with measurements using parts of the human body such as the foot, from which the British and American units of length originated. Much later, in the middle of the 20th century, the first electronic distance measurement (EDM) instrument based on visible light and, later, on microwave radiation, was introduced. Nowadays there are a great number of distance measurement devices which can detect distance from sub-atomic to astronomical scales.

Despite this, challenges still exist and the need for accurate non-contact measurements of distance of mechanical components, surface deformations, or vibration has become critical.

A number of techniques enable the use of contactless distance measurement, including some for accurate distance measurement utilizing ultrasonic systems [13] or inductive sensors [14]. Usually, ultrasonic distance sensors are readily available with a wide measuring distance range. Nevertheless, they have a blind range for distances close to the sensor itself, which does not allow the correct determination of short distances. On the other hand, measurement results of inductive sensors are dependent on the material of the target. Ferromagnetic or non-ferromagnetic materials influence the frequency of the sensor oscillator differently. These sensors are not generic.

There are a few techniques for the accurate distance measurement proposed in the optical region using laser sensors [15], [16]. These can perform noncontact distance measurement with high resolution. However, the drawback of such systems is that the laser utilized does not penetrate the smoke, dust, or flying debris which can surround a target. To overcome this problem microwave or millimeter wave sensors can be used.

The distance of reflective objects in the microwave and millimeter wave regions can be determined by several different methods. Generally, the base principle of the measurement

is founded by defining a phase of the reflection coefficient reflected from the target, see [Figure 2.1](#), where a corresponding standing wave is displayed. The dependence of distance over the phase is linear and can be found as:

$$d = \lambda(\pi - \phi)/4\pi, \quad (2.1)$$

where  $\phi$  is a phase of the measured reflection coefficient of the signal,  $\lambda$  is a wavelength and  $d$  is the distance from the initial point to the target.

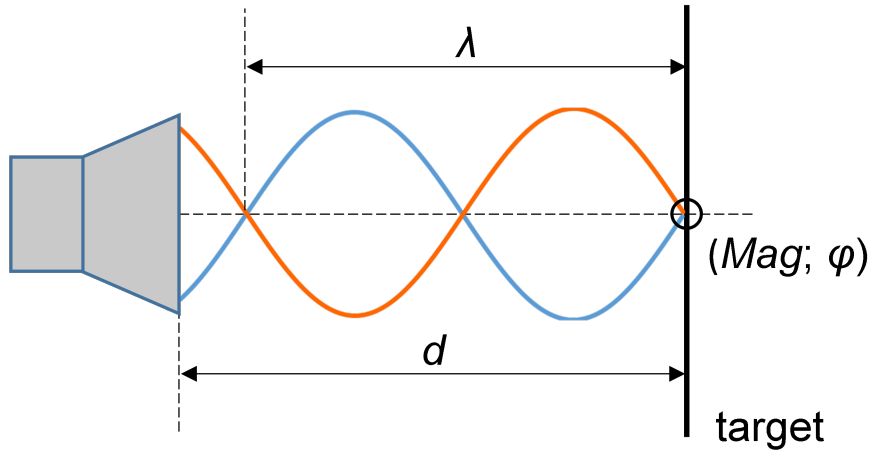


*Figure 2.1: Basic principle of distance determination*

In [\[17\]](#), [\[18\]](#),[\[19\]](#) the authors use the interferometric approach for contactless distance measurement. The precision and sensitivity of such systems are relatively high. However, measurement systems based on the interferometric approach are mostly used for distances of several wavelengths. At greater distances a problem with ambiguity appears and it requires the implementation of a  $2\pi$ -phase correction.

Microwave- and millimeter-wave radars, such as stepped frequency continuous wave (SFCW), frequency modulated continuous wave (FMCW) or single frequency (CW) radars, are used for noncontact measurement tasks for long distance determination. Considering the radar system for distance measurement as a 1-port reflectometer with a horn antenna at the end, the general block scheme is depicted in [Figure 2.2](#) and explained below.

The antenna sends a signal from the source to the object. This signal reaches the object and is reflected back to the antenna. The reflected signal must then be down converted to a baseband by an I/Q-Mixer and sampled. Now the Q-component contains the measured distance information [\[20\]](#).

The system's hardware performance is limited, and the radar signal is often distorted by interfering signals, caused by unwanted reflections, and by a low signal-to-noise ratio (SNR), which causes phase distortion. Since distance measurement is possible if the phase conversion of the system is linear over the whole distance range, one usually applies signal-processing algorithms [\[21\]](#), [\[22\]](#). The more precise the measurement required, the more sophisticated the algorithm applied.



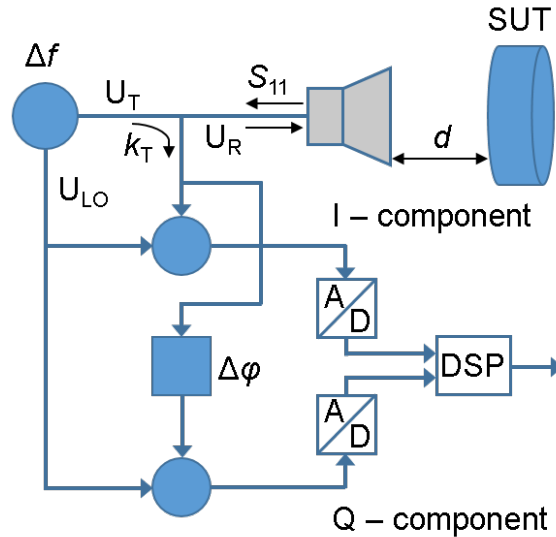


Figure 2.2: Block diagram of a radar system [20]

Moreover, standard antennas, e.g., horn and Vivaldi, are usually utilized in the radars. These antennas have good performance when the reflective target is in a far-field zone. However, nonlinear near-field effects appear when the target is closely spaced to the aperture of an antenna. The parameters of the antenna change due to the presence of the target close to it. The magnitude of a received signal decreases with an increase in distance. A corresponding trace of the measured reflection coefficient in the polar diagram has the shape of a deformed spiral with the center shifted out from the zero point of the diagram. It results in strongly nonlinear dependence of the measured phase on the target distance [20], [23], [24], [25]. Whereas the distance determination error depends on the linearity of the distance/phase relation, it is necessary to use complex calibration/correction methods to determine the distance, including a curve fitting for the spiral [25], [26], see Figure 2.3.

After the correction, distance  $d$  between the target and the antenna can be determined from the phase of the reflection coefficient  $\Gamma$  using the equation from (2.1). Despite the sophisticated correction method, the distance determination error stated in [25] changes in the interval (+0.3 mm, -0.9 mm) for measured distances from 0 mm to 6 mm, which is about  $\frac{1}{2} \lambda_0$ . In accordance with (2.1), at applied frequency 24 GHz, it corresponds to the errors of the measured phase from -17.3 deg to +51.8 deg.

The only publication [24] where a housing of the antenna is applied to correct the signal and reduce measurement errors actually did improve sensor accuracy. However, no physical explanation of the effect nor experimental results are given.

On the other hand, in [27], [28] several free-space calibration techniques for contactless reflection measurement, which corrects the measurement data without using any signal processing, are utilized. Though that kind of calibration is designed for the specific problem of the characterization of dielectric properties of the target, they do not account

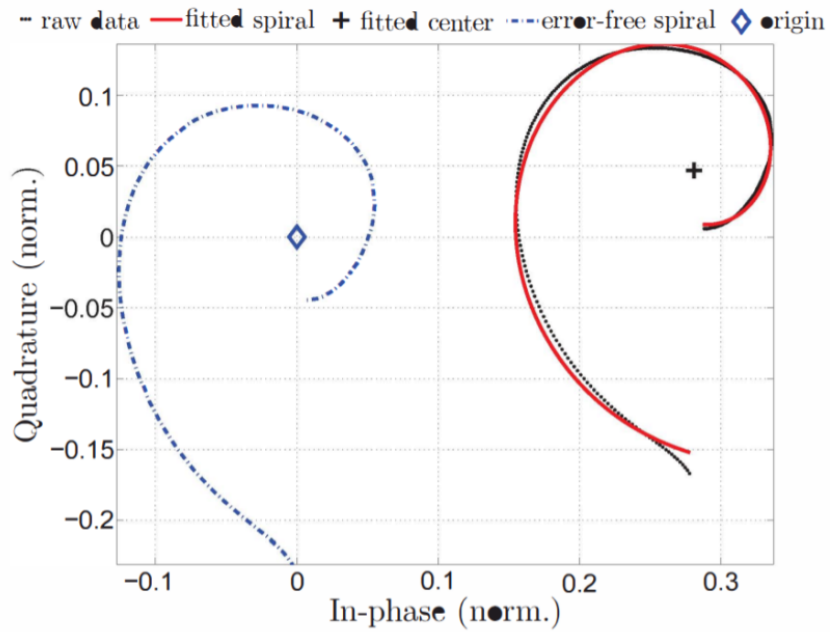


Figure 2.3: Measured (black), fitted (red), and calibrated (blue) spiral of measured data from [25]

for a distance measurement. The development of a correction method for contactless reflection measurement makes the measurement procedure faster and simpler.

Any simple microwave or mm-wave sensor for ultra-short distance measurements with a linear reflection coefficient phase dependence, with respect to the measured distance, has not been designed yet.

## 2.2 Imaging Measurement

The topic of near-field imaging has evolved over the past decades [29]. The imaging setup typically contains a probe, a positioner that holds an sample under test (SUT), and a VNA to determine the S-parameters of the probe, see Figure 2.4. The setup works in the following way: waves emitted by the probe, used to scan the SUT, undergo certain changes when they encounter media interfaces or gaps in the structure. The measured amplitude and phase record the changes and the image is built afterwards.

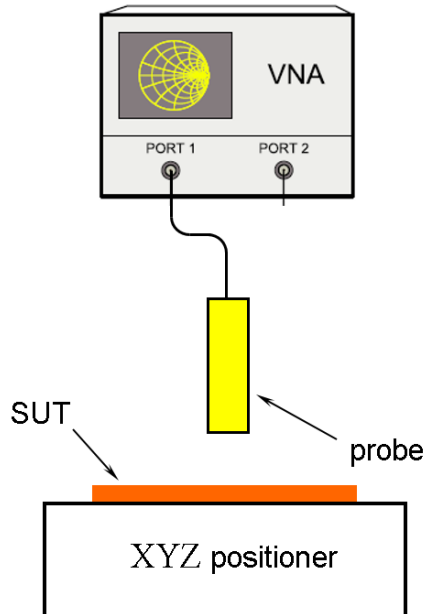


Figure 2.4: Schematic of the imaging setup

The most important parameters of imaging systems are spatial resolution and imaging contrast. Imaging contrast has various definitions. It can be defined as a ratio of the magnitudes or phases of reflection coefficients with different mediums, such as metal and dielectric. In some publications, it is also described as the difference between the reflected signal amplitude and/or the phase between the background and the imaged object [10]. In turn, the spatial resolution determines the sensitivity of the system.

Both parameters, as a rule, ultimately depend on the properties of the probe. Therefore, the probe is the most important part of the measuring system. The more concentrated the electromagnetic field propagating from the probe to the SUT, with the fewest losses, the more imaging information is stored. Thus, the system provides an accurate microwave characterization of the test object.

The first probes used in imaging systems were rectangular waveguides [29] featuring a simple structure that gave acceptable results of the imaging. The imaging resolution of the system is directly related to the wider waveguide side [30], thus, a resolution on the order of a few millimeters requires the use of waveguides at very high frequencies, *e.g.*, the

W-band. However, when studying the problem of imaging sensors, no published research focusing on the 75–110 GHz frequency band could be found. The maximum frequency that was found in the literature was 24 GHz.

Later it was proposed to use circular open-ended waveguide probes to increase the sensitivity of the measuring systems [3]. These probes have more direct field propagation with lower side slopes, which enables better near-field characteristics to be achieved and shows better resolution and contrast in comparison with a conventional rectangular waveguide probe.

Another probe in use is a tapered rectangular waveguide probe [31]. The design of such a probe is the narrow side of a standard rectangular waveguide with dimensions  $a$  and  $b$ , linearly tapering from width  $b$  to width  $d$  along a cone of radial length  $\rho$ , while the wide side  $a$  remains fixed, see Figure 2.5.

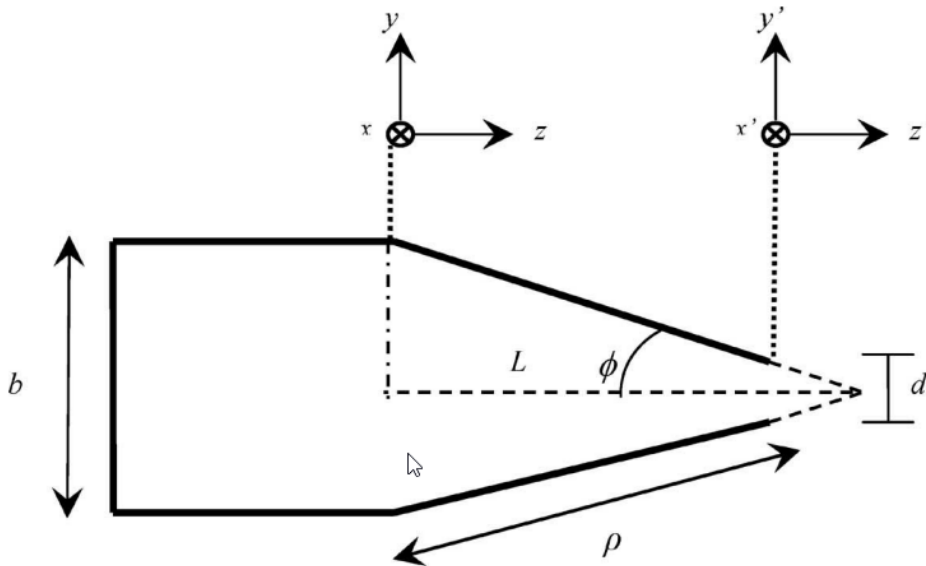


Figure 2.5: Cross section of an E-plane tapered waveguide probe [31]

Considering that the size of the aperture is reduced, the probe’s footprint gets accordingly smaller. Therefore, the resolution of the probe becomes higher. It has been discovered by means of computing that the real power of the tapered waveguide probe is more concentrated toward an SUT when compared to a standard waveguide probe. On the other hand, the sidelobe level fractionally increases.

Another practical taper approach implemented in laboratories is to cut the edges of the waveguide aperture at an angle to reduce the flange area. This approach improves the probe’s performance at high frequencies due to fewer multi-reflection interactions between the flange of the probe and the SUT.

There are also dual-polarized probes utilized for the detection of orientation targets highly dependent on electric field, such as cracks, highly conductive inserts, disbonds and

concrete or composite structural damages [6], [7]. These probes generate two sets of data for two orthogonal polarizations and enable the monitoring of polarized targets regardless of their orientation.

The tip of an open-ended coaxial cable can be used as a probe for imaging, a so-called apertureless probe [32], [33], [34], which provides high spatial resolution of the imaging. However, the standoff distance is extremely limited, almost touching the object of interest. The imaging contrast is, likewise, poor.

In general, all imaging sensors can be divided into two groups: resonant and non-resonant. Resonant nearfield sensors [9], [10] use resonant probes with dimensions of  $0.01 \div 0.2 \lambda_0$  (free space wavelength), thereby making it difficult to scale up to very high frequencies, e.g., the W band. All the probes discussed above are non-resonant and are not constrained by the scaling limitation [3], [7], although standoff distances around  $0.08 \lambda_0$  are relatively small and can bring misalignment problems at higher frequencies. Moreover, in both types of sensors, the obtained image does not provide realistic information regarding the local amplitudes of the reflection coefficients of the SUT and their ratios (contrasts).

Despite all the studies [3], [10], [31] of imaging probes or systems, it is difficult or impossible to predict field behavior, or even to characterize it using mathematical equations or analytical formulas. There is no way for the correction or calibration to be applied to improve system performance. Moreover, no studies about the best standoff distance to SUT can be found.

## 2.3 Scanning Microwave Microscopy

To scan extremely small areas, those much smaller than a waveguide probe is capable of scanning, and to detect incredibly tiny parts, a scanning microwave microscope can be utilized.

In general, scanning microwave microscopes consist of a near-field probe and a microwave measurement system which makes it possible to determine the impedance between the tip of the probe and a scanned sample. The distance between the tip and the sample is much smaller than the wavelength of the electromagnetic field and the field confines in space close to the tip of the probe. Therefore, the technique provides high spatial resolution [13].

The direct measurement of extremely high impedances using the tip connected to a standard 50  $\Omega$  VNA results in poor accuracy [35]. The reason is clearly described by a well-known relation between reflection coefficient and corresponding impedance  $Z$  (see Figure 2.6):

$$\Gamma = \frac{Z - Z_0}{Z + Z_0}, \quad (2.2)$$

where  $Z_0$  is equal to the characteristic impedance of the VNA.

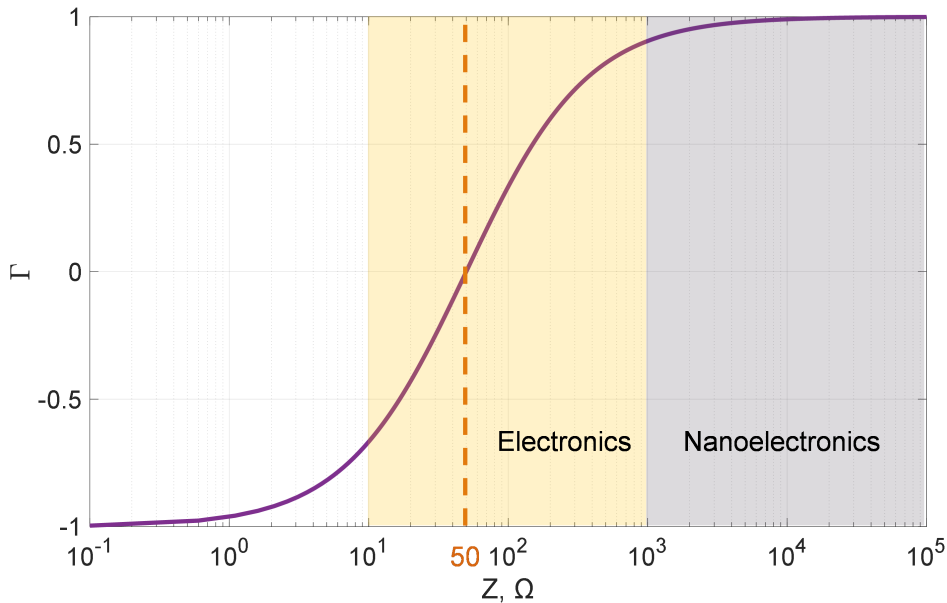


Figure 2.6: Impedance over reflection coefficient dependence

The measured reflection coefficient is not sensitive to changes of the impedance value in this case. Therefore, the magnitude value approaches unity in the area of interest. To overcome this problem, several methods have been proposed over the last few decades that shift high reflection coefficients to better measurable lower values.

Some of the first designs used a critically coupled half wavelength resonator with the tip probe connected to one end [36], [37]. In [38] a half wavelength resonator is

connected in parallel to a  $50 \Omega$  load. The advantage of these approaches is that the resonant loop passes close to the resonant frequency around the center of the Smith chart. VNA reflection measurements are, then, possible with low uncertainties due to the high Q-factor of the resonators. However, the use of resonators results in several limitations on the frequency band of operation. Moreover, resonators exhibit a high-unloaded Q-factor that decreases significantly in the presence of the material under test. The resonant loop changes in size and moves away from the center of the Smith chart or condenses the frequency scale.

There are other methods simplifying the reflection coefficient measurement based on an interferometric approach. The idea is that a measured high reflection coefficient is decreased by adding an out-of-phase reflection coefficient with a similar amplitude coming from the reference impedance. This technique was suggested in [39] for extreme impedance measurement and applied to scanning microwave microscopes in [40] using a Wilkinson power divider. Very low amplitudes of  $\Gamma_R$  reflection coefficients measured by the VNA can be achieved:

$$\Gamma_R = \frac{1}{2}(\Gamma_\chi + \Gamma_{ref}), \quad (2.3)$$

where  $\Gamma_\chi$  corresponds to the reflection coefficient of the tip and  $\Gamma_{ref}$  corresponds to a reference reflection coefficient which is out of phase with respect to  $\Gamma_\chi$  and with a similar amplitude.

However, considering  $\Delta\Gamma_R$ , a measurement uncertainty of the reflection measurement of the VNA due to noise,  $\Delta\Gamma_\chi$  uncertainties of  $\Gamma_\chi$  are determined using (2.3):

$$\Delta\Gamma_\chi = 2\Delta\Gamma_R. \quad (2.4)$$

The uncertainty of the reflection coefficient of tip  $\Delta\Gamma_\chi$  is twofold higher than the measurement uncertainty  $\Delta\Gamma_R$  of the VNA. Problems with tip impedance  $Z_\chi$  uncertainties determined using (2.2), therefore, remain.

The interferometric approach can be also applied on transmission measurements. The first frequency wide-band designs for extreme impedance measurements were suggested in [41] and [42] (see Figure 2.7). In an ideal case, measured transmission  $T_{21}$  equals:

$$T_{21} = \frac{G}{2}(\Gamma_\chi - \Gamma_{ref}), \quad (2.5)$$

where  $G$  is a linear gain of the amplifier.

The arrangement makes it possible to reduce the uncertainty of reflection coefficient  $\Delta\Gamma_\chi$  of the tip caused by VNA transmission measurement uncertainty  $\Delta T$  due to noise by a factor of  $G/2$ :

$$\Delta\Gamma_\chi = \frac{2\Delta T_{21}}{G}. \quad (2.6)$$

This reduction is limited by a crosstalk corresponding to the  $S_{21}$  parameter of the hybrid coupler between port 1 and port 2.

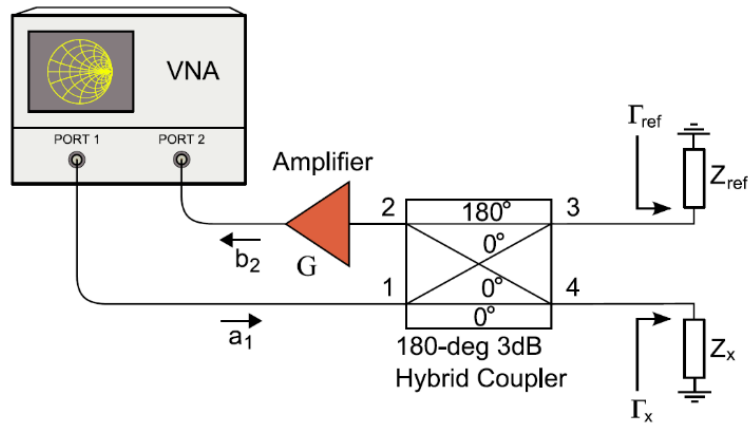


Figure 2.7: Interferometric system for transmission measurement [41]

The concept depicted in Figure 2.7 was adapted for a scanning near-field microwave microscope [43], [44]. Using an impedance tuner, instead of the reference impedance  $Z_{ref}$ , makes it possible to set it so that the crosstalk of the hybrid is eliminated. This enables the potential of the method to reduce uncertainty  $\Delta\Gamma_x$  due to the noise of the VNA being fully utilized. However, the tuner must be set on each frequency of measurement and the settings must have extremely good reproducibility, otherwise the calibration has to be repeated after each setting of the tuner.

In principle, the last two concepts make measurement on any frequency in the frequency band, by the applied components, possible. On the other hand, the two concepts have a rather complex arrangement containing precise variable components with high reproducible settings. Moreover, they enable measurement only at one frequency after calibration.



## Objectives of the Thesis

The main goal of the research is the development of new microwave circuits and components for two important applications: precise contactless near-field distance measurement and high-contrast imaging, including the scanning microwave microscopy technique. The measurement systems for these purposes consist of a VNA connected to a sensor.

The main fundamental challenge for the near-field distance measurement is that the measured target is located in the vicinity of a sensor which changes the sensor radiation pattern, resulting in the occurrence of nonlinear near-field effects and the corruption of the measured signal leading to greater measurement errors.

To improve the contrast and sensitivity of an imaging system, the development of a calibration technique suppressing the reflection coefficient of the sensor itself and enabling not only data to be corrected, but also to be de-embedded to the plane of the SUT required.

For the scanning microwave microscopy application, it is necessary to create a simple, new and compact structure for an interferometric transmission measurement approach. Furthermore, this device should be easy to calibrate and feature good repeatability of measurements.

Therefore, the dissertation thesis has the following main goals:

- To propose a new design of contactless near-field distance sensors using a modified waveguide open in the X-band;
- To refine the designs to the W-band to achieve accuracy of distance determination in the range of micrometers, to analyze field distributions between the sensors and a target, and to find a robust equivalent circuit of this area to derive a new calibration/correction method;
- To fabricate and experimentally verify the new distance sensors applying a post-process for measured signals to obtain corrected results with suppressing measurement errors;
- To apply the distance sensor, based on a rectangular waveguide, with calibration as a high-contrast imaging sensor, and to evaluate the sensor using a planar metal-dielectric SUT;

- 
- To propose a new concept of the system for the measurement of high impedances with a novel interferometric SMM sensor, to analyze field behavior and to detect unwanted coupling;
  - To propose an improved design of the interferometric sensor using coupled lines and a newly developed component: a dual-mode microstrip impedance transformer.

The core of the thesis is based on articles published in peer-reviewed journals with impact factor and in international conference proceedings. The full and original articles with bibliographic citations contributing to the thesis are provided in the following sections.

Section 4.1 presents a design concept of a new contactless precise ultra-short distance sensor based on an R100 open waveguide with a choke flange. It was discovered that the sensor enables a quasi-linear dependence of the measured reflection coefficient phase on the distance to target to be achieved with no ambiguities at selected frequencies. At these frequencies, the field distribution between the sensor and a target is influenced by the choke suppressing the radiated E-field at the edge of the flange. The distances from zero up to more than a half-wavelength can be measured with limited precision.

To increase the resolution to an order of micrometers the design of the sensor is extrapolated to the W-band in section 4.2. Two novel sensors with choke flanges applied at the open ends of a WR10 waveguide and a circular waveguide, featuring a radius of 1.42 mm, are proposed. A robust equivalent circuit using a cascade of lossy waveguides is proposed. A new two-step calibration correction method based on the equivalent circuit is derived which suppresses the influences of the reflection from the sensor itself, multi-reflections between the sensor and the target, variable wavelength in the vicinity of the sensor, and changes in the field configuration when one mode converts into another one. The new sensors make it possible to achieve about ten times fewer distance measurement errors in comparison with state-of-the-art sensors.

Section 4.3 shows a new successful application of the rectangular waveguide distance sensor from section 4.2 for high-contrast imaging in the W-band. Due to the homogeneous field distribution in front of the open-ended sensor, a calibration/correction method, then de-embedding to the plane of the SUT, is applied. Due to this technique, the high-contrast of the image above 26 dB and the correct amplitudes of local reflection coefficients can be determined. The spatial resolution and the minimum resolution for the tracking of SUT local properties of 1.9 mm at 80 GHz are achieved at 2- and 1-mm standoff distances, respectively. The outstanding features of the new sensor surpass the properties of the state-of-the-art sensors.

Section 4.4 proposes a new interferometric transmission measurement approach for

---

scanning microwave microscopy based on a compact circuit structure. The sensor contains multistage sections of microstrip lines and resistors to extend the operational bandwidth of the measuring system. The proposed setup provides deep minima in the interferometric picture, which is a direct demonstration of the high sensitivity of the system. It enables the uncertainty of the reflection coefficient measurements to be reduced about 40 times compared to a standard VNA reflection measurement and allows fast measurements with a VNA intermediate frequency (IF) bandwidth of 30 kHz.

The analysis of the interferometric sensor from [section 4.4](#) shows that its arrangement can be modified by replacing sections of microstrip lines with coupled lines to achieve equally deep minima of the reflection coefficient. However, it is important to reduce all the unwanted reflections of the system, especially any impedance mismatch between coupled lines connected to single-ended microstrip lines. Therefore [section 4.5](#) focuses on the development of a new four-port component, dual-mode impedance transformer for wideband matching of two microstrip lines with equal characteristic impedance and a coupled microstrip line with general even- and odd-mode impedances. A new dimension correction approach is derived. Two transformers between 50  $\Omega$  microstrips and microstrip coupled lines with even/odd impedances 100 /68  $\Omega$  and 36 /27  $\Omega$ , respectively, have been built. The concept is experimentally verified at the frequency band of 0.01–16 GHz.

[Section 4.6](#) is dedicated to the modified configuration of the interferometric sensor for SMM using the new, unique component from [section 4.5](#). As a result of the improvement, the system has a number of measuring frequencies available simultaneously, with the necessity of only one time calibration, and with high resolution. One of the main advantages of the approach is that the sensor is designed on a single substrate with no movable parts. Both interfering signals only propagate inside of the structure. Therefore, the sensor is not sensitive to movements of the interconnecting cables. Unfortunately, in the manufacturing of the sensor, technological difficulties were encountered when applying a thin layer of resistive material between the coupled lines. It turns out that surface resistivity is a demanding technology. Thus, only simulated results with no experimental verification can be shown. The problem can be studied in future research.

## 4.1 Investigation of Waveguide Sensors for Ultra-Short-Distance Measurements

**This chapter is a version of the published manuscript:**

**A. Baskakova**, and K. Hoffmann, “Investigation of Waveguide Sensors for Ultra-Short-Distance Measurements,” in *Proc. of 93rd ARFTG Microwave Measurement Conference (ARFTG)* , 2019, pp. 1–4, doi: 10.1109/ARFTG.2019.8739174.

### **Connection to my Ph.D. thesis:**

Contactless microwave distance measurement in the near-field zone is an important task for industry. A high-precision measurement system that can determine distances of mechanical components, as well as their surface deformations, or vibrations in a production environment is in high demand. The main challenge of such a system emerges from a natural reason: the non-linear dependence of the phase of the reflection coefficient on the distance to the target in the near-field. Therefore, an experimental study of an R100 open waveguide, with a choke flange at the end newly applied as a sensor for ultrashort distance measurements, was conducted. Properties of the sensors were measured in the frequency band from 8 GHz to 12.4 GHz for distances of a reflective target from 0 mm up to 20 mm. It was discovered that the phase-over-distance dependence has a quasi-linear behavior, thus the sensor can successfully measure distances from zero to more than one half of the wavelength.

# Investigation of Waveguide Sensors for Ultra-Short-Distance Measurements

Aleksandra Baskakova, Karel Hoffmann

Czech Technical University in Prague, Czech Republic

**Abstract** — Experimental study of two R100 open waveguides with a plain and a choke flanges at the ends newly applied as sensors for ultra-short distance measurements is presented. Properties of the sensors were mapped by measuring their reflection coefficients in the frequency band from 8 GHz to 12.4 GHz for distances of a reflective target from 0 mm up to 20 mm. Quasi-linear dependence of the phase of the measured reflection coefficient on the distance to the target was discovered at certain frequencies for both sensors. The sensors enable to measure the distances from zero to more than a half of the wavelength.

**Index Terms** — distance measurement, microwave measurement, millimeter wave measurement, sensors.

## I. INTRODUCTION

Different microwave and mm-wave radar systems have been used for decades for navigation and searching in number of military and civil engineering as well as for research in space. Nowadays they are more and more applied in automotive industry for a distance, direction or speed determination. The application of radar systems is wide; from low-cost simple systems like door openers, non-contact hand washers, up to more elaborated systems for tank level gauges, and sophisticated system for multi target search and identification.

Measurement of material parameters in free space is another task for radar systems. Vector network analyzer (VNA) is used for these purpose, and different calibration/correction methods are applied. In all these applications the measured targets are supposed to be in the far field zone of the antennas, in distances at least of several wavelengths.

On the other hand, there are also demands for measurements of reflection coefficients of targets placed in ultra-short distances. That measurements can have applications in material properties measurement, [1], microwave imaging, [2], and mechanical engineering to measure not only distances of mechanical components, but also their possible vibrations.

In principle, these measurements correspond to measurement in near field zone of an antenna, [3]. However, that kind of measurement suffers from several drawbacks. Parameters of the antenna change due to the presence of the target close to the antenna. The magnitude of a received signal exponentially decreases with the increasing of the distance. A corresponding trace of the measured reflection coefficient in the polar diagram has a shape of a deformed spiral with the center shifted out from the zero point of the diagram. It results in strongly nonlinear dependence of the measured phase on the target distance. Whereas the distance determination error depends on the

linearity of the distance/phase relation, it is necessary to use complex calibration/correction methods to determine the distance, including a curve fitting for the spiral [3], [4]. After the correction a distance  $d$  between the target and the antenna can be determined from the phase of the reflection coefficient  $\Gamma$  using a well-known equation

$$d = \frac{\lambda_0}{4\pi} (\pi - \arg \Gamma), \quad (1)$$

where  $\lambda_0$  is a free space wavelength.

Despite the sophisticated correction method, the distance determination error stated in [3] changes in the interval (+0.3 mm, -0.9 mm) for measured distances from 0 mm to 6 mm, which is about  $\frac{1}{2} \lambda_0$ . In accordance to (1), at applied frequency 24 GHz it corresponds to errors of the measured phase from -17.3 deg to +51.8 deg.

It should be emphasized that with respect to the phase measurement, an amplitude of the reflection should be above about 0.5 to reduce measurement uncertainties of the VNA, [5]. Any radiation of the structure antenna plus target reducing the amplitude reflection coefficient below 0.5 therefore increases uncertainty of the distance determination.

Linear dependence of the measured phase with respect to the distance of the target is advantageous, and does not require any complex calibration/correction method. Any simple microwave or mm-wave sensor for ultra-short distance measurements with linear reflection coefficient phase dependence with respect to the measured distance, and simultaneously with its amplitude of above 0.5 has not been designed yet.

In the paper, an experimental study of the distance measurement using linear phase/distance dependence sensors based on an open waveguide with a standard flange, and with a standard flange and a waveguide choke is presented.

## II. EXPERIMENTAL INVESTIGATION

The experimental investigation of two sensors for ultra-short-distance measurements was proceeded at frequency band 8-12.4 GHz. R 100 waveguides with a standard plain flange and a standard flange with a waveguide choke at their ends were used as the sensors, see Fig. 1. Both sections of waveguides had identical lengths.

The measurement set up, consisting of a VNA Agilent E8364A connected to the sensor and a target – metal sheet placed on a precise micrometric positioner, is depicted in Fig. 2. The width of the target formed by a section of radiator is

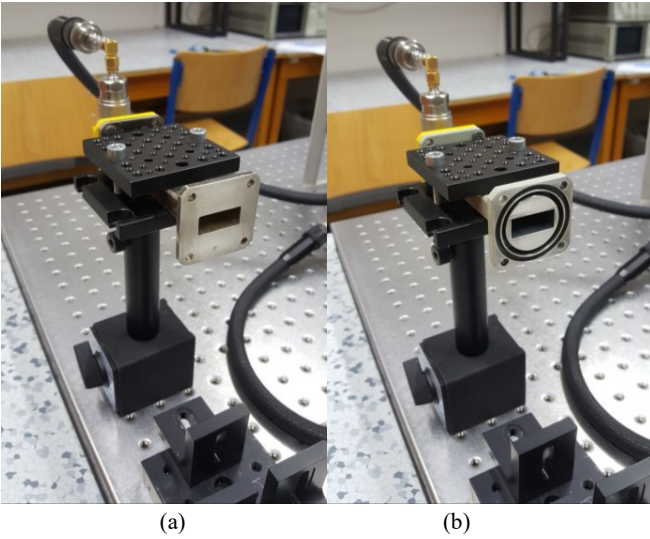


Fig. 1. Sensors for ultra-short distance measurement in the test fixture with a standard plain flange (a) and with a choke flange (b).

112 mm. Calibration of the system was realized at the reference plane of the flange without a choke using TRL method. The test fixture holding waveguides was covered with an absorber material to decrease possible multiple reflections.

The reflection coefficient for both sensors was measured at distances from 0 mm up to 20 mm with a step 0.5 mm in frequency band from 8 GHz up to 12.4 GHz. The measured sets of data are displayed in Fig. 3 with a distance step 4 mm. Each curve corresponds to  $S_{11}$  in the reference plane for different distances from the target.

The uncertainty of the VNA increases for the amplitudes of signals lower than 0.5. Apparently, for the sensor with the flange with a choke there are reasonably high amplitudes for more measuring distances in comparison to the sensor with the plain flange. However, both sensors can be potentially used for distance measurement at some suitable operating frequency.

A schematic with a switch was arranged in NI AWR to determine proper operating frequencies for both sensors. The measured data were consequently processed using a sweep over the distances of the target. Both sets of the measured data were

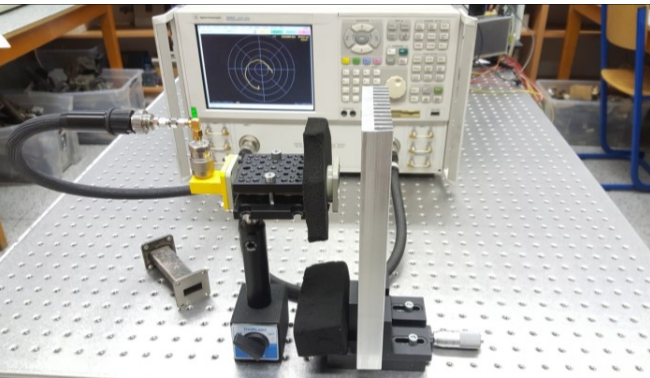
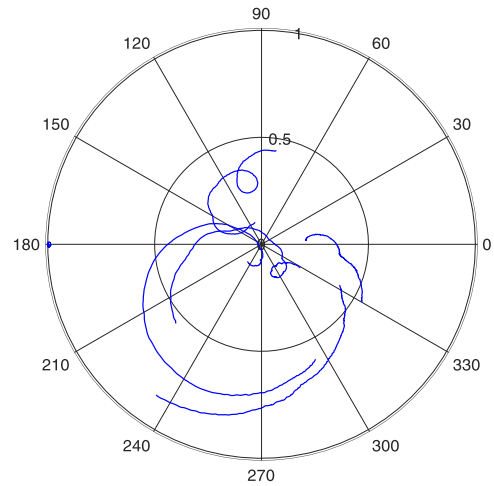
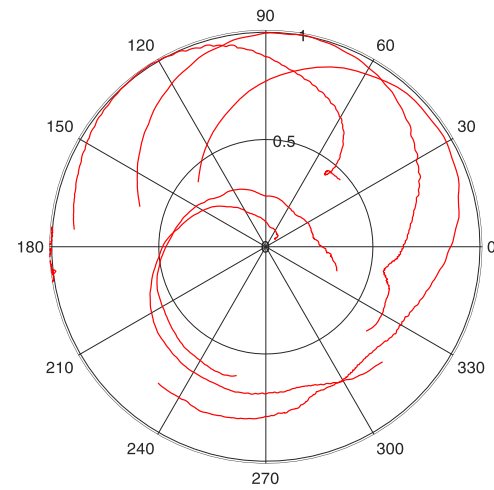


Fig. 2. The experimental setup.



(a)



(b)

Fig. 3. Measurement results for the sensors with a plain (a) and with a choke (b) flange. Distances from 0 mm to 20 mm, step 4 mm.

analyzed on selected frequencies in the interval 0–20 mm. The best results with respect to acceptable values of the reflection coefficient amplitude and linearity of its phase over distance dependence were found, see Fig. 4 and Fig. 5.

The best phase dependence for the sensor with a plain flange close to the linear one was found at frequency 12.4 GHz. The distances from 0.5 mm up to 12.5 mm which corresponds to  $0.54 \lambda_0$ , can be distinguished in this case, see Fig. 5(a). In this interval the trace has no loop, which results in no ambiguity in determination of the distance, see Fig. 4(a). However, with respect to VNA measurement uncertainties the amplitude above 0.5 is only in the intervals from 0.5 mm to 3.5 mm, and from 7.5 mm to 13 mm. In the interval between 3.5 and 7.5 mm the amplitude is lower than 0.5 with its minimum around 0.4. It can be still considered as applicable, but some degradation of measurement uncertainty should be expected. The phase deviation from the linear trace, which is depicted in Fig. 5 with dotted line, is from +12 deg to -17 deg. It corresponds from +0.4 mm to -0.57 mm error in the distance determination.

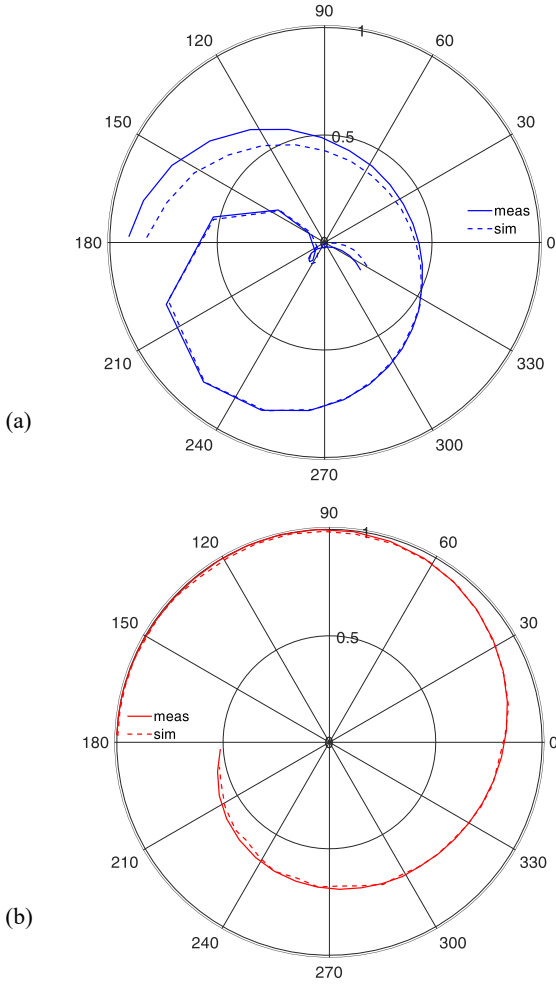


Fig. 4.  $S_{11}$  of the sensors with a plain flange at 12.4 GHz (a) and with a choke flange at 8.9 GHz (b) as a function of the target distance.

The most linear dependence of the phase on the distance for the sensor based on the flange with a choke was achieved at frequency 8.9 GHz and is depicted in Fig. 5(b). In the whole measured interval, the phase dependence on the distance curve is close to the linear one. Moreover, the amplitude is also reasonably high in the whole distance range from 0 mm up to 20 mm corresponding to  $0.59 \lambda_0$  at 8.9 GHz. There is no ambiguity in the relation between the phase and the distance as well, see Fig. 4(b). The phase deviation from the linear trace is from 0 to 12 deg. It corresponds to maximum 0.56 mm error in the distance determination. In comparison with the results from [1], this new sensor has significantly smaller phase error and smaller distance error even though it works at less than half frequency and no correction is applied. Moreover the sensor using the choke flange enables to measure ultra-short distances with higher precision than the sensor with the plain flange.

The physical explanation of properties of both new sensors is discussed in the section below.

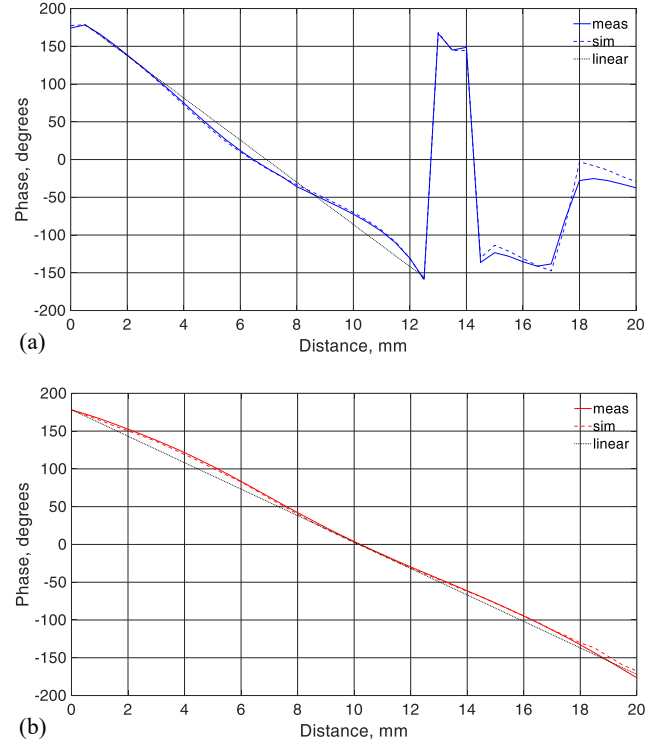


Fig. 5. Phase of the reflection coefficient of the sensors with a plain flange at 12.4 GHz (a) and with a choke flange at 8.9 GHz (b) as a function of the target distance.

### III. DISCUSSION OF THE SENSORS PROPERTIES

The demonstrated results of experimental mapping of the sensors' properties might be influenced by some residual systematic measurement errors. Therefore, both sensors were designed and simulated in CST Studio Suite to verify the measured data. The results of simulations (dashed lines) in comparison with the measured results (solid lines) are depicted in Fig. 4 and Fig. 5. The corresponding results are in a good agreement.

Simulations in CST Studio Suite were also used to get deeper understanding of the physical background of the structures. The propagation of E-field was analyzed for both sensors at the frequencies of interest. Corresponding pictures for the target distances 1 mm, 5 mm and 17 mm are shown in Fig. 6. It can be clearly observed that the radiation from the sensor based on the plain flange is bigger than from the sensor with the flange with a choke. The radiated E-field at the edge of the flange with a choke is about 30 dB suppressed compared to its maximum inside of the waveguide even for the distance of the target 17 mm. Contrarily, corresponding E-field suppression for the sensor with the plain flange is approximately 15 dB at the same distance. The difference can be explained by the choke influence.



For the sensor with the plane flange the field outflows even for very small distances between the flange and the metallic plane target. That happens because the flange and the target form the parallel plate line, and the field radiates at the end of the line.

The different field propagation was observed in the sensor with the flange with a choke. The distance from the center of the wider wall of the waveguide to the bottom of the choke notch is about  $\frac{1}{2}$  of the wavelength, therefore the choke forms a short in the planes of the wider waveguide walls. This effect has been used for many decades in high power waveguide systems where plain flanges are connected to flanges with the choke.

Measurements and simulations confirmed that the choke works acceptably well even when the second plane flange is substituted by the distant plane reflective target. In fact, the choke notch creates a very high impedance at its input, which significantly suppresses the current flow across the notch. That prevents propagation of the field between the flange and the target to the sides of structure. In other words, the choke forms some kind of a virtual waveguide as an extension of the metallic waveguide with a flexible length corresponding to the distance to the target. That effect is well demonstrated in Fig. 6 for distances 1 mm and 5 mm of the metal target.

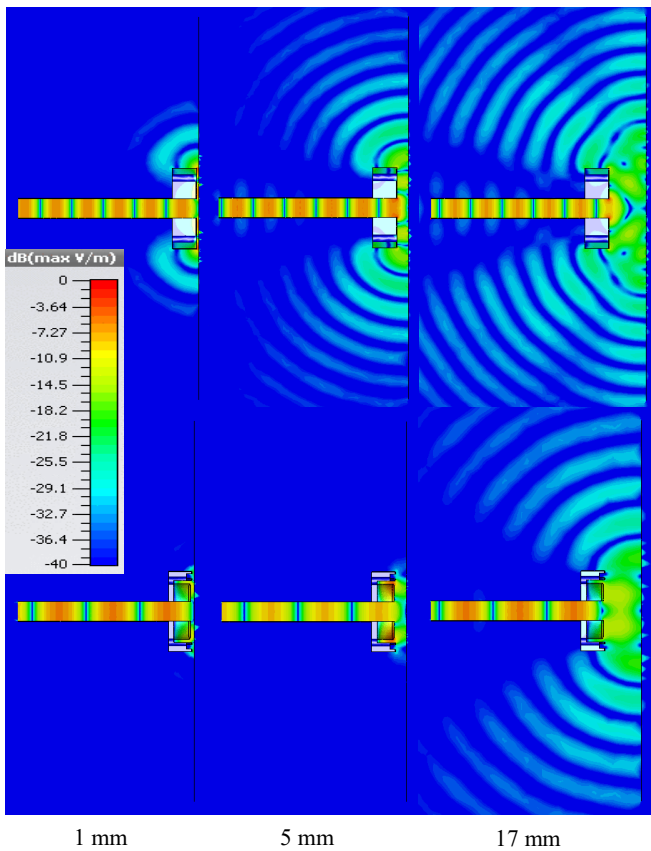


Fig. 6. Propagation of E-field in the sensors with a plain (top row) and a choke (bottom row) flanges.

Increasing the distance to the target the propagated field leaks more, and the amplitude of the reflection coefficient degrades. Nevertheless, the sensor described in [1] provides amplitudes of the reflection coefficient from 0.25 down to 0.05 for distances between 0 mm and 6.6 mm. The new sensor with the choke provides amplitude greater than 0.5 for distances from 0 mm up to 20 mm and the sensor with the plane flange provides amplitude above 0.4 for distances from 0.5 mm to 12.5 mm. Investigated sensors are very advantageous for ultra-short distance measurements application.

#### IV. CONCLUSION

Two sensors based on R 100 waveguides with a standard plain and a choke flanges for contactless ultra-short distance measurement application were experimentally investigated in the frequency band from 8 GHz to 12.4 GHz. Both sensors at selected frequencies enable to achieve a quasi-linear dependence of the measured reflection coefficient phase on the distance to target with no ambiguities. The distances from zero up to more than a half wavelength can be measured. The sensor using the open waveguide with the standard flange with the choke enables to achieve from 4 to 10 times greater value of amplitude of the measured reflection coefficient in comparison with sensors known up to now for the same measured distances. The results can be extrapolated to different frequencies up to mm wave bands, waveguide dimensions and target distances.

#### ACKNOWLEDGEMENT

This work was supported by the European Union's Horizon 2020 research and innovation programme 2016-2020 under the Marie Skłodowska-Curie grant agreement No. 675683.

#### REFERENCES

- [1] Kempin, Matthew Alan, "Design and analysis of an open-ended waveguide probe for material characterization" (2013). *Masters Theses*. 5437. [http://scholarsmine.mst.edu/masters\\_theses/5437](http://scholarsmine.mst.edu/masters_theses/5437).
- [2] M. R. Ramzi, M. Abou-Khousa and I. Prayudi, "Near-Field Microwave Imaging Using Open-Ended Circular Waveguide Probes," in *IEEE Sensors Journal*, vol. 17, no. 8, pp. 2359-2366, 15 April 15, 2017.
- [3] S. Linz, F. Lurz, M. Sporer, S. Lindner, S. Mann, Robert Weigel, and Alexander Koelpin, "Ultra-short-range, precise displacement measurement setup with a near field slot-line antenna and a dedicated spiral calibration," *2015 IEEE MTT-S International Microwave Symposium*, Phoenix, AZ, 2015, pp. 1-4.
- [4] K. Haddadi, M. M. Wang, D. Glay and T. Lasri, "A 60 GHz Six-Port Distance Measurement System with Sub-Millimeter Accuracy," in *IEEE Microwave and Wireless Components Letters*, vol. 19, no. 10, pp. 644-646, Oct. 2009.
- [5] Technical Specifications Agilent Technologies PNA Series Network Analyzers E8362A, E8363A, and E8364A, Available: <https://literature.cdn.keysight.com/litweb/pdf/5989-1072ENUS.pdf?id=450959>.

## 4.2 Novel Waveguide Sensors for Contactless Ultrashort-Distance Measurements

**This chapter is a version of the published manuscript:**

**A. Baskakova**, and K. Hoffmann, “Novel Waveguide Sensors for Contactless Ultrashort-Distance Measurements,” in *IEEE Transactions on Microwave Theory and Techniques*, vol. 70, no. 1, pp. 565–575, Jan. 2022, doi: 10.1109/TMTT.2021.3107503.

**Connection to my Ph.D. thesis:**

After discovering a sensor design with a distinct field distribution directed towards the target, with suppressed radiation at the edge of the flange with a quasi-linear phase-over-distance dependence, the design was rescaled to the W-band to achieve error in distance determination in the order of microns. Two novel sensors for ultrashort-distance measurements, with choke flanges applied to the open ends of both a WR10 waveguide and a circular waveguide, featuring a radius of 1.42 mm, were fabricated. To minimize the measurement errors, a new calibration/correction method based on homogeneous electromagnetic (EM) field propagation between the sensors and a target was derived. The new circular waveguide sensor operates in a frequency band of 75-76 GHz with a maximum error of measured distance 19  $\mu\text{m}$ . The new rectangular waveguide sensor enables the use of an outstanding applicable frequency bandwidth from 76 up to 86 GHz, with best properties around 80 GHz where the maximum error of the measured distance is 12  $\mu\text{m}$ .

# Novel Waveguide Sensors for Contactless Ultrashort-Distance Measurements

Aleksandra Baskakova<sup>1b</sup> and Karel Hoffmann<sup>1b</sup>, *Senior Member, IEEE*

**Abstract**—Novel sensors for ultrashort-distance measurements, with choke flanges applied at the open ends of both a WR10 waveguide and a circular waveguide, featuring a radius of 1.42 mm, are proposed. Field distributions between the sensors and a target are analyzed and explained on the basis of higher order modes of a radial line formed by the sensors and a planar reflective target. A robust equivalent circuit using a cascade of lossy waveguides is proposed and a new calibration/correction method is derived. Properties of both sensors are verified experimentally for target distances of 0–6 mm (more than one and half of wavelength). The new circular waveguide sensor operates in a frequency band of 75–76 GHz with a maximum error of measured distance 19  $\mu\text{m}$ . The new rectangular waveguide sensor enables to use an outstanding applicable frequency bandwidth from 76 up to 86 GHz, with best properties around 80 GHz, where the maximum error of the measured distance is 12  $\mu\text{m}$ . The new sensors make possible to achieve about ten times smaller distance measurement errors in comparison with the state-of-the-art sensors.

**Index Terms**—Correction method, distance measurement, microwave measurement, millimeter-wave (mm-wave) measurement, waveguide sensor.

## I. INTRODUCTION

NOWADAYS, industrial production devices, such as those in the automotive industry or rolling mills, demand highly precise, small distance measurements to control the manufacturing process, and inspect final products to assure top quality. Consequently, contactless distance measurements of mechanical components, surface deformations, or vibrations have become critically important.

A number of techniques can be used for distance measurements, including some for the accurate distance measurement proposed in optical regions using laser sensors [1], [2]. These can perform noncontact distance measurements with high resolution. However, the drawback of such systems is that the laser beam utilized problematically penetrates the vapor or dust surrounding a target. Another option is to use ultrasonic systems [3] or inductive sensors [4].

Manuscript received June 7, 2021; revised August 4, 2021; accepted August 14, 2021. Date of publication September 3, 2021; date of current version January 5, 2022. This work was supported by the European Union's Horizon 2020 Research and Innovation Programme 2016–2020 under the Marie Skłodowska-Curie Grant 675683. (*Corresponding author: Aleksandra Baskakova.*)

The authors are with the Department of Electromagnetic Field, Czech Technical University in Prague, 16000 Prague, Czech Republic (e-mail: aleksandra.baskakova@fel.cvut.cz).

Color versions of one or more figures in this article are available at <https://doi.org/10.1109/TMTT.2021.3107503>.

Digital Object Identifier 10.1109/TMTT.2021.3107503

Microwave- and millimeter-wave (mm-wave) radars, such as stepped-frequency continuous-wave (SFCW), frequency-modulated continuous-wave (FMCW), or single-frequency (CW) radars, enable contactless distances to be determined. Standard antennas, e.g., horn and Vivaldi, are usually utilized in the radars. Those antennas have a good performance when the reflective target is in a far-field zone. However, nonlinear near-field effects appear when the target is close to the aperture of an antenna. The measured signal is corrupted due to multireflections, which results in distance measurement errors [5]–[8]. Designers of the radar systems suggest different sophisticated calibration methods to solve the consequences of these nonlinearities leaving their physical cause unsolved. The only exception is [7] where housing of the antenna is applied, which reduces measurement errors. However, no physical explanation of the effect and experimental results is given.

In our previous work [9], an experimental study of an R100 open-ended waveguide sensor with a choke flange was conducted. It was discovered that the dependence of the phase of the measured reflection coefficient on the distance to the target is quasi-linear around the resonant frequency of the choke. Thus, the measured distance can be found from a phase of the reflection coefficient formed by a signal reflected from a target as

$$d = \lambda(\pi - \varphi)/4\pi \quad (1)$$

where  $\varphi$  is a phase of the measured reflection coefficient,  $\lambda$  is a wavelength, and  $d$  is a distance from the reference plane to the target.

The purpose of this article developing the concept mentioned in [9] is to propose new sensors using open-ended circular and rectangular waveguides with a choke for ultrashort-distance measurements with the minimized nonlinear effects. The sensors are designed in the  $W$ -band to get the resolution in the order of micrometers. Robust physical explanations of properties and a new simple calibration/correction method are given.

This article is organized as follows. In Section II, the properties of new sensors, with a choke in the flange, are analyzed using the 3-D electromagnetic field simulator CST Studio Suite (CST); the properties are theoretically explained. In Section III, we propose a new physical model of the sensors based on simulated results and a calibration/correction method. In Section IV, the model and the calibration/correction method are experimentally verified using both new sensors. Comparisons of the measured and real distances with respect to the properties of the state-of-the-art sensors are given.

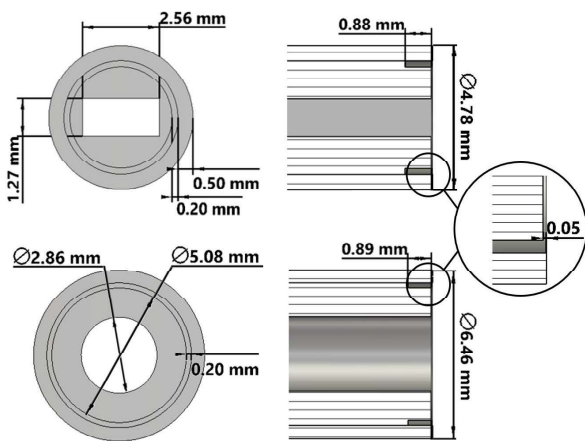


Fig. 1. Analyzed structures of the circular and rectangular sensors with chokes.

## II. THEORY AND SENSOR DESIGN

### A. Properties of Sensors

Structures of the new sensors founded on the idea from [9] are based on the WR10 waveguide and a circular waveguide (see Fig. 1). The approach from [10] is used to design the choke flanges. The distance from the inner wall of the circular waveguide, or from the center of the wider wall of the rectangular waveguide to the bottom of the choke notch, is selected to be one half of the wavelength at 80 GHz. In standard high-power applications, a choke forms a short in the planes of the waveguide walls if another waveguide, with a plane flange without choke, is attached. In our simulations in CST, a planar reflective target at different distances is applied instead of another flange.

Properties of the structures are simulated in the presence of a perfect electric conductor (PEC) with dimensions  $26 \times 26 \text{ mm}^2$ , set in front of the sensors at a distance interval from 0 up to 6 mm with an incremental step of 0.12 mm.  $S_{11}$  parameters, at a reference plane at the end of the structures, are determined in waveguide frequency bands of 75–90 GHz for those with circular waveguides and 75–110 GHz for those with rectangular waveguides. It should be emphasized that the magnitude of the measured  $S_{11}$  should also be above 0.2 to reduce the measurement uncertainties of a vector network analyzer (VNA) [11]. The  $TE_{10}$  mode in the rectangular waveguide and the  $TE_{11}$  mode in the circular waveguide are considered.

The reflection coefficients of the circular waveguide sensor with a choke flange for selected simulated distances to the target are shown in Fig. 2(a). Due to the presence of the choke, the magnitudes of  $S_{11}$  in distances below 1 mm are close to unity at frequencies around 78 GHz. It was found that the magnitude of  $S_{11}$  of the sensor is above the desired value of 0.2 in the frequency subband of 75–82.5 GHz for all considered distances. Furthermore, there are resonance loops in the distance interval of 0.6–1.44 mm. The reason for the resonances is explained later in Section II-B.

The most linear distance dependence of the phase is found at 79 GHz and is shown in Fig. 2(b). In the 75–80.5-GHz

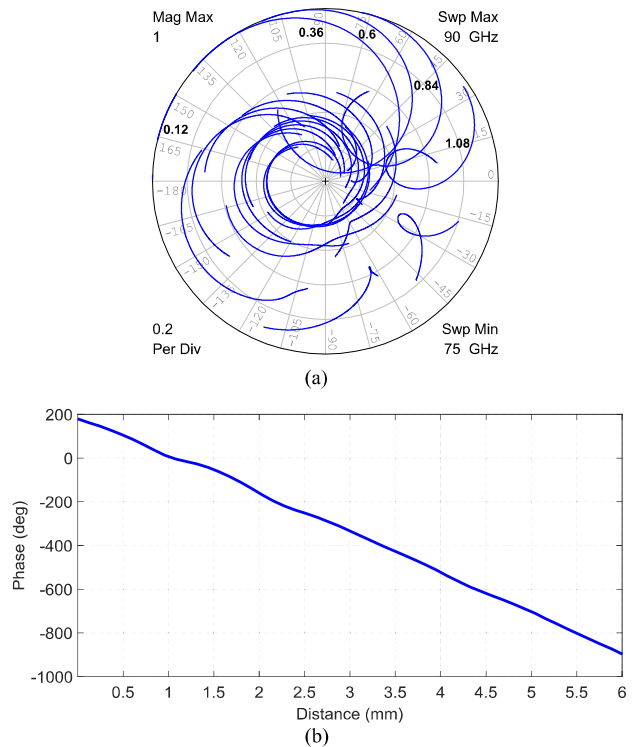


Fig. 2. Circular waveguide sensor. (a)  $S_{11}$  for selected target distances from 0 to 6 mm. (b) Phases of  $S_{11}$  for the target distances at  $f = 79 \text{ GHz}$ .

range, the phase quasi-linearly and monotonically decreases with the increasing distances.

$S_{11}$  of the rectangular waveguide sensor with a choke is shown in Fig. 3. The decrease of the magnitude of the reflection coefficient is very low in distances from 0 up to about 0.8 mm. A detailed analysis shows that in the frequency band from 76 up to 80.4 GHz, the magnitude of the reflection coefficient is above 0.2 for all distances of the target up to 6 mm.

The best phase versus the distance dependence at 79 GHz is shown in Fig. 3(b). The linearity is even better compared to the circular sensor with a choke. The phase is monotonically decreasing as distances increase in the frequency band from 75 to, at least, 80.4 GHz.

Both sensors are highly advantageous for short-distance measurement applications, since compared to standard antennas, they have a higher magnitude of reflection coefficient for small distances to the target and quasi-linear distance over phase dependence. It is a great edge over the sensors in [6] and [8]. Theoretical explanations of the sensors' properties based on the 3-D electromagnetic field simulations in CST are provided in Section II-B.

### B. Theoretic Explanation of the Sensors' Properties

1) *Circular Waveguide Sensor*: The volume between the target and the front of the circular waveguide sensor from the inner radius to the outer radius can be considered as a section of a radial line. Let us introduce cylindrical coordinates  $r$ ,  $\phi$ , and  $z$  and in the area of the gap (see Fig. 4).

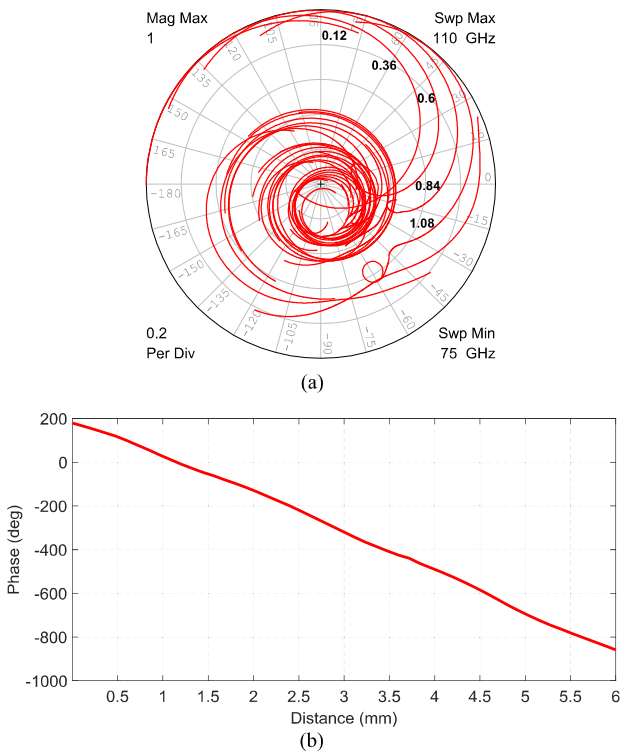


Fig. 3. Rectangular waveguide sensor. (a)  $S_{11}$  for selected target distances from 0 to 6 mm. (b) Phases of  $S_{11}$  for the target distances at  $f = 79$  GHz.

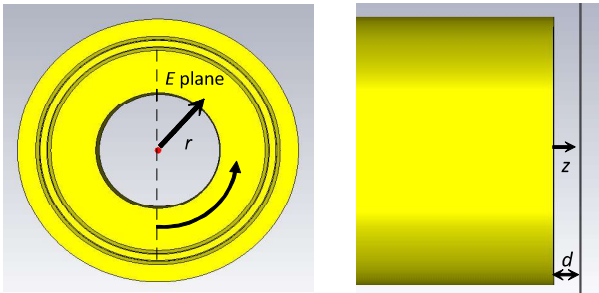


Fig. 4. Circular waveguide sensor and the target.

Variable  $d$  represents the gap width, and the dashed line corresponds to the  $E$ -plane in the  $TE_{11}$  mode in the circular waveguide.

The radial line is a nonuniform cylindrical region with the transmission direction along coordinate  $r$ . Depending on the frequency, dimensions of the structure, and type of excitation, a number of modes can propagate in the structure. The more modes move along the radial line, the greater the sensor loss.

With respect to the  $r$  coordinate, all modes are generally hybrid with both  $E_r$  and  $H_r$  components. If the magnetic field has no  $z$ -component, i.e.,  $H_z = 0$ , the transfer field can be represented as a superposition of a set of  $E$ -type modes [12]. The 3-D electromagnetic simulations in the frequency band of the circular waveguide sensor show that, despite some disturbances due to the excitation of higher order modes close to the circular waveguide end and due to the open space at the end of the radial line, the  $H_z$  components of the

field are, at least, ten times smaller than the  $H_r$  components. Therefore, the  $H_z = 0$  assumption can be accepted for the characterization of these  $E$ -type modes.

In accordance with [12], the transverse functional behavior of the  $E$ -field can be expressed as

$$E_z = K_z \cos(m\phi) \cos\left(\frac{n\pi}{d}z\right) \quad (2)$$

$$E_\phi = \frac{1}{r} K_\phi \sin(m\phi) \sin\left(\frac{n\pi}{d}z\right) \quad (3)$$

$$E_r = \frac{1}{r} K_r \cos(m\phi) \sin\left(\frac{n\pi}{d}z\right) \quad (4)$$

where mode indices  $m$  and  $n$  determine a type of a mode, with respect to the  $\phi$  and  $z$  coordinates, and  $K_z$ ,  $K_\phi$ , and  $K_r$  are complex constants.

The radial line is excited by the  $TE_{11}$  mode in the circular waveguide. It means that all modes excited in the radial line have the index  $m = 1$ . The mode can propagate only if  $f > f_c$ , where  $f$  is an operating frequency of the circular waveguide and  $f_c$  is the cutoff frequency of a mode in the radial line, which, for  $E$ -type modes, is expressed by

$$f_{cmn} = \frac{c}{\lambda_{cmn}} \quad (5)$$

where  $\lambda_{cmn}$  is a corresponding cutoff wavelength determined as

$$\lambda_{cmn} = \frac{1}{\sqrt{\left(\frac{n}{2d}\right)^2 + \left(\frac{m}{2\pi r}\right)^2}} \quad (6)$$

where  $r$  is both the inner radius of the radial line and the radius of the metallic circular waveguide.

For example, when  $d = 0.6$  mm, the first  $E$ -mode with indices  $m = 1$  and  $n = 0$  is excited and the corresponding cutoff frequency is equal to 33.3 GHz. The frequency band of the circular waveguide in  $TE_{11}$  mode is above the cutoff frequency of the radial line. Thus, the basic mode  $TE_{10}$  can propagate and radiate at the end of the radial line bringing losses in the structure except for the frequencies around 78 GHz, where there is nearly no radiation [see Fig. 5(a)]. At these frequencies, the choke creates a minimum of a standing wave or reflective electrical wall close to the input of the radial line [see Fig. 5(b), dashed lines]. It interrupts the expansion of the  $TE_{10}$  mode to the free space. This enables the field propagation from the metallic waveguide to the target and back as in a waveguide. Therefore, the concept of a virtual waveguide (VWG) can be introduced. Inside this VWG, the field reflected back from the target creates a standing wave holding information about the distance of the target. VWGs have different dimensions than a metallic waveguide, which depends on the frequency and dimensions of the choke and its distance from the metallic waveguide.

At higher frequencies around 86.4 GHz, the choke operates above its resonant frequency resulting in a less reflective electrical wall that is shifted deeper into the radial line [see Fig. 5(d)]. The VWG is lossy and has a larger radius than at lower frequencies, which enables the excitation of the higher order mode  $TM_{11}$  in it. The field distribution in the VWG and close to the end of the sensor corresponds to the field distribution in one half of a cylindrical cavity resonator with

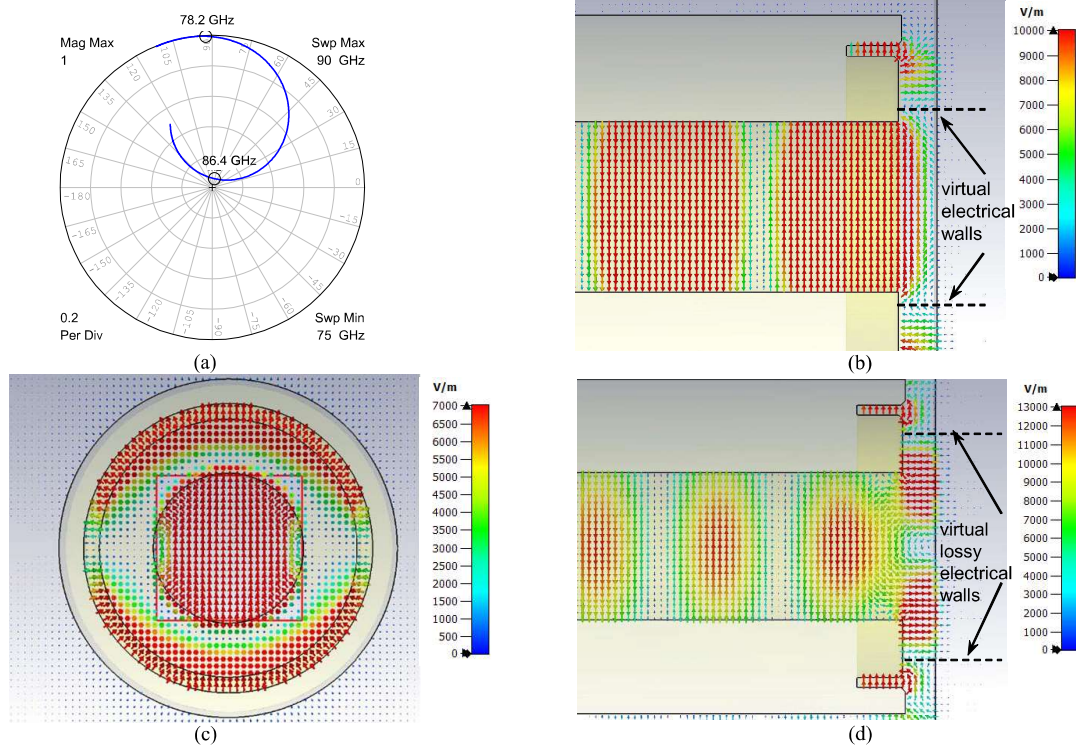


Fig. 5. Circular waveguide sensor. (a) Simulated  $S_{11}$  for  $d = 0.6$  mm;  $E$ -field distribution in the gap in the longitudinal section for (b)  $f = 78.2$  GHz and (d)  $f = 86.4$  GHz. (c)  $E$ -field distribution in the gap and the choke in the cross section for  $f = 78.2$  GHz.

the mode  $TM_{111}$ . This resonator with a resonant frequency of 86.4 GHz is critically coupled to the metallic waveguide [see Fig. 5(a)]. It is extremely problematic to determine a correct target distance from the phase of  $S_{11}$  correctly around the resonant frequency, and therefore, only sufficiently far frequencies can be used for distance measurements.

When  $d$  gets wider, a higher order mode gains more space for propagation in the radial line. The basic mode is excited at the low end of the frequency band. However, at higher frequencies, it is coupled less and less and the higher order mode with  $m = 1$  and  $n = 1$  starts to dominate. It continues in this fashion while increasing the gap of width  $d$  to mode  $m = 1$  and  $n = 2$  and  $m = 1$  and  $n = 3$ .

The choke influences the field distribution only in the part of the gap adjacent to the front of the sensor. Losses grow with increasing of  $d$  due to radiation into the free space. The standing wave half wavelengths in the area between the sensor and the target gradually decrease for larger distances  $d$  (see Fig. 6). There are three individual parts with different wavelengths that correspond to different dimensions of VWGs. We can estimate the borders (breaking points) of those VWGs from the  $E$ -field distribution picture. Analyzing the phase versus distance curve in Fig. 7, the slopes of each VWG enable to be determined. The intersections of the breaking points are marked by circles.

It means that with increase in  $d$ , the wavelength in the gap decreases from the wavelength of the metallic waveguide into the free-space wavelength, not continuously but in steps in accordance with the excitation of the individual modes in the

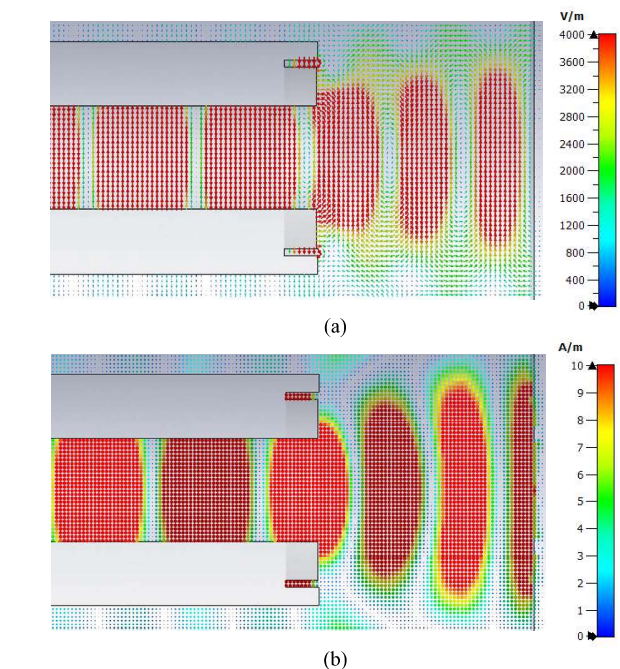


Fig. 6. Circular waveguide sensor with  $d = 6$  mm to the target. (a)  $E$ -field and (b)  $H$ -field distribution for  $f = 79$  GHz.

radial line. The wavelength remains constant in the distance interval corresponding to an individual mode.

It should be noted that  $E$ -field animations characterize a more complex field than those described by (2)–(4). They also

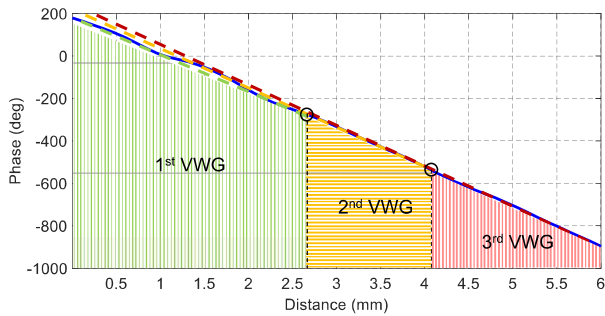


Fig. 7. Circular waveguide sensor with a choke.  $S_{11}$  phase for target distances from 0 to 6 mm,  $f = 79$  GHz.

cover the propagation of the field from the sensor toward the target and back, which forms a standing wave holding target distance information and the influence of the choke. However, (2)–(4) form a qualitative approximate tool for understanding the properties of the field between the sensor and target.

2) *Rectangular Waveguide Sensor*: The rectangular waveguide sensor with a choke is analyzed in the same way as the circular sensor with a choke in the frequency band of 75–110 GHz. The field distributions between both the circular and rectangular sensors with a choke and the target are notably similar. Figures equivalent to Figs. 5 and 6 are also obtained for the rectangular sensor with a choke. The main difference is in the resonant frequency of the virtual cavity resonators.

The difference in resonant frequencies can be explained with respect to the different dimensions of the chokes. The radius of the choke of the circular waveguide sensor (2.54 mm) is greater than in the case of the rectangular one (1.69 mm). The larger radius of the virtual cavity resonator of the circular waveguide sensor explained in Fig. 5(d) results in a resonant frequency of 86.4 GHz. On the other hand, the resonant frequency of the virtual cavity resonator of the rectangular waveguide sensor is around 105 GHz, which is advantageous with respect to a potentially wider frequency bandwidth applicable for distant measurements.

### III. CORRECTION METHOD

On the basis of the above results, namely Figs. 6 and 7, an equivalent circuit of the area between the sensors and the target formed by a cascade of three homogeneous lossy waveguides with different dimensions and wavelengths is proposed in Fig. 8(a). Distances  $d_1$  and  $d_2$  correspond to the breaking points where the three straight lines in Fig. 7 intersect. The simulated phase versus distance dependence is quasi-linear and slightly wavy along the three straight lines with different slopes (see Fig. 7). It is assumed that deviations result from multireflections due to the impedance discontinuities at steps at the connections of all considered waveguides with a dominating discontinuity at the end of the sensor.

It is also assumed that the influence of discontinuities can be eliminated by calibration/correction methods that have been used for decades in precise measurements using VNAs [13], [14]. In the case of measurements of waveguides,

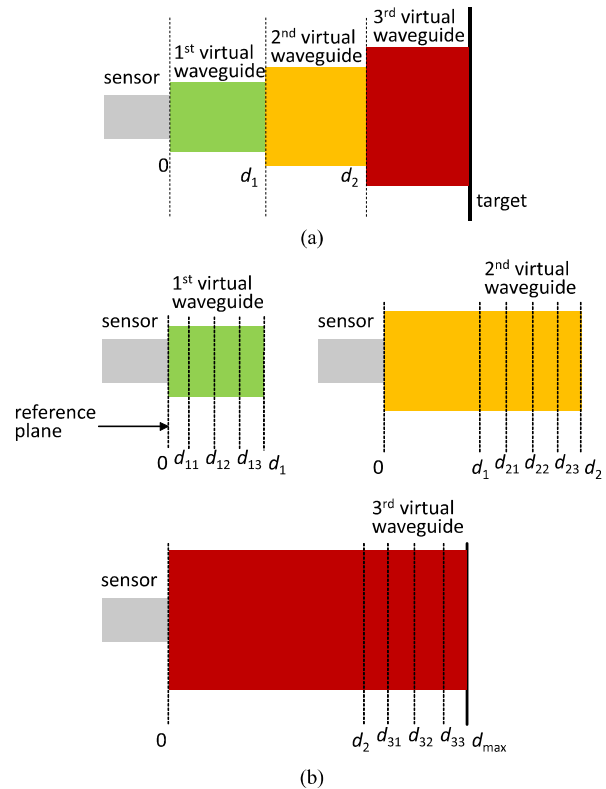


Fig. 8. Preliminary equivalent circuit of (a) the area between sensor and target and (b) a new calibration correction method.

a set of offset calibration standards are applied. However, the method using offset standards was developed for uniform lines. To apply such a method, a new calibration correction method is proposed. The new method uses an equivalent circuit consisting of three independent VWGs covering the space between the reference plane and distances  $d_1$ ,  $d_2$ , and  $d_{\max}$  using the second and third extended VWGs [see Fig. 8(b)]. Any reflection coefficient considered at reference planes placed in these VWGs at distance intervals  $(0, d_1)$ ,  $(d_1, d_2)$ , and  $(d_2, d_{\max})$  is seen at the reference plane of the sensor as being disturbed. The disturbances result from systematic errors due to impedance mismatching and losses. The situation in any of the VWGs in Fig. 8(b) can be characterized by a two-port error model shown in Fig. 9(a), which corresponds to the approach used in the one-port calibration correction method for a VNA as described by the flow graph in Fig. 9(b).

Different calibration methods based on [13] can then be used. The most common one-port calibration techniques for waveguides are short, offset short, and load (SSL) and triple offset shorts (SSS) [14]. The last method mentioned is advantageous because a metallic target (short) placed at three known distances from the sensor can be applied.

Using [14] and [15], three equations for calculating the error terms (7)–(9), as shown at the bottom of the next page, are derived, where  $p_1$ ,  $p_2$ , and  $p_3$  are the reflection coefficients of the standards seen at the beginning of individual VWGs at the reference plane and  $S_{11M}^{(1)}$ ,  $S_{11M}^{(2)}$ , and  $S_{11M}^{(3)}$  are the corresponding values of the simulated or measured reflection coefficients as seen in the sensor at the reference plane.

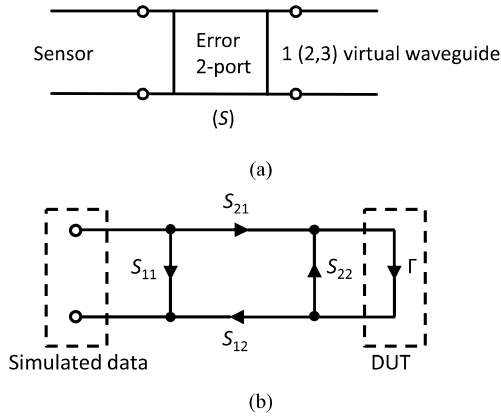


Fig. 9. (a) Error two-port. (b) Flow graph.

The standards for individual VWGs are considered as ideal shorts placed at the end of sections of individual lossy waveguides at distances  $d_{1i}$ ,  $d_{2i}$ , and  $d_{3i}$ , where  $i = 1, 2$ , and  $3$ , inside the distance intervals  $(0, d_1)$ ,  $(d_1, d_2)$ , and  $(d_2, d_{\max})$ , respectively [see Fig. 8(b)].

The corrected reflection coefficient  $S_{11Dd}$  at the reference plane of a considered VWG can be found from the one-port error term equation

$$S_{11Dd} = \frac{S_{11Md} - S_{11}}{(S_{11Md} - S_{11}) \cdot S_{22} + S_{12}S_{21}} \quad (10)$$

where index  $d$  corresponds to target distance and  $S_{11Md}$  is the simulated or measured reflection coefficient at the reference plane of the sensor. The distance of the target from the reference plane at a VWG can then be determined from the  $S_{11Dd}$  phase using (1). The new correction method uses the above approach independently in individual waveguides of the equivalent circuit in Fig. 8(b).

The estimated waveguide wavelengths and the corresponding widths or radii of the VWGs can be found from the estimated slopes of the phase versus distance dependence curve in Fig. 7 as

$$\lambda_{\text{WG}} = \frac{4\pi \cdot (d_{x1} - d_{x2})}{(\arg \Gamma_2 - \arg \Gamma_1)} \quad (11)$$

$$\lambda_C = \frac{\lambda_{\text{FS}}}{\sqrt{1 - \left(\frac{\lambda_{\text{FS}}}{\lambda_{\text{WG}}}\right)^2}} \quad (12)$$

$$r = \frac{1.8412 \cdot \lambda_C}{2\pi} \quad (13)$$

$$a = \frac{\lambda_C}{2} \quad (14)$$

where  $\lambda_{\text{WG}}$  is a wavelength in the waveguide,  $(d_{x1} - d_{x2})$  is the distance between two different distance points,  $d_{x1}$  and  $d_{x2}$ , on one of the straight lines in Fig. 7,  $\Gamma_1$  and  $\Gamma_2$  are their corresponding reflection coefficients,  $\lambda_C$  is the cutoff wavelength of the rectangular or cylindrical waveguide,  $\lambda_{\text{FS}}$  is the free-space wavelength,  $r$  is the radius of the cylindrical waveguide, and  $a$  is the width of the rectangular waveguide. The characteristic impedances of individual waveguides can be expressed by the formula

$$Z_0 = \frac{120\pi}{\sqrt{1 - \left(\frac{\lambda_{\text{FS}}}{\lambda_C}\right)^2}}. \quad (15)$$

#### A. Rectangular Waveguide Sensor

The calibration standards for the rectangular waveguide sensor are characterized as ideal shorts at the end of lossy rectangular waveguides in the  $\text{TE}_{10}$  mode. The lengths of these waveguides applied to the first VWG are 0, 0.48, and 0.84 mm. The first breaking point is considered at  $d_1 = 1.8$  mm. The lengths of the lossy waveguides for standards for the second VWG are selected at 1.92, 2.52, and 3 mm. The second breaking point is considered at  $d_2 = 3.96$  mm. The third VWG is supposed to be up to 6 mm and is calibrated using shorts placed at distances of 4.2, 4.68, and 5.16 mm.

The correction method can work properly only if wavelengths in the individual VWGs and their dimensions are correctly determined. However, they are determined by (11), which relies on three straight estimated lines in a figure equivalent to Fig. 7 corresponding to the rectangular waveguide sensor. The estimated widths of VWGs are  $a_1 = 3.23$  mm ( $\lambda_{\text{WG}} = 5.19$  mm),  $a_2 = 5.65$  mm ( $\lambda_{\text{WG}} = 3.94$  mm), and  $a_3 = 7.92$  mm ( $\lambda_{\text{WG}} = 3.85$  mm).

The correction method is implemented in the AWR design environment using output equation editor and elements, such as the rectangular waveguides in  $\text{TE}_{10}$  mode and ideal adapters between rectangular waveguides and 50- $\Omega$  coaxial lines.

We work with two curves: phase deviations of the corrected reflection coefficients  $S_{11Dd}$  determined by (10) from the straight lines and the magnitude dependence of the corrected reflection coefficients on distances in the interval  $(0, d_{\max})$ . The widths and losses of VWGs are then manually tuned with the goal of achieving a linear phase versus distance dependence and monotonically decreasing the magnitude while increasing the distance of the target at selected frequencies. The slopes of the straight lines are set in accordance with the current wavelengths of the VWGs.

$$S_{11} = \frac{p_2 \cdot (S_{11M}^{(1)} - S_{11M}^{(2)}) \cdot (p_3 \cdot S_{11M}^{(1)} - p_1 \cdot S_{11M}^{(3)}) + p_3 \cdot (S_{11M}^{(1)} - S_{11M}^{(3)}) \cdot (p_1 \cdot S_{11M}^{(2)} - p_2 \cdot S_{11M}^{(1)})}{p_2 \cdot (p_3 - p_1) \cdot (S_{11M}^{(1)} - S_{11M}^{(2)}) + p_3 \cdot (p_1 - p_2) \cdot (S_{11M}^{(1)} - S_{11M}^{(3)})} \quad (7)$$

$$S_{22} = \frac{S_{11} \cdot (p_1 - p_2) + p_2 \cdot S_{11M}^{(1)} - p_1 \cdot S_{11M}^{(2)}}{p_2 \cdot p_1 \cdot (S_{11M}^{(1)} - S_{11M}^{(2)})} \quad (8)$$

$$S_{12} \cdot S_{21} = (S_{11M}^{(1)} - S_{11}) \cdot (1 - S_{22} \cdot p_1) / p_1 \quad (9)$$



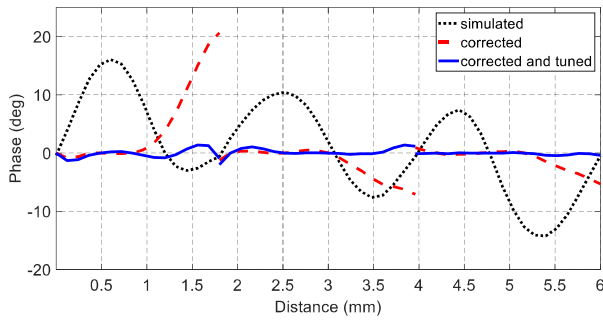


Fig. 10. Rectangular waveguide sensor. Deviation of  $S_{11}$  and  $S_{11Dd}$  phases from the linearity of simulated and corrected data, respectively, at 79 GHz.

The wavelength between the sensor and the target changes from the longest one closest to the metal waveguide wavelength toward a wavelength close to  $\lambda_{FS} = 3.795$  mm at 79 GHz. The phase deviations from the final linear traces of simulated, corrected, and corrected tuned data are shown in Fig. 10.

The method enables the simulated data in all distances at selected frequencies to be corrected. For example, at 79 GHz, corrected distances inside the VWGs for the distance intervals 0–1.8 mm (phase interval  $(+180, -70.54)^\circ$  at  $\lambda_{WG1}$ ), 1.8–3.96 mm (phase interval  $(-71.61, -462.9)^\circ$  at  $\lambda_{WG2}$ ), and 3.96–6 mm (phase interval  $(-464.2, -845.9)^\circ$  at  $\lambda_{WG3}$ ) can be determined using the formula

$$d_x = \lambda_{WG_i} \cdot (\pi - \arg S_{11Dd}) / (4\pi), \quad i = 1, 2, 3 \quad (16)$$

where  $S_{11Dd}$  corresponds to the values of the reflection coefficient determined with respect to the phase intervals by (10). Phase discontinuities, noticeable at the breaking points, result from independent calibrations in individual VWGs. These discontinuities do not disturb continuous distance determination using (16).

The deviation from the linear dependence in the distance interval close to the first breaking point (0.96 mm, 1.8 mm), corresponding to  $(+46.48, -70.54)^\circ$  at 79 GHz, starts to grow rapidly for frequencies differing significantly from 79 GHz. A similar effect around the second breaking point is observed as negligible. To explain the phenomenon, some transitions (TR) between waveguides with different dimensions are assumed, where one VWG transforms into another by gradually changing its wavelength. It means that formulas (7)–(10), based on the assumption of a uniform line with a constant wavelength, cannot work correctly at these distances. To extend an applicable frequency band, the second correction method is proposed. The transition close to the end of the first VWG is approximated by a section of another VWG [see Fig. 11(a)]. Fig. 11(b) shows the subsequently changed equivalent circuit.

$\Gamma_1$  corresponds to a reflection coefficient due to the impedance step between the first and the transition VWG. It can be determined by

$$\Gamma_1 = \frac{Z_{TR} - Z_{1VWG}}{Z_{TR} + Z_{1VWG}} \quad (17)$$

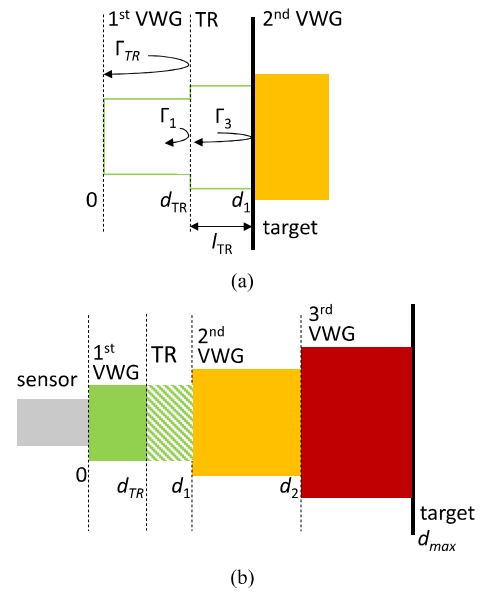


Fig. 11. Reflections of (a) transition and (b) final equivalent circuit.

where  $Z_{TR}$  and  $Z_{1VWG}$  are the impedances of the transition waveguide and the first VWG, respectively, and can be found from (15).

According to the formula for a single-section transformer [15], the resultant reflection coefficient at the input of the transition can be expressed as follows:

$$\Gamma_{TR} = \frac{\Gamma_1 + \Gamma_3 \cdot e^{-2j\theta}}{1 + \Gamma_1 \cdot \Gamma_3 \cdot e^{-2j\theta}} \quad (18)$$

where  $\Gamma_{TR}$  is a resultant reflection coefficient of the transition, including all multireflections, and  $\Gamma_3 = -1$  equals the reflection coefficient of the target.

A phase shift along the transition is

$$\theta = 2\pi \cdot l_{TR} / \lambda_{TR} \quad (19)$$

where the wavelength in the transition  $\lambda_{TR}$  can be found from

$$\lambda_{TR} = \frac{\lambda_{FS}}{\sqrt{1 - \left(\frac{\lambda_{FS}}{2a_{TR}}\right)^2}} \quad (20)$$

where  $a_{TR}$  is the width of the transition VWG.

The parameters of the first VWG and the TR waveguide are again manually tuned with the goal of achieving as linear a phase versus distance curve as possible in individual sections in an extended frequency band.

An expression for the length of the TR waveguide  $l_{TR}$ , which also means the distance of the target from the beginning of the transition, can be found after some transformations of the formula (18)

$$l_{TR} = -\frac{\lambda_{TR}}{4\pi} \arg \left( \frac{\Gamma_1 e^{-\frac{j4\pi d_{TR}}{\lambda_{VWG1}}} - S_{11Dd}}{e^{-\frac{j4\pi d_{TR}}{\lambda_{VWG1}}} - S_{11Dd} \Gamma_1} \right) \quad (21)$$

where  $S_{11Dd}$  corresponds to the corrected reflection coefficient at the reference plane of the first VWG, which is equivalent to

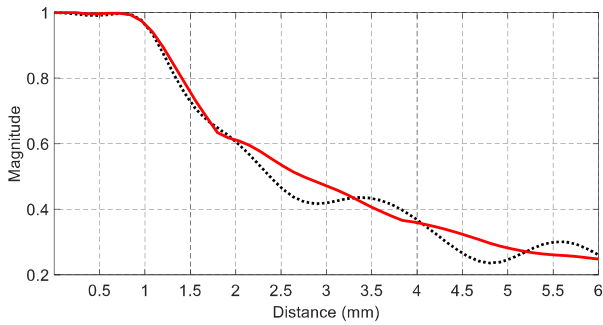


Fig. 12. Rectangular waveguide sensor. simulated (dashed line) and corrected (solid line) magnitude versus distance to the target at 79 GHz.

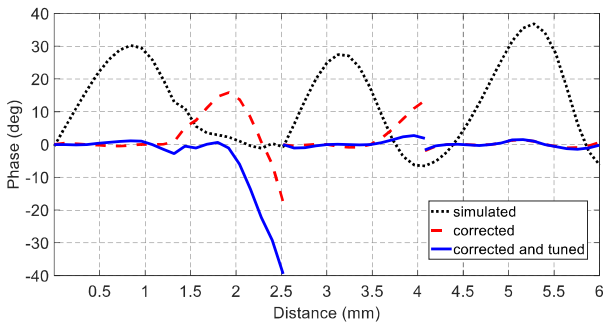


Fig. 13. Circular waveguide sensor. Deviation of  $S_{11}$  and  $S_{11,Dd}$  phases from the linearity of simulated and corrected data, respectively, at 75 GHz.

$\Gamma_{TR}$  transformed to this reference plane. The target distances in the transition can be determined using the second correction as

$$d_x = d_{TR} + l_{TR} \quad (22)$$

where  $d_{TR}$  is the distance of the beginning of the transition from the beginning of the first VWG and  $l_{TR}$  is determined by (21).

Other distances to the target outside the transition area from 0 to 6 mm can now be determined at any frequency in the interval 76–86 GHz using (16).

The entire distance interval 0–6 mm corresponds to the phase interval from 180 to  $-845.9^\circ$  at 79 GHz. However, VNA measurements of reflection coefficients provide the phase information only in the interval  $(+180, -180)^\circ$ . It means that there is a problem with phase ambiguities in determining the right distance. To distinguish what phase interval select to determine the correct distance, the magnitude over distance curve has to be monotonically decreasing. The dependence is shown in Fig. 12.

At small distances, the magnitude decreases slowly with the increasing distance of the target, which corresponds to small radiation from the sensor. When it starts to radiate, the trace bends and the dependence is approximately quasi-linear in the logarithmic scale with an approximate slope of 1.13 dB/mm. The corrected trace is a monotonically decreasing function, and no ambiguities occur in the distance determination.

### B. Circular Waveguide Sensor

The correction method applied to the rectangular waveguide sensor is also applied to the sensor using the cylindrical waveguide. The frequency of 75 GHz is selected as sufficiently

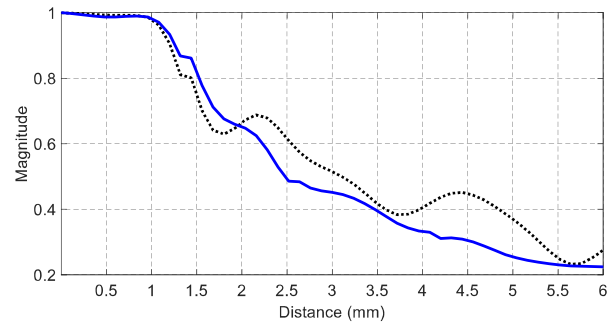


Fig. 14. Circular waveguide sensor. Simulated (dashed line) and corrected (solid line) magnitude versus distance to the target at 75 GHz.

far from the resonant frequency 86.4 GHz, as mentioned in Section II.

The calibration standards for the circular waveguide sensor are characterized as ideal shorts at the end of lossy cylindrical waveguides in the  $TE_{11}$  mode. The lengths of the standards applied to the first virtual cylindrical waveguide are 0, 0.36, and 1.08 mm; for the second VWG, they are 2.52, 3, and 3.48 mm; and for the third VWG, the standards are supposed at distances 4.32, 4.8, and 5.4 mm. The breaking points are derived at 2.52 and 4.08 mm. The radii calculated from the estimated slopes in Fig. 7 for the frequency 75 GHz are:  $r_1 = 2.42$  (corresponding to  $\lambda_{WG} = 4.61$  mm),  $r_2 = 6.02$  (corresponding to  $\lambda_{WG} = 4.34$  mm), and  $r_3 = 8.33$  mm (corresponding to  $\lambda_{WG} = 4.05$  mm).

The model is manually tuned in the same way as for the rectangular waveguide sensor case. The reflection coefficient phase deviations from the final linear traces of simulated, corrected, and corrected tuned data are shown in Fig. 13.

Corrected distances inside the VWGs for the intervals 0–1.32 mm (phase interval  $(+180, -17.93)^\circ$  at  $\lambda_{WG1}$ ), 2.52–4.08 mm (phase interval  $(-192.5, -449)^\circ$  at  $\lambda_{WG2}$ ), and 4.08–6 mm (phase interval  $(-449.3, -789.5)^\circ$  at  $\lambda_{WG3}$ ) at frequency 75 GHz can be determined using (16).

There are strong deviations near the first breaking point at the distance interval 1.32–2.52 mm (see Fig. 13). The reason is that not only the transition area but also the presence of the resonator discussed in Fig. 5(d) influences the reflection coefficient of the target. Due to its resonances, the sensor can be applied only at a narrow frequency band of 75–76 GHz, after the second part of the correction is employed. On the other hand, it is possible to use the sensor on selective distances 0–1.32 or 2.52–6 mm in a wider frequency band. The number of calibration measurements can be minimized to three if only distance measurements in one distance subinterval determined by the breaking points are demanded.

The sensor has no distance ambiguities since the curve from Fig. 14 is monotonically decreasing.

The first and the second correction characterized by (6)–(21) form a new general correction method, which suppresses the influences of the reflection from the sensor itself, multireflections between the sensor and the target, variable wavelength in the vicinity of the sensor, and also changes in the field configuration when one mode converts into another one.

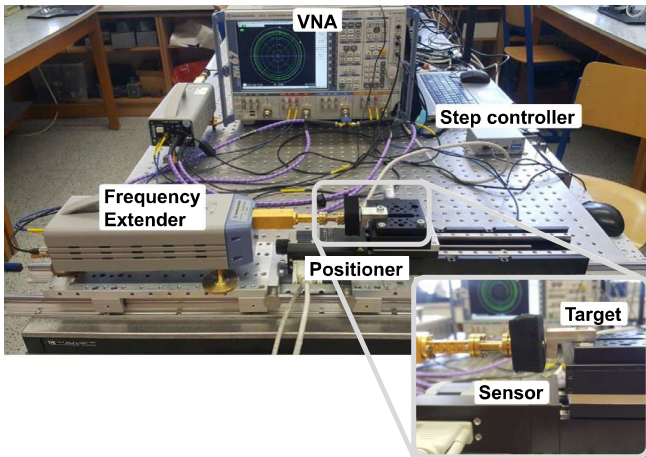


Fig. 15. Measurement setup.

This general method works well even in cases when the target is in close proximity of the sensor starting from zero distance. It is a great advantage compared to the correction method of complex subtraction of the reflection coefficient of the sensor in free space from the measured reflection coefficient of the target [17], which can work properly only when the target is sufficiently far from the sensor so that multireflections and changes of wavelength become negligible.

#### IV. EXPERIMENTAL VERIFICATION

Both new sensors are fabricated from brass using an NC machine tool and measured using a four-port R&S ZVA-67 VNA with R&S ZVA-Z110E mm-wave converters from 75 to 110 GHz (see Fig. 15). In the case of the circular waveguide sensor, smooth transitions from the WR10 waveguide to the circular waveguide are connected to both converters. The TRL calibration technique is applied at the reference planes of the WR10 and circular waveguide flanges. The measured data are then deembedded to the end of the sensors. The PI positioner (M-404.82S) and PC-controlled step controller (C663.11) are utilized to set the distances to the target. Both waveguide sensors are measured for the target distances from 0 to 6 mm with incremental steps of 0.12 mm, meaning that the same target positions are used for simulations. Multireflections between the target and flanges of the sensors connected to the mm-wave converter are suppressed by an absorber placed close to the flanges (see Fig. 15).

Using the data sheet of the producer of the VNA and mm-wave converters, the uncertainty analysis for the measurement setup is done. The converters bring a systematic residual error of  $\pm 1^\circ$  in measurements of high reflections. In addition, the trace stability of the VNA is typically less than  $\pm 2^\circ$  for the measurement IF bandwidth of 100 Hz. Uncertainty of  $1^\circ$  corresponds to  $10.4 \mu\text{m}$  at 80 GHz in free space, which means that, in total, the uncertainty of the distance measurements can be expected to be around  $\pm 15 \mu\text{m}$ .

The same correction method, waveguide dimensions, and loss/mm derived for the simulated data are applied to the measured data of both sensors. Summarized parameters for

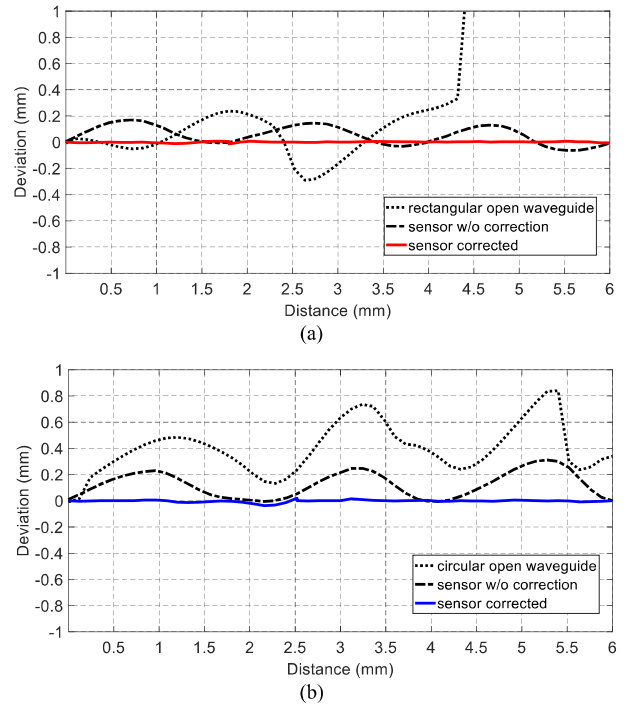


Fig. 16. Deviation of the measured distance from the real distance. (a) Rectangular waveguide sensor with choke and open-ended rectangular waveguide at 80 GHz. (b) Circular waveguide sensor with choke and open-ended circular waveguide and at 75 GHz.

the sensors at the best frequencies and the extreme frequencies can be found in Table I.

The deviations between the real target distance determined by the positioner and the target distance determined from the VNA measured reflection coefficient after correction are shown in Fig. 16. For a better comparison, the results of the waveguide sensors without correction as well as measured results of rectangular and circular open-ended waveguides without choke with distances determined by (1) using  $\lambda_{FS}$  are added.

The only open-ended waveguides enable the distances from 0 to 6 mm of the target to be measured, but with errors exceeding 0.5 mm at certain distances. Applying new waveguide sensors with a choke improves measurements so that the maximum errors of the measurements are no greater than 0.18 mm for the rectangular sensor and around 0.3 mm in the case of the cylindrical one. Applying the new correction method significantly reduces the values of measurement errors. In the case of the new rectangular waveguide sensor, it is  $12 \mu\text{m}$  at 80 GHz, and in the case of the new circular waveguide sensor, it is  $19 \mu\text{m}$  at 75 GHz. It is less than 0.7% and 0.9% of the measured distances. However, these errors are in the same order as the  $\pm 15\text{-}\mu\text{m}$  VNA distance measurement uncertainties mentioned above. Therefore, it can be supposed that the errors caused by the new sensors themselves and by the new correction method are even smaller.

It was also experimentally verified that both new sensors produce notably little radiation, which results in a magnitude of the measured reflection coefficient close to unity until the

TABLE I  
EXPERIMENTALLY PROVED SENSOR PROPERTIES

<b>Rectangular waveguide sensor</b>					
Freq. (GHz)	Target distance areas (mm)	1 <sup>st</sup> VWG	Transition	2 <sup>nd</sup> VWG	3 <sup>rd</sup> VWG
		0÷0.96	0.96÷1.8	1.8÷3.96	3.96÷6
76	<i>a</i> (mm)	2.93	2.47	6.0	11.2
	loss (dB/mm)	0.691	0.691	2.102	2.235
	Phase intervals (deg)	180÷49.42	49.42 ÷-66.6	-65.46÷-437.4	-436.4÷-801.2
	max. dev. (μm)	0÷-13	25.8÷-4.2	20÷-15	11÷-6
	<i>s</i> (μm)	5.54	9.97	9.41	4.12
79	<i>a</i> (mm)	2.78	2.84	7.0	11.2
	loss (dB/mm)	0.089	0.089	2.002	2.172
	Phase intervals (deg)	180÷46.48	46.48÷-70.54	-71.61÷-462.9	-464.2÷-845.9
	max. dev. (μm)	0÷-4.6	8.4÷-11.6	8÷-14	7÷-7
	<i>s</i> (μm)	1.86	7.17	4.46	3.17
80	<i>a</i> (mm)	2.75	2.95	6.9	11.2
	loss (dB/mm)	0.127	0.127	2.386	2.401
	Phase intervals (deg)	180÷44.91	44.91÷-75	-74.64÷-472.5	-472.7÷-859.5
	max. dev. (μm)	0÷-2.8	6.2÷-11.8	6÷-12	9÷-1
	<i>s</i> (μm)	1.23	6.27	3.51	2.7
86	<i>a</i> (mm)	2.9	4.0	6.7	11.2
	loss (dB/mm)	1.201	1.201	1.931	2.218
	Phase intervals (deg)	180÷24.86	24.86÷-119.6	-116.5÷-551	-549.4÷-964.6
	max. dev. (μm)	7.2÷-10.2	15.6÷5.6	21÷-11	8÷-2
	<i>s</i> (μm)	8.09	3.46	9.26	2.67
<b>Circular waveguide sensor</b>					
Freq. (GHz)	Target distance areas (mm)	1 <sup>st</sup> VWG	Transition	2 <sup>nd</sup> VWG	3 <sup>rd</sup> VWG
		0÷1.32	1.32÷2.52	2.52÷4.08	4.08÷6
75	<i>r</i> (mm)	2.05	4.4	2.8	7.2
	loss (dB/mm)	0.238	0.238	2.3	2.34
	Phase intervals (deg)	180÷-17.93	-17.93÷-231.7	-192.5÷-449	-449.3÷-789.5
	max. dev. (μm)	5÷-16	16÷-19	15÷-14	4÷-12
	<i>s</i> (μm)	5.43	11.01	8	5.3
76	<i>r</i> (mm)	1.95	7.7	2.9	7.3
	loss (dB/mm)	0.3684	0.3684	2.154	2.235
	Phase intervals (deg)	180÷-15.18	-15.18÷-240.4	-190.5÷-449.6	-452÷-796.7
	max. dev. (μm)	6.3÷-14	20÷-38	14÷-5	5÷-9
	<i>s</i> (μm)	5.95	15.77	4.63	3.78

target distance reaches approximately 1 mm in accordance with Figs. 12 and 14.

The new correction method not only improves the precision of the distance measurements but also increases the operational frequency band of the sensors to 76–86 GHz for the rectangular sensor and to 75–76 GHz for the circular one. The comparisons of the properties of the sensors for several selected frequencies are summarized in Table I, where phase intervals correspond to the corrected data.

The maximum deviation between the real distances and the measured distances as well as the sample standard deviations *s* offering a better global view on measurement uncertainties is included. *s* is given as

$$s = \sqrt{\frac{1}{N-1} \sum_{i=1}^N (x_i - \bar{x})^2} \quad (23)$$

where *N* is the number of distant points, *x<sub>i</sub>* are deviations in individual distances, and  $\bar{x}$  is the mean value of deviations.

The rectangular sensor has a significantly wider applicable frequency band compared to the circular one, as explained

TABLE II  
NEW SENSORS AND STATE-OF-THE-ART SENSORS

Technology	Sensor size (mm)	Freq. (GHz)	Max error (μm)	Range (mm)	Ref.
VNA	4.5x5.3	80,92,95	200	5-50	[5]
FMCW	Ø72	24-28/4	200	0-5000	[18]
Six-port	5x7.5	60/-	250	5-27.5	[19]
Six-port	7.8	61/-	<100	0-7.5	[20]
Six-port	-	24/-	700	0-20	[8]
CW	6	77/-	10	2-5	[7]
VNA	Ø6.5	75-76/2	19 (at 75GHz)	0-6	Circ. sensor*
VNA	Ø4.8	76-86/10	12 (at 80GHz)	0-6	Rect. sensor*

\* this work

in Section III. The best properties of the rectangular sensor can be found around the resonant frequency of the choke.

Properties of both sensors were also compared with state-of-the-art sensors (see Table II). The table shows that in comparison with other sensors measuring from the zero distance, the new sensors have about ten times smaller distance

measurement errors. A comparable maximum error can be found only in the sensor from [7]. However, the authors provide only results of simulations and no result for the most critical area close to zero distance. Namely, the rectangular waveguide new sensor has also outstanding applicable frequency bandwidth of 10 GHz.

## V. CONCLUSION

New circular- and rectangular-shaped open-ended waveguide sensors with a choke flange at the end for contactless ultrashort-distance measurements starting from zero distance in the *W*-band have been designed and fabricated. Both sensors at the selected frequency bands are capable of achieving a quasi-linear dependence of the measured reflection coefficient phase on the distance to the target with no ambiguities. A physical explanation and description of the field behavior between the sensors and the target has been suggested and a corresponding physically well-founded equivalent circuit based on a cascade of VWGs with different dimensions has been proposed. A new two-step calibration correction method based on the equivalent circuit has been derived. The new method suppresses the influences of the reflection from the sensor itself, multireflections between the sensor and the target, variable wavelength in the vicinity of the sensor, and also changes in the field configuration when one mode converts into another one. Only nine calibration measurements are necessary for measurements in the whole distance interval from 0 to 6 mm. Both sensors have been successfully experimentally verified. The sensors enable the distances from zero to more than one and half of the wavelength with maximum error below 0.9% and 0.7%, respectively, to be determined. In comparison with the state-of-the-art sensors, the new sensors enable to achieve about ten times smaller distance measurement errors. Both new sensors are applicable in wide frequency bandwidths 2 and 10 GHz.

## REFERENCES

- [1] K. Alzahrani, D. Burton, F. Lilley, M. Gdeisat, F. Bezombes, and M. Qudeisat, "Absolute distance measurement with micrometer accuracy using a Michelson interferometer and the iterative synthetic wavelength principle," *Opt. Exp.*, vol. 20, no. 5, pp. 5658–5682, Feb. 2012.
- [2] M. Norgia, G. Giuliani, and S. Donati, "Absolute distance measurement with improved accuracy using laser diode self-mixing interferometry in a closed loop," *IEEE Trans. Instrum. Meas.*, vol. 56, no. 5, pp. 1894–1900, Oct. 2007.
- [3] A. P. Cracknell, *Ultrasonics*. London, U.K.: Wykeham, 1982, ch. 3.
- [4] M. Jagiella and S. Fericean, "Miniaturized inductive sensors for industrial applications," in *Proc. IEEE Sensors*, Jun. 2002, pp. 771–778, doi: 10.1109/ICSENS.2002.1037204.
- [5] A. Schicht, K. Huber, A. Ziroff, M. Willsch, and L.-P. Schmidt, "Absolute phase-based distance measurement for industrial monitoring systems," *IEEE Sensors J.*, vol. 9, no. 9, pp. 1007–1013, Sep. 2009, doi: 10.1109/JSEN.2009.2025582.
- [6] Y. Venot and W. Wiesbeck, "76.5 GHz radar sensor for contact-free distance measurement with micrometer accuracy," in *Proc. IEEE Sensors*, Oct. 2003, pp. 216–221, doi: 10.1109/ICSENS.2003.1278931.
- [7] C. Rusch, S. Beer, and T. Zwick, "LTCC endfire antenna with housing for 77-GHz short-distance radar sensors," *IEEE Antennas Wireless Propag. Lett.*, vol. 1, pp. 998–1001, 2012, doi: 10.1109/LAWP.2012.2213791.

- [8] S. Linz *et al.*, "Ultra-short-range, precise displacement measurement setup with a near field slot-line antenna and a dedicated spiral calibration," in *IEEE MTT-S Int. Microw. Symp. Dig.*, May 2015, pp. 1–4, doi: 10.1109/MWSYM.2015.7167116.
- [9] A. Baskakova and K. Hoffmann, "Investigation of waveguide sensors for ultra-short-distance measurements," in *Proc. 93rd ARFTG Microw. Meas. Conf. (ARFTG)*, Jun. 2019, pp. 1–4, doi: 10.1109/ARFTG.2019.8739174.
- [10] C. G. Montgomery, R. H. Dicke, E. M. Purcell, *Principles of Microwave Circuits*. New York, NY, USA: McGraw-Hill, 1948.
- [11] *Technical Specifications Agilent Technologies PNA Series Network Analyzers E8362A, E8363A, and E8364A*, document 5989-1072EUS, USA, Jul. 2006. [Online]. Available: <https://literature.cdn.keysight.com/litweb/pdf/5989-1072EUS.pdf?id=450959>
- [12] N. Marcuvitz, *Waveguide Handbook*. New York, NY, USA: McGraw-Hill, 1951.
- [13] S. Rehnmark, "On the calibration process of automatic network analyzer systems (short papers)," *IEEE Trans. Microw. Theory Techn.*, vol. MTT-22, no. 4, pp. 457–458, Apr. 1974, doi: 10.1109/TMTT.1974.1128250.
- [14] "The essentials of VNA from  $\alpha$  to Z0," Anritsu, USA, Tech. Rep. 11410-00476A, Jan. 2009.
- [15] G. Bryant, *Principles of Microwave Measurements*. London, U.K.: Peregrinus on behalf of Institution of Electrical Engineers, 1993.
- [16] D. M. Pozar, *Microwave Engineering*, 3rd ed. Hoboken, NJ, USA: Wiley, 2005.
- [17] C. Rusch, J. Schäfer, T. Kleiny, S. Beer, and T. Zwick, "W-band Vivaldi antenna in LTCC for CW-radar nearfield distance measurements," in *Proc. 5th Eur. Conf. Antennas Propag. (EUCAP)*, vol. 2011, pp. 2124–2128.
- [18] N. Pohl, M. Gerding, B. Will, T. Musch, J. Hausner, and B. Schiek, "High precision radar distance measurements in overmoded circular waveguides," *IEEE Trans. Microw. Theory Techn.*, vol. 55, no. 6, pp. 1374–1381, Jun. 2007, doi: 10.1109/TMTT.2007.896784.
- [19] K. Haddadi, M. M. Wang, D. Glay, and T. Lasri, "A 60 GHz six-port distance measurement system with sub-millimeter accuracy," *IEEE Microw. Compon. Lett.*, vol. 19, no. 10, pp. 644–646, Oct. 2009, doi: 10.1109/LMWC.2009.2029744.
- [20] S. Mann *et al.*, "Substrate integrated waveguide fed antenna for 61 GHz ultra-short-range interferometric radar systems," in *Proc. IEEE Topical Conf. Wireless Sensors Sensor Netw. (WiSNet)*, Jan. 2016, pp. 64–66, doi: 10.1109/WISNET.2016.7444323.



**Aleksandra Baskakova** received the B.S. and M.Sc. degrees in radio engineering from Saint-Petersburg Electrotechnical University "LETI," Saint Petersburg, Russia, in 2011 and 2013, respectively. She is currently pursuing the Ph.D. degree at the Microwave Measurement Group, Department of Electromagnetic field, Czech Technical University in Prague, Prague, Czech Republic.

Her research interests include the design of microwave circuits and components, microwave imaging, 3-D electromagnetic simulations, vector network analyzer (VNA), measurements, and calibration techniques.



**Karel Hoffmann** (Senior Member, IEEE) received the Ing. degree (Hons.) from the Czech Technical University in Prague, Prague, Czech Republic, in 1974.

From 1990 to 1991, he spent four months with the University of Rome "Tor Vergata," Rome, Italy, where he was involved with research on precise microwave measurement correction methods. From 1994 to 2002, he was an Associate Professor with the Faculty of Electrical Engineering, Czech Technical University in Prague, where he has been a Full Professor since 2002. His professional activities are focused on the design of active and passive microwave integrated circuits, precise microwave measurement, and modeling of microwave components.

## 4.3 W-Band Imaging Sensor Using a Rectangular Waveguide Structure With Choke

**This chapter is a version of the published manuscript:**

**A. Baskakova**, and K. Hoffmann, “W-Band Imaging Sensor Using a Rectangular Waveguide Structure With Choke,” in *IEEE Microwave and Wireless Components Letters*, vol. 32, no. 3, pp. 230–233, March 2022, doi: 10.1109/LMWC.2021.3134472.

**Connection to my Ph.D. thesis:**

The development of the distance sensors, which performed exceptionally well, inspired me to apply them to near-field scanning. The best properties were achieved for the rectangular sensor based on the WR10 waveguide with a choke flange. Therefore, this sensor was evaluated using a planar metal-dielectric SUT, thus enabling the detection of different materials. The simplified calibration/correction technique based on triple offset shorts (SSS) was applied to the measured data. Unlike known and similar sensors, this sensor enables the scanning of a metal-dielectric SUT at 80 GHz with correct amplitudes and a contrast of reflection coefficients corresponding to their local material parameters in a standoff distance interval of 0.3 – 4 mm (0.08 to 1.07  $\lambda_0$ ). A spatial resolution of 1.9 mm is achieved at a 2-mm standoff distance. This study confirmed that the sensor is multifunctional and has outstanding features that surpass the properties of state-of-the-art sensors.

# W-Band Imaging Sensor Using a Rectangular Waveguide Structure With Choke

Aleksandra Baskakova<sup>1b</sup> and Karel Hoffmann<sup>1b</sup>, *Senior Member, IEEE*

**Abstract**—A new application of a rectangular waveguide structure with a choke from Baskakova and Hoffmann (2021) is proposed for high-contrast imaging in the W-band. As with homogeneous lossy waveguides, the field distribution in front of the open-ended sensor is observed and a calibration/correction method is applied. The sensor is evaluated using planar metal-dielectric samples under test (SUT), thus enabling the detection of different materials with a standoff distance ranging from 0.08 to 1.07  $\lambda_0$ . The sensor can determine both amplitudes and the contrast of the reflection coefficients correctly at the reference plane of the SUT, which is not possible for state-of-the-art sensors. The maximum contrast of the imaging is greater than 26 dB. A spatial resolution and minimum resolution for the tracking of SUT local properties of 1.9 mm are achieved at standoff distances of 2 and 1 mm, respectively.

**Index Terms**—Microwave measurement, mm-wave imaging, mm-wave sensors, rectangular waveguide, waveguide flange choke.

## I. INTRODUCTION

NEAR-FIELD imaging is widely used for many biological and industrial applications, such as noninvasive sensing, the characterization of biological samples [2], material characterization [3], the detection of surface defects [4], the evaluation of different surfaces [5]–[8], the inspection of composite materials [9], etc. In the microwave and millimeter-wave region, near-field imaging is an accurate tool, which does not require special measurement conditions, that can be adapted for industrial environments, and is hazard-free.

Some specific applications of near-field imaging include new automotive radar systems operating at 76–81 GHz [10]. The radar antennas are located behind a plastic bumper or the nameplate of the producer, often in the form of the corporate logo, making it necessary to measure the bumper or the nameplate properties to determine their impact on the radar antennas radiation pattern. Nowadays, it can be approximately measured with a far-field approach using a vector network analyzer (VNA) with two horn antennas and lenses. However, a proper near-field millimeter-wave imaging sensor would

Manuscript received November 19, 2021; accepted November 26, 2021. Date of publication December 21, 2021; date of current version March 11, 2022. This work was supported by the European Union's Horizon 2020 Research and Innovation Program 2016–2020 under the Marie Skłodowska-Curie Grant under Agreement 675683. (*Corresponding author: Aleksandra Baskakova.*)

The authors are with the Department of Electromagnetic Field, Czech Technical University in Prague, 16000 Prague, Czech Republic (e-mail: aleksandra.baskakova@fel.cvut.cz).

Color versions of one or more figures in this letter are available at <https://doi.org/10.1109/LMWC.2021.3134472>.

Digital Object Identifier 10.1109/LMWC.2021.3134472

be more advantageous as it provides local properties of the obstacles.

Several published articles on imaging microwave sensors used an operational frequency no higher than 24 GHz, however, no research focused on imaging sensors working in the frequency band of 76–81 GHz could be found. Resonant near-field sensors [7], [8] use resonant probes with dimensions of  $0.01 \div 0.2 \lambda_0$  (free space wavelength), thereby making it difficult to scale up to frequencies around 80 GHz. Non-resonant techniques are not constrained by this limitation [5], [6], although standoff distances around  $0.08 \lambda_0$  are relatively small and can bring misalignment problems at higher frequencies. Moreover, in both types of sensors, the obtained image does not provide realistic information regarding the local amplitudes of reflection coefficients of the samples under test (SUT) and their ratios (contrasts).

This letter demonstrates the successful use of our previously published sensor [1] in W-band imaging. Unlike known and similar sensors, this sensor enables the scanning of metal-dielectric SUT at 80 GHz with correct amplitudes and a contrast of the reflection coefficients corresponding to their local material parameters in a standoff distance interval of 0.3–4 mm. A spatial resolution of 1.9 mm is achieved at a 2-mm standoff distance.

## II. SENSOR DESIGN AND CALIBRATION

In our previous work [1], a distance sensor with a choke notch in a flange was proposed to create an extremely high impedance at its input, significantly suppress the current flow across the notch, and concentrate the field in front of the sensor. The fabricated sensor, see Fig. 1, is applied to near-field scanning in this letter.

The field distribution of the open sensor is demonstrated in Fig. 2. The choke shapes the field so that three lossy virtual waveguides (VWGs) for three distance intervals from the reference plane of the sensor, up to distances around  $1.6 \lambda_0$  at 80 GHz, can be considered.

Due to the homogeneous distribution of the field in individual VWGs, it is possible to eliminate impedance discontinuities where the end of the sensor and the considered VWGs are connected. This can be done by the common one-port calibration technique for waveguides with triple offset shorts (SSS) [11], [12].

The entire correction/calibration method is described in Section III of [1]. Its equivalent circuit includes three VWGs and a transition area occurring between the first and second

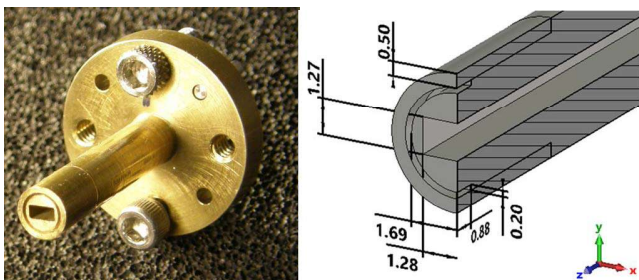


Fig. 1. Photograph and illustration of the designed sensor (sizes are in millimeter).

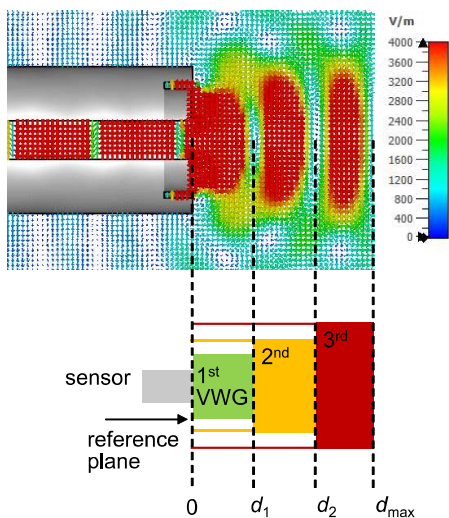


Fig. 2.  $E$ -field (top) and an equivalent circuit used in the calibration (bottom).

VWGs. Correcting the results for standoff distances located in the transition area ( $\approx 1 \div 1.8$  mm) requires solving more complex equations. To avoid this in imaging applications, we recommend selecting the standoff distances out of the transition area and using a simplified correction procedure.

An equivalent circuit used in the calibration is depicted in Fig. 2. It consists of three independent VWGs covering the space between the reference plane and distances  $d_1$ ,  $d_2$ , and  $d_{\max}$ , which correspond to the end of each VWG and can be determined from Fig. 2 as 1.8, 3.96, and 6 mm, respectively, see also [1] for more details. Depending on the selected standoff distance, the reflection coefficient of the three standards have to be defined for one of the intervals  $(0; d_1)$ ,  $(d_1; d_2)$ , or  $(d_2; d_{\max})$  and the corresponding values of the measured reflection coefficient have to be determined.

For the definition of the standard sets, three distances have to be selected. The calibration standards are characterized as ideal shorts placed at the end of lossy waveguides. In our work, the lengths of the standards applied to the first VWG are 0, 0.48, and 0.84 mm (all outside the transition area) with losses of 0.063 dB/mm; for the second VWG they are 1.92, 2.52, and 3 mm with losses of 1.2 dB/mm; and for the third VWG the standards are supposed at distances 4.2, 4.68, and 5.16 mm with losses of 1.33 dB/mm. Then, the  $S_{11}$  values of the sensor, with a metallic plate placed at the selected distances, are measured.

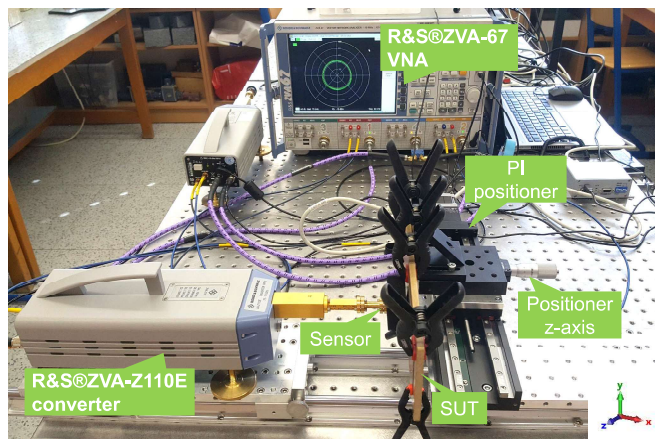


Fig. 3. Measurement setup.

Now, having obtained all the necessary data, formulas from [12] are applied to correct the measured scanning data. In addition, the resultant reflection coefficient enables to be transformed through the lossy waveguide, so that the reference plane of the measurement is located at the plane of the SUT.

Generally, the reference plane of standard open-ended waveguide sensors is at the end of the waveguide. The measured reflections forming the images are incorrect as they are influenced by reflections from the sensor itself. Accordingly, the images cannot have correct contrasts.

Our approach enables us to correct and de-embed the scanning data to the plane of the SUT by subtracting the corresponding section of the VWG. This provides the correct amplitudes and a contrast in the reflection coefficient image.

### III. EXPERIMENTAL RESULTS

The new sensor was measured using a setup consisting of an R&S<sup>®</sup>ZVA-Z110E millimeter-wave converter from 75 to 110 GHz and a 4-port R&S<sup>®</sup>ZVA-67 VNA, see Fig. 3. We measured two SUTs, formed by a 0.508-mm-thick CuClad 233 substrate, where  $\epsilon_r = 2.33$  and with 17- $\mu$ m-thick copper patterns, placed on the Physik Instrumente (PI) positioner (M-404.82S) controlled by a PC using a step controller (C663.11). Incremental steps were set at 0.25 mm. The TRL calibration technique is applied at the reference plane of a WR10 waveguide connecting flange. The measured data are de-embedded to the reference plane of the sensor, then post-processed using the proposed calibration technique, including the de-embedding to the plane of the SUT. For a better comparison of the results, we also measured a WR10 tapered waveguide sensor using the same setup and TRL calibration only. The sensors were also measured without the SUT.

The pattern of the first SUT is composed of metal strips 5.08-mm-wide. Measurement results are presented in Fig. 4 and correspond to different standoff distances to the SUT: 0.3 and 1 mm inside the first VWG, 2 mm inside the second VWG, and 4 mm inside the third VWG. Contrasts  $|S_{11}^m/S_{11}^{fs}|$ ,  $|S_{11}^d/S_{11}^{fs}|$ , and  $|S_{11}^m/S_{11}^d|$ , as ratios of the magnitudes of reflection coefficients with a different medium, namely metal ( $m$ ), free space ( $fs$ ), and substrate ( $d$ ), are summarized in Table I.



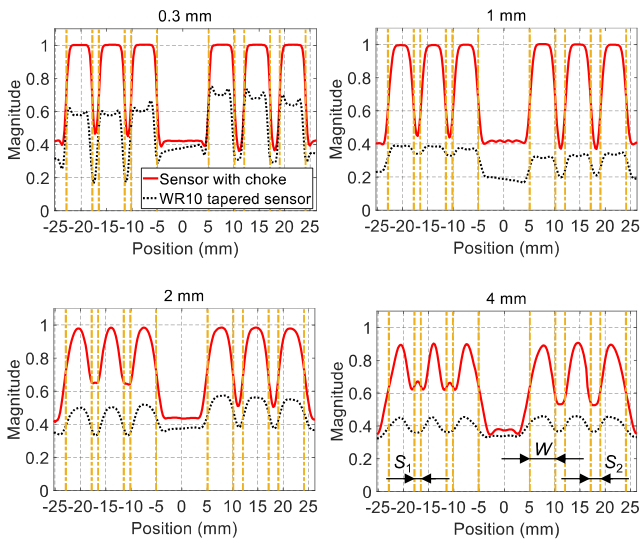


Fig. 4. Magnitude of the measured  $S_{11}$  from SUT1 consisting of metal strips with width  $W = 5.08$  and gaps of  $S_1 = 1.27$  mm and  $S_2 = 1.9$  mm (indicated by the vertical dashed lines) for different standoff distances at 80 GHz.

TABLE I  
CONTRAST COMPARISON

Standoff distance	0.3 mm		1 mm		2 mm		4 mm	
	1 <sup>st</sup>	2 <sup>nd</sup>	1 <sup>st</sup>	2 <sup>nd</sup>	1 <sup>st</sup>	2 <sup>nd</sup>	1 <sup>st</sup>	2 <sup>nd</sup>
$ S_{11}^m $	0.22	<0.05	0.22	<0.05	0.22	<0.05	0.22	<0.05
$ S_{11}^d $	0.7	1	0.32	1	0.57	0.98	0.46	0.89
$ S_{11}^m/S_{11}^d $	3.2	>22	1.45	>22	2.6	>20	2.1	>18
$ S_{11}^d/S_{11}^m $	1.8	>9.4	0.86	>8.3	1.7	>8.7	1.6	>7.4
$ S_{11}^m/S_{11}^d $	1.8	2.4	1.7	2.4	1.5	2.3	1.4	2.4

1<sup>st</sup> sensor - WR10

2<sup>nd</sup> sensor - new sensor

The new sensor (the second sensor in Table I) measures  $|S_{11}|$  at the reference plane of the sample. In front of the metal strip, it is equal to unity, provided the openings of the VWGs are fully covered by the strip. In greater distances, the opening is only partially overlapped and  $|S_{11}|$  starts to decrease.

$|S_{11}^d|$  of the substrate has different values for different standoff distances, which can be explained by the diverse characteristic impedances of the three VWGs, resulting in different reflection coefficients for the same substrate.

Models of VWGs with the substrate at the considered standoff distances using  $|S_{11}^d|$  provide  $\epsilon_r = 2.24$  if measurement uncertainties around  $\pm 0.05$ , due to limited mounting repeatability, are supposed. The agreement is acceptable with the value  $\epsilon_r = 2.33$  declared by the producer at 10 GHz and it also indirectly confirms the validity of the determined  $|S_{11}^d|$ .

Moreover, the proposed sensor measures a nearly constant contrast  $|S_{11}^m/S_{11}^d|$  for different standoff distances. The other outstanding features are the high contrasts  $|S_{11}^m/S_{11}^f|$  and  $|S_{11}^d/S_{11}^f|$  which result from the application of the calibration reducing the reflection from the sensor itself.

The minimum gap width resolution between metal strips can be determined by the same level of  $|S_{11}|$  compared to  $|S_{11}^d|$  in the middle of the SUT. The resolution equals 1.9 mm at the standoff distance of 1 mm, see Fig. 4, which also corresponds to a minimum resolution for the tracking of SUT local properties.

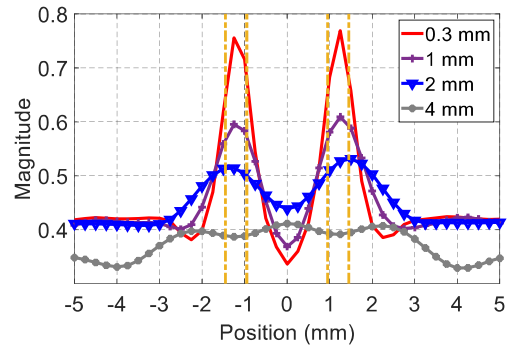


Fig. 5. Magnitude of the measured  $S_{11}$  of the proposed sensor with 0.5-mm-wide metal strips and a gap of 1.9 mm between them (indicated by the vertical lines) at 80 GHz.

TABLE II  
STATE OF THE ART SENSORS

Ref.	Frequency [GHz]	Standoff dist. [mm ( $\lambda_0$ )]	Spatial resol. [mm]	Contrast $ S_{11}^m/S_{11}^d $
[4]	24	1 (0.08)	5	4.3
[5]	24	1 (0.08)	5	4.4
[6]	0.426	1 (0.0014)	5	1.6
[7]-1*	3.99	4 (0.05)	5	14
[7]-2*	4.05	2 (0.027)	5	8.9
This work	80	0.3÷4 (0.08÷1.07)	1.9 at 2 mm	>20
[7]-1*-LA probe				
[7]-2*-Helix probe				

The second scanned SUT contains two narrow 0.5-mm-wide strips with a gap of 1.9 mm. Minimum spatial resolutions of the new sensor can be determined from Fig. 5. Two individual strips with a gap between them can be clearly distinguished, even for the 2-mm distance of the sample from the sensor.

On the other hand, in standard sensors, e.g., a rectangular tapered sensor, the reflection coefficient is measured at the end of the open-ended metallic waveguide. The values of  $|S_{11}^m|$  and  $|S_{11}^d|$  measured by this sensor (first sensor in Table I) show non-monotonic distance dependences which means that they are incorrect (as well as the contrasts  $|S_{11}^m/S_{11}^f|$ ,  $|S_{11}^d/S_{11}^f|$ , and  $|S_{11}^m/S_{11}^d|$  of the images obtained) and suffering from the mutual interference of the relatively high reflection from the end of sensor  $S_{11}^f$  and the reflection from the sample.

The excellent properties of the new sensor are shown in comparison with the state-of-the-art sensors in Table II.

#### IV. CONCLUSION

A new application of the rectangular waveguide sensor with a choke for imaging in the W-band has been proposed. The sensor can scan the image of the SUT up to at least a 1.07  $\lambda_0$  standoff distance. The calibration technique suppressing the reflection coefficient of the sensor itself has been derived and applied. Due to this technique, the high-contrast of the image above 26 dB and the correct amplitudes of local reflection coefficients can be determined in the plane of the SUT. The spatial resolution and the minimum resolution for the tracking of SUT local properties of 1.9 mm at 80 GHz are achieved at 2- and 1-mm standoff distances, respectively. The outstanding features of the new sensor surpass the properties of the state-of-the-art sensors.

## REFERENCES

- [1] A. Baskakova and K. Hoffmann, "Novel waveguide sensors for contactless ultrashort-distance measurements," *IEEE Trans. Microw. Theory Techn.*, early access, Sep. 3, 2021, doi: [10.1109/TMTT.2021.3107503](https://doi.org/10.1109/TMTT.2021.3107503).
- [2] P. Mehta, K. Chand, D. Narayanswamy, D. G. Beetner, R. Zoughi, and W. V. Stoecker, "Microwave reflectometry as a novel diagnostic tool for detection of skin cancers," *IEEE Trans. Instrum. Meas.*, vol. 55, no. 4, pp. 1309–1316, Aug. 2006, doi: [10.1109/TIM.2006.876566](https://doi.org/10.1109/TIM.2006.876566).
- [3] K. M. Donnell, M. A. Abou-Khousa, M. Belayneh, and R. Zoughi, "Dual-loaded modulated dipole scatterer as an embedded sensor," *IEEE Trans. Instrum. Meas.*, vol. 60, no. 5, pp. 1884–1892, May 2011, doi: [10.1109/TIM.2010.2091184](https://doi.org/10.1109/TIM.2010.2091184).
- [4] S. Kharkovsky, A. C. Ryley, V. Stephen, and R. Zoughi, "Dual-polarized microwave near-field reflectometer for non-invasive inspection of carbon fiber reinforced polymer (CFRP) strengthened structures," in *Proc. IEEE Instrum. Meas. Technol. Conf.*, Apr. 2006, pp. 2108–2111, doi: [10.1109/IMTC.2006.328499](https://doi.org/10.1109/IMTC.2006.328499).
- [5] M. A. Abou-Khousa, M. S. Rahman, and X. Xingyu, "Dual-polarized microwave imaging probe," *IEEE Sensors J.*, vol. 19, no. 5, pp. 1767–1776, Mar. 2019, doi: [10.1109/JSEN.2018.2882695](https://doi.org/10.1109/JSEN.2018.2882695).
- [6] M. R. Ramzi, M. Abou-Khousa, and I. Prayudi, "Near-field microwave imaging using open-ended circular waveguide probes," *IEEE Sensors J.*, vol. 17, no. 8, pp. 2359–2366, Apr. 2017, doi: [10.1109/JSEN.2017.2669301](https://doi.org/10.1109/JSEN.2017.2669301).
- [7] M. A. Abou-Khousa, K. T. M. Shafi, and X. Xingyu, "High-resolution UHF near-field imaging probe," *IEEE Trans. Instrum. Meas.*, vol. 67, no. 10, pp. 2353–2362, Apr. 2018, doi: [10.1109/TIM.2018.2815437](https://doi.org/10.1109/TIM.2018.2815437).
- [8] O. Malyuskin and V. F. Fusco, "High-resolution microwave near-field surface imaging using resonance probes," *IEEE Trans. Instrum. Meas.*, vol. 65, no. 1, pp. 189–200, Jan. 2016, doi: [10.1109/TIM.2015.2476277](https://doi.org/10.1109/TIM.2015.2476277).
- [9] W. Saleh, N. Qaddoumi, and M. Abu-Khousa, "Preliminary investigation of near-field nondestructive testing of carbon-loaded composites using loaded open-ended waveguides," *Compos. Struct.*, vol. 62, nos. 3–4, pp. 403–407, Jan. 2003.
- [10] A. Hagelauer, M. Wojnowski, K. Pressel, R. Weigel, and D. Kissinger, "Integrated systems-in-package: Heterogeneous integration of millimeter-wave active circuits and passives in fan-out wafer-level packaging technologies," *IEEE Microw. Mag.*, vol. 19, no. 1, pp. 48–56, Jan./Feb. 2018, doi: [10.1109/MMM.2017.2759558](https://doi.org/10.1109/MMM.2017.2759558).
- [11] G. J. Scalzi, A. J. Slobodnik, Jr., and G. A. Roberts, "Network analyzer calibration using offset shorts," *IEEE Trans. Microw. Theory Techn.*, vol. MTT-36, no. 6, pp. 1097–1100, Jun. 1988, doi: [10.1109/22.3638](https://doi.org/10.1109/22.3638).
- [12] G. Bryant, "Vector analyzers," in *Principles of Microwave Measurements*. London, U.K.: Peregrinus on behalf of Institution of Electrical Engineers, 1993, pp. 88–101.

## 4.4 An Interferometric Sensor for Scanning Microwave Microscopy Application

**This chapter is a version of the published manuscript:**

**A. Baskakova**, G. Stella and K. Hoffmann, “An Interferometric Sensor for Scanning Microwave Microscopy Application,” in *2018 Asia-Pacific Microwave Conference (APMC)*, Kyoto, Japan, 2018, pp. 1232–1234, doi: 10.23919/APMC.2018.8617173.

**Connection to my Ph.D. thesis:**

This chapter proposes a new approach to interferometric transmission measurement for scanning microwave microscopy with the new interferometric sensor based on the Wilkinson power divider concept. The main idea of the proposed concept is to use a crosstalk signal as the reference signal to create destructive interference at certain frequencies. This can be achieved by using a new component, in the form of a microstrip Wilkinson power divider using cascaded pairs of line length and interconnecting resistors, to extend the bandwidth. The optimization procedures based on CST and AWR simulations are used to find the values of the resistors and length of lines for each section. The system has been experimentally investigated in the frequency band of 45 MHz to 26 GHz. The new sensor makes it possible to reduce the uncertainty of the reflection coefficient measurements approximately 40 times, when compared to standard VNA reflection measurement, allowing fast measurements with a VNA IF bandwidth of 30 kHz.

# An Interferometric Sensor for Scanning Microwave Microscopy Application

Aleksandra Baskakova, Giuseppe Stella and Karel Hoffmann

Czech Technical University in Prague  
Czech Republic  
aleksandra.baskakova@fel.cvut.cz

**Abstract** — The development of an interferometric sensor for scanning microwave microscopy is proposed. The structure is based on the concept of Wilkinson power divider; by using multistage sections of microstrip lines and resistors the operational bandwidth is increased. The optimization of dimension parameters and resistors values is discussed. The sensor was experimentally investigated in frequency band 45 MHz to 26 GHz. 40 times reduction of the reflection coefficient measurement uncertainty compared to standard VNA reflection measurement was achieved.

**Index Terms** — Scanning probe microscopy, interferometry, on wafer microwave measurement, impedance measurement.

## I. INTRODUCTION

The development of new materials and device structures based on nanostructures and fabricated on chips in wafers requires new measurement approaches for precise broadband measurement and imaging of their electromagnetic properties. These approaches face demands for measurement of high impedances much larger than conventional reference impedance of the measurement system, which leads to the problem of mismatching and poor accuracy of measurements [1].

Scanning Microwave Microscope (SMM) in combination with a Vector Network Analyzer (VNA) allows to measure characteristics of nanostructures in high spatial resolution [2]. Different SMM-measurement methods have been already presented, [3]-[7]. The most common methods use the interferometric approaches. However, they make possible measurement only at one frequency after a calibration.

A new wideband interferometric transmission measurement approach for SMM with a possibility of simultaneous measurements on a number of different frequencies was proposed in [8]. At certain frequencies the transmission coefficient has deep minima, which are very sensitive to changes of high impedances seen by the probe tip. The values of the impedances can be calculated from the transmission coefficient of the sensor in cascade with an amplifier. An amplifier with a proper gain compensates attenuation in minima. The arrangement enables to reduce significantly the noise of the VNA, which considerably decreases maximum measurable values of impedances in standard reflection coefficient measurements. The deeper the minima, the deeper the noise suppression is.

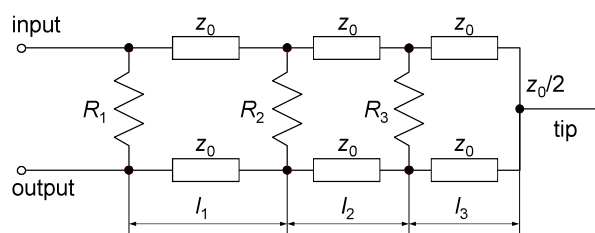


Fig. 1. General circuit of the interferometric sensor with three sections.

The purpose of the article is to demonstrate a new sensor for SMM based on the approach from [8]. The paper presents an improved structure with wider operating bandwidth and more frequency measuring points. The improvement of measurement stability compared with direct measurement by VNA is shown as well.

## II. OPTIMIZATION

Cohn in [9] suggested to increase the bandwidth of a power divider by using cascaded pairs of line length and interconnecting resistors. This approach was applied to the interferometric sensor. We used three sections of lines with the same impedance and resistors with different values, Fig. 1. Values of the resistors and lengths of the lines were found by an optimization procedure focused on reaching equal and deep interference minima.

The optimization procedure was done with AWR Microwave Office (AWR) and CST Microwave Studio (CST) software. It was necessary to derive:

- a circuit structure of the sensor with discontinuities,
- an equivalent circuit of the resistor.

The layout of the sensor with discontinuities designed in AWR is shown in Fig. 2. It was observed that coupling between the lines results in a degradation of the sensor performance. Therefore, it was minimized by bending the microstrips between the resistors. They were shaped with a 90-degree angle between each other.

A precise 3D model of the resistor 0402 dimensions was created and simulated in CST. The simulation was done for a mounting case, which is depicted in Fig. 3a, with the flipped arrangement of the resistor to decrease parasitic inductances.

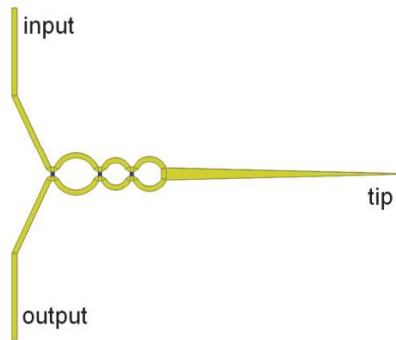


Fig. 2. The layout of the sensor (AWR model).

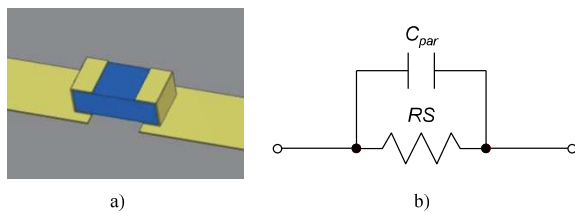


Fig. 3. Model of the resistor simulated in CST placed between lines in series (a) and the equivalent circuit (b).

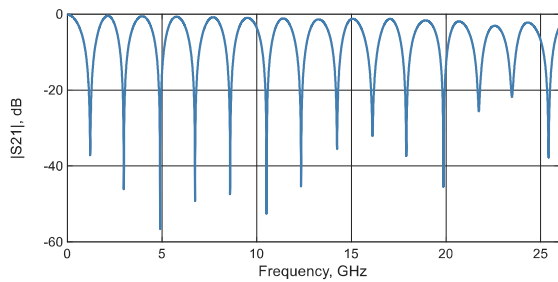


Fig. 4. Transmission coefficient of the proposed sensor (AWR).

Reference planes were considered at the edges of the component. Then AWR and curve fitting techniques were used to find an equivalent circuit of the resistor, Fig. 3b. It consists of a thin film resistor model with corresponding dimensions of the package and a surface resistivity, and a parasitic capacitance  $C_{par} = 0.039$  pF connected in parallel. Two T-junctions were added to connect the equivalent circuit between the microstrips in Fig. 2. No coupling between the microstrips was supposed in this arrangement.

The sensor circuit structure was optimized in AWR. However, the goal to get equivalent and deep minima in the whole frequency band has not been fully achieved yet, see Fig. 4. The optimized lengths of the sections  $l_1$ ,  $l_2$  and  $l_3$  are 7.4 mm, 4.5 mm, and 5.2 mm, respectively. The values of the resistors are  $R_1 = 2 \Omega$ ,  $R_2 = 91 \Omega$ , and  $R_3 = 110 \Omega$ .

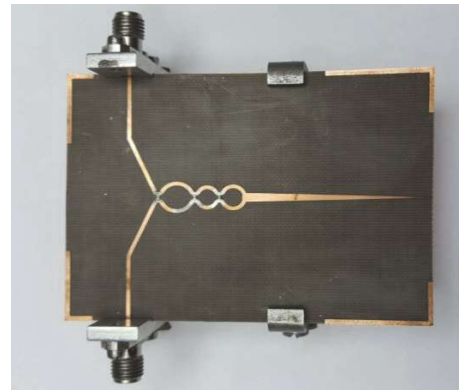


Fig. 5. Photo of the sensor with dimensions 50x70 mm.

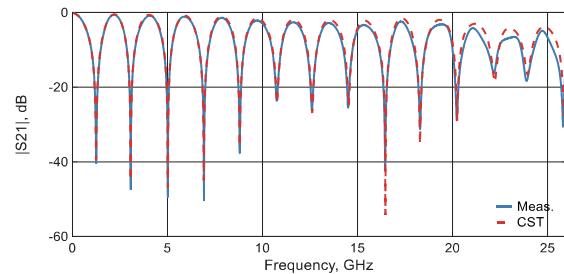


Fig. 6. Simulated (dashed lines) vs measured (solid lines) parameters of the sensor.

### III. EXPERIMENTAL VERIFICATION AND DISCUSSION

The final structure of the sensor was simulated in CST and fabricated on 0.254 mm CuClad 233 substrate, see Fig. 5. Its parameters were measured in frequency band 45 MHz to 26 GHz on Agilent PNA E8364A VNA calibrated by Agilent 85052C 3.5 mm Calibration Kit in reference planes of SMA connectors. The simulated and measured results, depicted in Fig. 6, are in a good agreement.

The new sensor was tested with respect to its ability to suppress the noise of the VNA and simultaneously the uncertainty of measurement of high impedances. Therefore, an SMA to microstrip adapter was connected to the sensor at the tip of the microstrip which slightly shifted frequencies of minima. The measurement was done at frequency 3.92 GHz, where the minimum level of the sensor with the added SMA adapter is around -50 dB.

The VNA was first calibrated at the reference planes of its test cables. IF bandwidth was set to 30 kHz. Then a cascade of the sensor and Mini Circuits amplifiers ZX60-8008E-S+, Gali 1+ and Gali 2+ with a total gain 48.5 dB was connected between the test cables. The second step of the calibration at the reference plane of the added SMA-microstrip adapter was applied. A 3-port error model with 3 constants  $C_1$ ,  $C_2$ , and  $C_3$  determined in accordance with [10] was used.

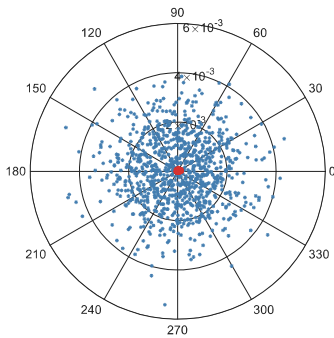


Fig. 7. Spreading of the 1000 values of the measured reflection coefficient of the direct method (blue markers) and interferometric method (red markers).

After calibration, 1000  $S_{21}$  measurements corresponding to open end of the added SMA-microstrip were collected and corresponding reflection coefficient  $\Gamma_x$  was calculated, in accordance with [10], by formula:

$$\Gamma_x = \frac{S_{21} - C_1}{C_2 + C_3 S_{21}}. \quad (1)$$

To compare these interferometric measurement results with the results of the direct VNA reflection coefficient measurement, the VNA was calibrated for one port measurement with SMA(f)-SMA(f) adapter connected to the test cable using the same calibration kit. 1000 reflection coefficients were measured at the same frequency.

The spreading of the values of the reflection coefficient around the mean value for both methods was defined as

$$\rho[\Gamma_{x_i}] = \Gamma_{x_i} - \frac{1}{N} \sum_{j=1}^N \Gamma_{x_j}, \quad (2)$$

where N is a number of measurements, and depicted in Fig. 7.

The standard deviations in the mean of the reflection coefficients determined by both methods were calculated [11], see Table I. It can be seen that the new sensor suppresses the uncertainty of the measurement about 40 times in comparison with the direct method of the reflection coefficient measurement.

TABLE I.  
STANDART DEVIATION OF MEASURED REFLECTION COEFFICIENTS

Method	Real part of $\Gamma_x$	Imaginary part of $\Gamma_x$
Direct	$4.4159 \cdot 10^{-5}$	$4.4157 \cdot 10^{-5}$
Interferometric	$1.3610 \cdot 10^{-6}$	$1.0221 \cdot 10^{-6}$

#### IV. CONCLUSION

A new structure of interferometric sensor, which can be applied for SMM measurements, was analyzed, realized and measured in frequency band 45 MHz up to 26 GHz. The sensor

contains multistage sections of microstrip lines and resistors extending the operating bandwidth. The optimization procedures based on CST and AWR simulations were used to find the values of resistors and length of lines for each section.

Significant improvement, more and deeper minima, was achieved in comparison with original sensor from [8]. The new sensor makes possible to reduce the uncertainty of the reflection coefficient measurements about 40 times compared to standard VNA reflection measurement allowing fast measurements with VNA IF bandwidth 30 kHz.

#### ACKNOWLEDGEMENT

This work was funded from the European Union's Horizon 2020 research and innovation programme 2014-2018 under the Marie Skłodowska-Curie grant agreement No. 675683.

#### REFERENCES

- [1] P.R. Bandaru, "Electrical properties and applications of carbon nanotube structures," *Journal of Nanoscience and Nanotechnology*, vol. 7, pp. 1 – 29, 2007.
- [2] S. M. Anlage, V. V. Talanov, and A. R. Schwartz, "Principles of nearfield microwave microscopy," *Scanning Probe Microscopy: Electrical and Electromechanical Phenomena at the Nanoscale*, S. Kalinin and A. Gruverman, Eds. New York, Springer Sci., pp. 215 – 253, 2007.
- [3] R. J. Gutmann, J. M. Borrego, P. Chakrabarti, Ming-Shan Wang, "Microwave Scanning Microscopy for Planar Structure Diagnostics," *IEEE MTT-S International Microwave Symposium Digest*, vol. 1, pp. 281 – 284, 1987.
- [4] B. J. Feenstra, C. P. Vlahacos, A. S. Thanawalla, D. E. Steinhauer, S. K. Dutta, F. C. Wellstood, S. M. Anlage, "Near-field scanning microwave microscopy: measuring local microwave properties and electric field distributions," *IEEE MTT-S International Microwave Symposium Digest*, vol. 2, pp. 965 – 968, 1998.
- [5] M. Tabib-Azar and J.L. Katz, "Evanescence microwaves: A novel super-resolution noncontact nondestructive imaging technique for biological applications," *IEEE Trans. on Instrumentation and Measurement*, vol. 48, no. 6, pp.1111-1116, 1999.
- [6] H. Bakli, K. Haddadi, and T. Lasri, "Interferometric Technique for Scanning Near-Field Microwave Microscopy Applications," *IEEE Trans. Instrumentation & Measurement*, vol. 63, no. 5, pp. 1281-1286, May 2014.
- [7] S. Fabiani, A. Lucesoli, A. Di Donato, D. Mencarelli, G. Venanzoni, A. Morini, T. Rozzi, and M. Farina, "Dual-Channel Microwave Scanning Probe Microscopy for Nanotechnology and Molecular Biology", *Proc. IEEE Eur. Microw. Conf. (EuMC)*, 2010, pp. 767–770.
- [8] K. Hoffmann and A. Baskakova, "A new Interferometric Sensor for Scanning Near-Field Microwave Microscopy," *2017 ARFTG Int. Conference*, 2017.
- [9] S. B. Cohn, "A Class of Broadband Three-Port TEM-Mode Hybrids," *IEEE Trans. on Microwave Theory and Tech.*, vol. 16, no. 2, 1968.
- [10] M. Randus, K. Hoffmann, "Microwave Impedance Measurement for Nanoelectronics," *Radioengineering*, vol. 20. No. 1, April 2011, pp. 276-283.
- [11] N. Ridler and M. Salter, "Evaluating and expressing uncertainty in complex S-parameter measurements," *IEEE 56th. ARFTG Conference Digest-Fall*, vol. 38, pp. 1-13, 2000.

## 4.5 Design of Microstrip Dual-Mode Impedance Transformers

**This chapter is a version of the published manuscript:**

**A. Baskakova**, and K. Hoffmann, “Design of Microstrip Dual-Mode Impedance Transformers,” in *IEEE Microwave and Wireless Components Letters*, vol. 29, no. 2, pp. 86–88, Feb. 2019, doi: 10.1109/LMWC.2018.2887313.

**Connection to my Ph.D. thesis:**

The EM analysis of the interferometric sensor from [section 4.4](#) shows that the parts of the sensor with placed resistors are coupled resulting in the degradation of sensor performance. To avoid this effect another configuration of the interferometric sensor is proposed utilizing coupled lines instead of bent microstrip line sections. The simpler the shape of the sensor (with fewer discontinuities), the easier it can be described in software and optimized afterwards. Since the new sensor design is relatively plain, only the part with the connection of the  $50\ \Omega$  microstrip lines and coupled line can bring any mismatching of impedances. This mismatching can be suppressed using a new dual-mode impedance transformer which should match single-ended impedance  $Z_0$  to general impedances of even mode  $Z_{0e}$  and odd mode  $Z_{0o}$  of a coupled line. For this purpose, a new, unique four-port component is investigated and developed in this chapter. A new dimension correction approach is derived. Two transformers between  $50\ \Omega$  microstrips and microstrip coupled lines with even/odd impedances of  $100 / 68\ \Omega$  and  $36 / 27\ \Omega$ , respectively, are built. The concept is experimentally verified at the frequency band 0.01–16 GHz.

# Design of Microstrip Dual-Mode Impedance Transformers

Aleksandra Baskakova<sup>1</sup>, Student Member, IEEE, and Karel Hoffmann, Senior Member, IEEE

**Abstract**—new four-port component, dual-mode impedance transformer for wideband matching of two microstrip lines with equal characteristic impedance and a coupled microstrip line with general even- and odd-mode impedances, is proposed. Practical realization problems are discussed and a new dimension correction approach is derived. Two transformers between 50- $\Omega$  microstrips and microstrip coupled lines with even/odd impedances 100  $\Omega$ /68  $\Omega$  and 36  $\Omega$ /27  $\Omega$ , respectively, were built. The concept was experimentally verified at the frequency band 0.01–16 GHz.

**Index Terms**—Coupled lines, impedance matching, tapered lines, transformer.

## I. INTRODUCTION

IMPEDANCE matching is an important technique commonly used in the design of many microwave circuits [1]. A wider frequency band can be achieved using multisection transformers. Binomial multisection matching transformers enable a flat response near the design frequency. For a given number of sections, greater frequency bandwidth can be achieved using Chebyshev multisection matching transformers, where the bandwidth is optimized at the expense of a passband ripple. In both multisection transformers, bandwidth increases with more of sections. The limit of an infinite number of sections is achieved by using a continuously tapered line. There are different types of tapered line impedance transformers such as exponential, triangular, or Klopfenstein tapers [1]. All of these impedance transformers match or transform impedances supposing only single-mode propagation along a transmission line.

Dual-mode tapered-coupled line impedance transforming structures have been proposed for applications in directional couplers [2]–[4]. In these theoretical papers, impedances of the even mode  $Z_{0e}$  and the odd mode  $Z_{0o}$  along the structure are solely linked with connected line impedance  $Z_0$  so that  $Z_0^2 = Z_{0e}Z_{0o}$ , and nonzero reflection coefficients of the even and odd modes are considered. Realizations in stripline are supposed [3].

In some applications where coupled lines are applied, the more general type of dual-mode impedance matching

Manuscript received September 21, 2018; accepted December 10, 2018. Date of publication January 8, 2019; date of current version February 14, 2019. This work was supported by the European Union's Horizon 2020 Research and Innovation Programme 2016–2020 under the Marie Skłodowska-Curie under Grant 675683. (Corresponding author: Aleksandra Baskakova.)

The authors are with the Department of Electromagnetic Field, Faculty of Electrical Engineering, Czech Technical University in Prague, 166 27 Prague, Czech Republic (e-mail: aleksandra.baskakova@fel.cvut.cz).

Color versions of one or more of the figures in this paper are available online at <http://ieeexplore.ieee.org>.

Digital Object Identifier 10.1109/LMWC.2018.2887313

1531-1309 © 2019 IEEE. Personal use is permitted, but republication/redistribution requires IEEE permission. See [http://www.ieee.org/publications\\_standards/publications/rights/index.html](http://www.ieee.org/publications_standards/publications/rights/index.html) for more information.

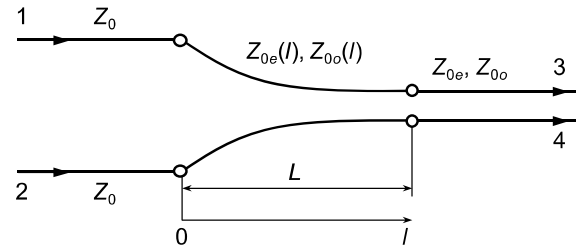


Fig. 1. Proposed dual-mode impedance transformer.

transformers may be useful, e.g., in a new type of three-port sensor for scanning microwave microscopy [5]. In principle, these components use a signal formed by an interference of both even- and odd-mode signals. A dual-mode matching transformer can improve their properties suppressing unwanted simultaneous reflections of both modes by the reduction of discontinuities between microstrip lines and a microstrip coupled line.

The purpose of this letter is to demonstrate that the realization of a four-port component for wideband simultaneous matching of two microstrip lines with characteristic impedance  $Z_0$  and a coupled microstrip line with general impedances  $Z_{0e}$  and  $Z_{0o}$  is possible. Practical recommendations for the determination of structure dimensions in microstrip technology are provided.

## II. DESIGN OF DUAL-MODE IMPEDANCE TRANSFORMERS

The design of a dual-mode impedance transformer is based on the theory of small reflections [1], namely, continuously tapered lines. Applying the conventional single-mode approach simultaneously to both even and odd modes of a coupled line enables to design a dual-mode microstrip impedance transformer, which matches a single-ended impedance  $Z_0$  to general impedances  $Z_{0e}$  and  $Z_{0o}$  of a coupled line (see Fig. 1). According to [1], the characteristic impedance of the tapered line is variable with the position along the line. We utilized the approach on both modes using the exponential functions

$$Z_{0e}(l) = Z_0 e^{\frac{l}{L} \ln \frac{Z_{0e}}{Z_0}}, \quad Z_{0o}(l) = Z_0 e^{\frac{l}{L} \ln \frac{Z_{0o}}{Z_0}} \quad (1)$$

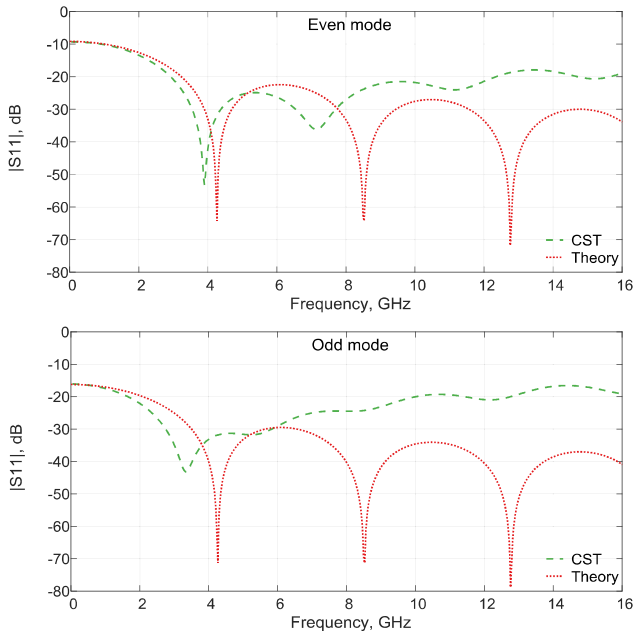
where  $l$  is a position along the coupled tapered line,  $L$  is its length,  $Z_0$  is an impedance of the single-ended microstrip line, and  $Z_{0e}$  and  $Z_{0o}$  are impedances of the microstrip coupled line.

Employing (1),  $Z_{0e}$  and  $Z_{0o}$  impedances in each chosen position  $l$  can be calculated, and corresponding widths of lines ( $W$ ) and the slot between them ( $S$ ) can be determined [6]. Spline approximation can be applied to eliminate the influence of a step in width discontinuities.



TABLE I  
 SPECIFICATION OF THE IMPEDANCE TRANSFORMERS

	$Z_{0e}, \Omega$	$Z_{0o}, \Omega$	$S, \text{mm}$	$W, \text{mm}$	$Z_0, \Omega$	$W_0, \text{mm}$
Above 50 $\Omega$	100	68	0.37	0.57		
Below 50 $\Omega$	36	27	0.21	2.64	50	1.49


 Fig. 2.  $|S_{11e}|$  and  $|S_{11o}|$  theoretical versus simulation in CST results for the transformer with impedances  $Z_{0e}$  and  $Z_{0o}$  both above 50  $\Omega$ . Dimensions  $W$  and  $S$  considered in the plane perpendicular to the plane of symmetry.

As an example, two general dual-mode microstrip impedance transformers with impedances not limited by  $Z_0^2 = Z_{0e}Z_{0o}$  condition from [2]–[4] were designed. The length of the transformers was  $L = 25$  mm. A CuClad 0.508-mm substrate with  $\epsilon_r = 2.33$  was supposed. The characteristic impedance  $Z_0$ , the width of the microstrip line  $W_0$ , and general impedances of the coupled lines with their widths and slots are shown in Table I. The input reflection coefficients of each impedance transformer were computed using a formula from [1] applied to both modes

$$\begin{aligned} |S_{11e}| &= \frac{\ln Z_{0e}/Z_0}{2} e^{-j\beta_e L} \frac{\sin \beta_e L}{\beta_e L} \\ |S_{11o}| &= \frac{\ln Z_{0o}/Z_0}{2} e^{-j\beta_o L} \frac{\sin \beta_o L}{\beta_o L} \end{aligned} \quad (2)$$

where  $\beta_e$  and  $\beta_o$  are propagation constants of even and odd modes.

Both transformers were simulated in CST Microwave Studio. The dimensions  $W$  and  $S$  were considered in planes perpendicular to the plane of symmetry of the transformers since it is common in homogeneous coupled lines. However, Fig. 2 confirms that the theoretical results determined by (2) and the results of simulations do not agree.

Animations of the electromagnetic (EM) field in the transformer structure clarified the problem. The real EM field distribution in the structure was significantly different from

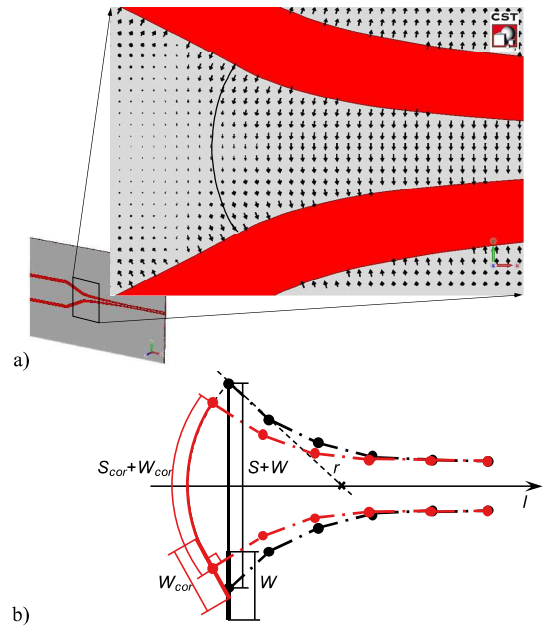


Fig. 3. (a) Propagation of the EM wave along the structure on the top of the substrate. (b) Sketch of the correction of the dimensions (microstrip center lines are displayed).

the assumed perpendicular to the plane of symmetry EM field distribution in the coupled lines [see Fig. 3(a)]. The  $E$ -field lines between microstrips were perpendicular to their edges and were shaped like arcs instead of the supposed linear shape. Therefore, some dimension corrections were necessary.

We approximated the arcs using circular arcs with the radii corresponding to the distance between the coordinates under correction and the intersections of the plane of symmetry and the lines connecting that coordinate with the nearest one [see Fig. 3(b)]. The corrected slot width  $S_{\text{cor}}$  was considered as the length of the circular arc supposing  $S_{\text{cor}} = S$ . To respect the  $E$ -field distribution, the width of lines  $W_{\text{cor}}$  had to be measured in the direction perpendicular to the center line of the microstrip, supposing  $W_{\text{cor}} = W$ .

The parameters  $W$  and  $S$  were calculated at a frequency of 10 GHz. The limit of the ratio of  $S$  and the substrate thickness did not allow to calculate  $S$  for  $l$  from 0 to 0.5 mm [6]. For this low-coupled part of the transformer, a linear extrapolation was used instead. This correction method was applied for both dual-mode impedance transformers, and CST simulations were repeated. Results are depicted in Figs. 4 and 5. It is clear that the dimension correction brought simulation results significantly closer to the theoretical results.

### III. EXPERIMENTAL INVESTIGATION

Two dual-mode microstrip impedance transformers for two coupled lines specified in Table I with corrected dimensions were designed on a 0.508-mm CuClad 233 substrate (see Fig. 6). The 20-mm pieces of homogeneous microstrip lines and homogeneous coupled lines, respectively, were added at both ends of the transformers so that the time gating measurement techniques could be applied. Two samples of each transformer were made for the measurement of even- and

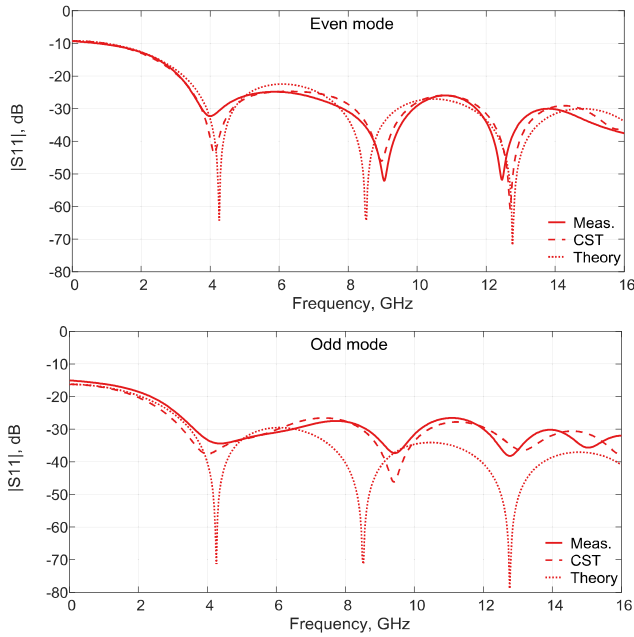


Fig. 4. Measured, simulated, and theoretical reflection coefficients of the impedance transformer with the final impedances above  $50\ \Omega$ .

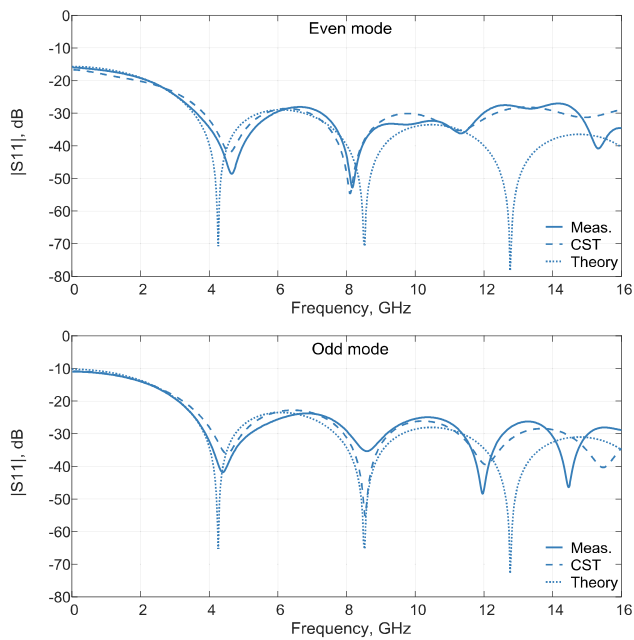


Fig. 5. Measured, simulated, and theoretical reflection coefficients of the impedance transformer with the final impedances below  $50\ \Omega$ .

odd-mode reflection coefficients. At the end of the coupled line of each transformer, 0402 resistors with values corresponding to even- and odd-mode impedances were mounted.

Reflection coefficients at the input of microstrip lines were measured using an R&S ZVA-67 vector network analyzer set for true common and true differential mode measurements at frequency band 10 MHz–16 GHz. Calibration with an R&S ZV-Z52 E-cal calibration unit at the reference plane of SMA connectors was applied. Then, the time-gating technique

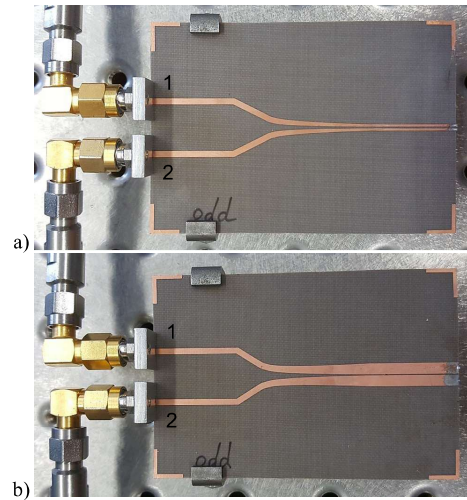


Fig. 6. Experimental samples of two transformers with  $Z_{0c}$  and  $Z_{0o}$  impedances both (a) above and (b) below  $50\ \Omega$ .

was used to eliminate the influences of the SMA-microstrip adapters and parasitics of SMD resistors on the measurement of the reflection coefficients of the samples.

The theoretical, simulated in CST, and measured results are depicted in Figs. 4 and 5. The characteristics reasonably correspond to each other. The differences between the simulated and measured curves may be because of the etching technological limits. Also, at higher frequencies, the correspondence between theory and both simulations and measurements slightly degraded, probably due to dispersion properties of the structure not taken into account in (1). Radiation of SMA-microstrip adapters may have played a role.

#### IV. CONCLUSION

A design of a new dual-mode microstrip impedance transformer for simultaneous matching of even- and odd-mode general impedances of a coupled line to a characteristic impedance of connected microstrip lines was proposed. A novel correction method for the determination of transformer dimensions was derived and verified by simulations and experiments.

#### REFERENCES

- [1] D. M. Pozar, "Impedance matching and tuning," in *Microwave Engineering*, 4th ed. New York, NY, USA: Wiley, 2011, pp. 250–263.
- [2] R. H. DuHamel and M. E. Armstrong, "The tapered-line magic-T," in *Proc. 15th Annu. Symp. USAF Antenna Res. Develop. Program*, Monticello, IL, USA, 1965.
- [3] F. Arndt, "Tables for asymmetric Chebyshev high-pass TEM-mode directional couplers," *IEEE Trans. Microw. Theory Technol.*, vol. MTT-18, no. 9, pp. 633–638, Sep. 1970.
- [4] R. Levy, "Tables for asymmetric multi-element coupled-transmission-line directional couplers," *IEEE Trans. Microw. Theory Technol.*, vol. MTT-12, no. 3, pp. 275–279, May 1964.
- [5] K. Hoffmann and A. Baskakova, "A new interferometric sensor for scanning near-field microwave microscopy," in *Proc. 89th ARFTG Microw. Meas. Conf. (ARFTG)*, Honolulu, HI, USA, Jun. 2017, pp. 1–4.
- [6] M. Kirschning and R. H. Jansen, "Accurate wide-range design equations for the frequency-dependent characteristic of parallel coupled microstrip lines," *IEEE Trans. Microw. Theory Technol.*, vol. MTT-32, no. 1, pp. 83–90, Jan. 1984.

## 4.6 Advanced Configuration of the Interferometric Sensor

### Sensor

In this chapter, the advanced configuration of the interferometric sensor based on coupled lines and the impedance transformer developed in [section 4.5](#) is proposed.

The schematic of the measuring scanning microwave microscope system is presented in [Figure 4.1](#). The transmission coefficient has deep minima at the frequencies of interference which are very sensitive to changes of high impedances as seen by the probe tip. The values of the impedances can be calculated from the transmission coefficient of the sensor in cascade with an amplifier. An amplifier with proper gain compensates for attenuation in minima. The arrangement enables the noise of the VNA to be reduced significantly, which considerably decreases maximum measurable values of impedances in standard reflection coefficient measurements. The deeper the minima, the deeper the noise suppression is.

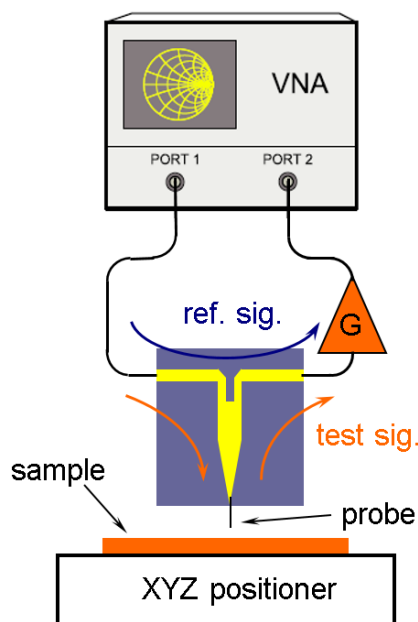


*Figure 4.1: Schematic of the measurement system*

The principle of the method can be explained by an analysis of the four-arm symmetrical networks where the input wave is broken into even and odd modes [45]. The measurement signal goes from port 1 to the sensor where the modes start to propagate. The even mode travels along the arms of the sensor to the end of the probe, and then reflects back. In contrary fashion, the odd mode propagates along the arms and, at the end of a coupled line, a short circuit for this mode occurs. Therefore, the odd mode has a shorter path. Ultimately, both signals are added. Due to the different lengths of the pathways, the signals destructively interfere at some frequencies. The resultant transmission between port 1 and port 2 has, therefore, deep minima on these frequencies. The number of these

frequencies in a frequency band depends on the electrical length of the line connected to the probe. The deepness of the minima can be controlled by making the reflection coefficient amplitude of the even and odd modes equal.

Considering that the parts of the sensor with placed resistors from [section 4.4](#) are coupled, they bring degradation of sensor performance. A problem in characterizing them sufficiently correctly arises. For full characterization of the structure in software, when optimizing its properties, the design of the sensor should be as simple as possible.

Another configuration of the interferometric sensor utilizing coupled lines, instead of bent microstrip line sections, is advantageous. The shape of the sensor is plain, with fewer discontinuities, therefore it can be more easily described in software and optimized afterwards.

The advanced configuration of the sensor is designed in CST Studio Suite and depicted in [Figure 4.2](#). The structure of the sensor was simulated using a 0.254 mm CuClad 233 substrate and lossy copper metallization in a frequency band ranging from 45 MHz to 18 GHz. The structure includes a number of improvements to suppress unwanted reflections and to modify sensor properties.

To decrease unwanted coupling between the ports, they are designed at the same plane (see [Figure 4.2 – 1](#)). An impedance transformer from [section 4.5](#) is applied to reduce impedance mismatch (see [Figure 4.2 – 2](#)). It transforms 50  $\Omega$  microstrip lines, with width  $W_0 = 1.49$  mm, to microstrip coupled lines with even/odd impedances 100 / 68  $\Omega$ , with the width of coupled line  $W = 0.57$  mm and gap  $S = 0.37$  mm. And finally, surface-mount device (SMD) resistors are replaced by a thin layer of resistive material with a resistance of 9 Ohm per square (see [Figure 4.2 – 3](#)). This technique allows the resistive layer to be deposited precisely on the place of interest with high tolerance, in comparison with the SMD component placement.

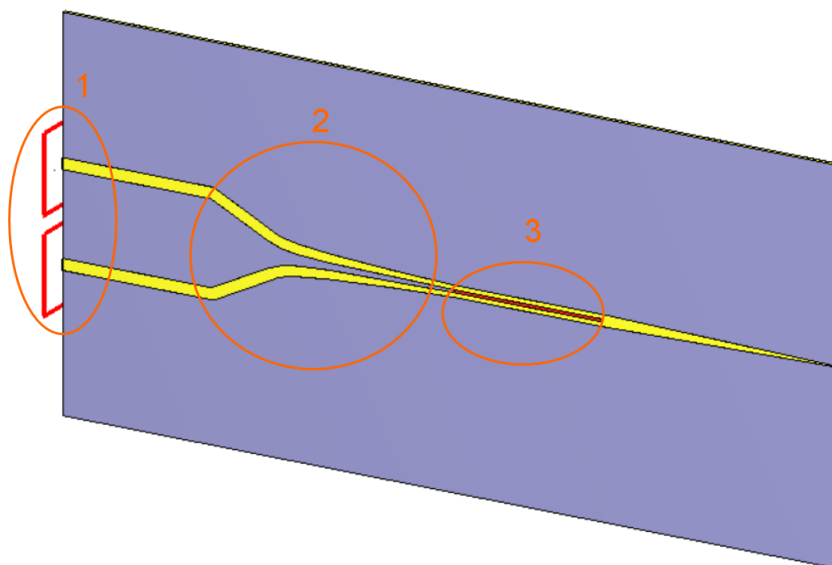


*Figure 4.2: Advanced interferometric sensor for SMM*

One of the main advantages of the approach is that the sensor is designed on a single substrate with no movable parts. Both interfering signals propagate only inside of the structure. Therefore, the sensor is not sensitive to the movements of interconnecting cables or the placement of SMD components.

The simulated transmission coefficient is depicted in [Figure 4.3](#). The minima of the sensor are similar for frequencies up to 15 GHz and equal to  $38 \pm 4.5$  dB. In principle, this arrangement allows the measurement system to be calibrated only once for all frequencies of the minima, which makes the system broadband and simple to use. The structure can be further optimized to achieve equal minima even for frequencies above 15 GHz.

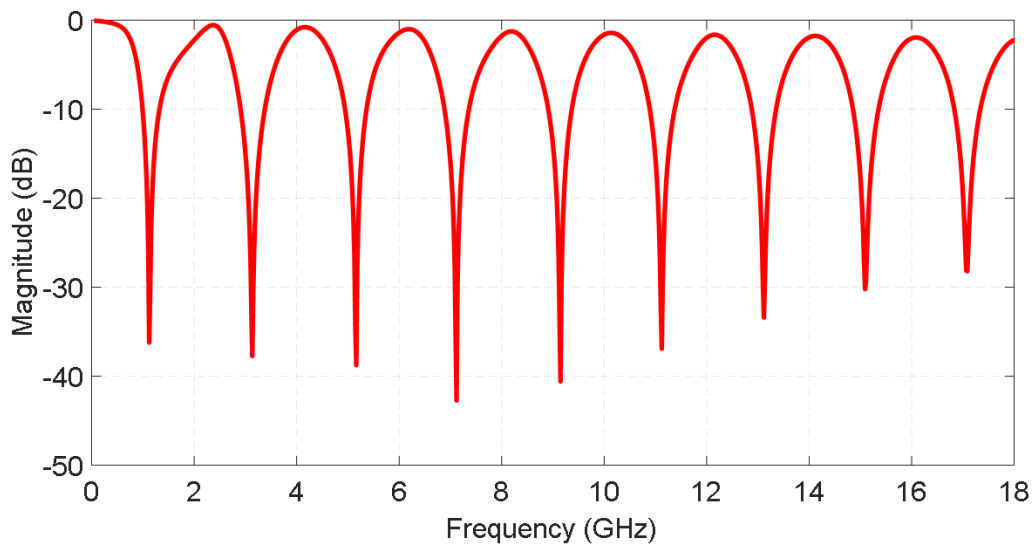


*Figure 4.3: Transmission coefficient of the advanced interferometric sensor*

However, I faced a problem in the realization of the structure, in particular, to find manufacturers who could apply a resistive layer to the substrate. It takes a well-designed technology to fill the gap between a coupled line with lossy material. Therefore, the fabrication of the structure is planned for the future.



This thesis provides theoretical, analytical and experimental analyses of new components for microwave distance and imaging measurements based on an interferometric approach. The state-of-the-art was presented with an emphasis on the advantages and limitations of contactless distance sensors, sensors for imaging purpose and scanning microwave microscopy systems.

The core part of the thesis starts with a proposal of a new design of a contactless ultrashort distance sensor based on an R100 waveguide with a choke flange in [section 4.1](#). It was experimentally investigated in the frequency band from 8 GHz to 12.4 GHz measuring reflection coefficients from 0 up to 20 mm. It was found that the sensor has a quasi-linear dependence of the measured reflection coefficient phase on the distance to a target with no ambiguities, which is a unique property for this particular application.

The design was extrapolated to the W-band in [section 4.2](#) to decrease the error in distance determination. In addition, the design, based on a circular waveguide sensor with choke, was introduced. A physical explanation and description of field behavior between the sensors and the target has been suggested and a corresponding, physically well-founded, equivalent circuit, based on a cascade of virtual waveguide (VWG)s with different dimensions, has been proposed. A new calibration correction method, based on the equivalent circuit, has been derived. The new method suppresses the influences of the reflection from the sensor itself, multi-reflections between the sensor and the target, variable wavelength in the vicinity of the sensor, and changes in the field configuration when one mode converts into another one. Only nine calibration measurements are necessary for measurements in the whole distance interval from 0 to 6 mm. Both sensors have been successfully experimentally verified. The sensors enable distances from zero to more than one and a half of the wavelength with maximum error below 0.9 % and 0.7 %, respectively, to be determined. In comparison with the state-of-the-art sensors, the new sensors enable about ten times fewer distance measurement errors to be achieved. Both new sensors are applicable in the wide frequency bandwidths 2 and 10 GHz.

While developing the theory for the distance sensor, I realized that its properties are beneficial for the imaging application. [Section 4.3](#) demonstrates the successful use of the rectangular distance sensor in W-band imaging. The sensor can scan the image of the SUT up to at least a  $1.07 \lambda_0$  standoff distance. The calibration technique suppressing

---

the reflection coefficient of the sensor itself has been applied. Due to this technique, the high-contrast of the image above 26 dB and the correct amplitudes of local reflection coefficients can be determined in the plane of the SUT. The spatial resolution, and the minimum resolution for the tracking of SUT local properties of 1.9 mm at 80 GHz, are achieved at 2- and 1-mm standoff distances, respectively. The outstanding features of the new sensor surpass the properties of the state-of-the-art sensors.

A new design of a measurement system for the measurement of the properties of extremely high impedance materials in the microwave region was proposed in [section 4.4](#). It consists of new circuit structures using the interferometric transmission measurement approach. The novel structure of an interferometric sensor, consisting of multi-stage sections of microstrip lines and resistors, was analyzed, realized and measured in a frequency band of 45 MHz up to 26 GHz. The sensor enables the reduction of the uncertainty of the reflection coefficient measurements by approximately 40 times compared to a standard VNA reflection measurement and allows fast measurements with a VNA IF bandwidth of 30 kHz. The sensor is simple, cheap and mechanically stable with no movable parts.

Another structure of the sensor based on coupled line was suggested in [section 4.6](#). To decrease the unwanted reflections in the structure, it was necessary to design a four-port component – impedance transformer. The new, original design of the dual-mode microstrip impedance transformer, for the simultaneous matching of even- and odd-mode general impedances of a coupled line to a characteristic impedance of connected microstrip lines, was proposed in [section 4.5](#). A new dimension correction approach was derived. Two transformers between 50  $\Omega$  microstrips and microstrip coupled lines, with even/odd impedances 100 / 68  $\Omega$  and 36 / 27  $\Omega$ , respectively, were built. The concept was experimentally verified at a frequency band of 0.01–16 GHz.

The results attained in this thesis have opened a number of directions for future research. There are still many challenges in the area for which the author suggests future research as follows:

- As a part of the imaging sensor study, it can be verified whether it can detect material properties of the dielectric samples. A method for 1-port material property measurements can be derived;
- The final design of the interferometric advanced sensor using the dual-mode impedance transformer can be fabricated and experimentally verified by measuring samples with very high impedances.





## References

- [1] F. Griffiths and M. Ooi, "The fourth industrial revolution-industry 4.0 and iot [trends in future i&m]," *IEEE instrumentation & measurement magazine*, vol. 21, no. 6, pp. 29–43, 2018.
- [2] M. A. Kempin, "Design and analysis of an open-ended waveguide probe for material characterization," 2013.
- [3] M. R. Ramzi, M. Abou-Khousa, and I. Prayudi, "Near-field microwave imaging using open-ended circular waveguide probes," *IEEE sensors journal*, vol. 17, no. 8, pp. 2359–2366, 2017.
- [4] P. Mehta, K. Chand, D. Narayanswamy, D. G. Beetner, R. Zoughi, and W. V. Stoecker, "Microwave reflectometry as a novel diagnostic tool for detection of skin cancers," *IEEE Transactions on Instrumentation and Measurement*, vol. 55, no. 4, pp. 1309–1316, 2006.
- [5] K. M. Donnell, M. A. Abou-Khousa, M. Belayneh, and R. Zoughi, "Dual-loaded modulated dipole scatterer as an embedded sensor," *IEEE Transactions on Instrumentation and Measurement*, vol. 60, no. 5, pp. 1884–1892, 2011.
- [6] S. Kharkovsky, A. C. Ryley, V. Stephen, and R. Zoughi, "Dual-polarized microwave near-field reflectometer for non-invasive inspection of carbon fiber reinforced polymer (cfrp) strengthened structures," in *2006 IEEE Instrumentation and Measurement Technology Conference Proceedings*. IEEE, 2006, pp. 2108–2111.
- [7] M. A. Abou-Khousa, M. S. U. Rahman, and X. Xingyu, "Dual-polarized microwave imaging probe," *IEEE Sensors Journal*, vol. 19, no. 5, pp. 1767–1776, 2018.
- [8] M. A. Abou-Khousa, K. M. Shafi, and X. Xingyu, "High-resolution uhf near-field imaging probe," *IEEE Transactions on Instrumentation and Measurement*, vol. 67, no. 10, pp. 2353–2362, 2018.
- [9] O. Malyuskin and V. F. Fusco, "High-resolution microwave near-field surface imaging using resonance probes," *IEEE Transactions on Instrumentation and Measurement*, vol. 65, no. 1, pp. 189–200, 2015.
- [10] W. Saleh, N. Qaddoumi, and M. Abu-Khousa, "Preliminary investigation of near-field nondestructive testing of carbon-loaded composites using loaded open-ended waveguides," *Composite structures*, vol. 62, no. 3-4, pp. 403–407, 2003.
- [11] A. Hagelauer, M. Wojnowski, K. Pressel, R. Weigel, and D. Kissinger, "Integrated systems-in-package: Heterogeneous integration of millimeter-wave active circuits and passives in fan-out wafer-level packaging technologies," *IEEE Microwave Magazine*, vol. 19, no. 1, pp. 48–56, 2017.
- [12] S. M. Anlage, V. V. Talanov, and A. R. Schwartz, "Principles of near-field microwave microscopy," in *Scanning probe microscopy*. Springer, 2007, pp. 215–253.
- [13] A. P. Cracknell, *Ultrasonics*. London, U.K.: Wykeham, 1982.
- [14] M. Jagiella and S. Fericean, "Miniaturized inductive sensors for industrial applications," in

- SENSORS, 2002 IEEE*, vol. 2. IEEE, 2002, pp. 771–778.
- [15] K. Alzahrani, D. Burton, F. Lilley, M. Gdeisat, F. Bezombes, and M. Qudeisat, “Absolute distance measurement with micrometer accuracy using a michelson interferometer and the iterative synthetic wavelength principle,” *Optics express*, vol. 20, no. 5, pp. 5658–5682, 2012.
- [16] M. Norgia, G. Giuliani, and S. Donati, “Absolute distance measurement with improved accuracy using laser diode self-mixing interferometry in a closed loop,” *IEEE transactions on Instrumentation and Measurement*, vol. 56, no. 5, pp. 1894–1900, 2007.
- [17] K. Hoffmann and Z. Skvor, “Contactless distance measurement method,” in *77th ARFTG Microwave Measurement Conference*. IEEE, 2011, pp. 1–4.
- [18] K. Hoffmann, Z. Skvor, and M. Prihoda, “Precise microwave measurement of liquid level,” in *79th ARFTG Microwave Measurement Conference*. IEEE, 2012, pp. 1–2.
- [19] K. Hoffmann and Z. Skvor, “Microwave interferometric method for metal sheet thickness measurement,” in *81st ARFTG Microwave Measurement Conference*. IEEE, 2013, pp. 1–3.
- [20] Y. Venot and W. Wiesbeck, “76.5 ghz radar sensor for contact-free distance measurement with micrometer accuracy,” in *SENSORS, 2003 IEEE*, vol. 1. IEEE, 2003, pp. 216–221.
- [21] S. Scherr, S. Ayhan, B. Fischbach, A. Bhutani, M. Pauli, and T. Zwick, “An efficient frequency and phase estimation algorithm with crb performance for fmcw radar applications,” *IEEE Transactions on Instrumentation and Measurement*, vol. 64, no. 7, pp. 1868–1875, 2014.
- [22] N. Pohl, T. Jaschke, S. Scherr, S. Ayhan, M. Pauli, T. Zwick, and T. Musch, “Radar measurements with micrometer accuracy and nanometer stability using an ultra-wideband 80 ghz radar system,” in *2013 IEEE Topical Conference on Wireless Sensors and Sensor Networks (WiSNet)*. IEEE, 2013, pp. 31–33.
- [23] A. Schicht, K. Huber, A. Ziroff, M. Willsch, and L.-P. Schmidt, “Absolute phase-based distance measurement for industrial monitoring systems,” *IEEE Sensors Journal*, vol. 9, no. 9, pp. 1007–1013, 2009.
- [24] C. Rusch, S. Beer, and T. Zwick, “Ltcc endfire antenna with housing for 77-ghz short-distance radar sensors,” *IEEE Antennas and Wireless Propagation Letters*, vol. 11, pp. 998–1001, 2012.
- [25] S. Linz, F. Lurz, M. Sporer, S. Lindner, S. Mann, R. Weigel, and A. Koelpin, “Ultra-short-range, precise displacement measurement setup with a near field slot-line antenna and a dedicated spiral calibration,” in *2015 IEEE MTT-S International Microwave Symposium*. IEEE, 2015, pp. 1–4.
- [26] K. Haddadi, M. Wang, D. Glay, and T. Lasri, “A 60 ghz six-port distance measurement system with sub-millimeter accuracy,” *IEEE microwave and wireless components letters*, vol. 19, no. 10, pp. 644–646, 2009.
- [27] J. Barowski, M. Zimmermanns, and I. Rolfes, “Millimeter-wave characterization of dielectric materials using calibrated fmcw transceivers,” *IEEE Transactions on Microwave Theory and Techniques*, vol. 66, no. 8, pp. 3683–3689, 2018.
- [28] M. Zhao, J. D. Shea, S. C. Hagness, and D. W. van der Weide, “Calibrated free-space microwave measurements with an ultrawideband reflectometer-antenna system,” *IEEE microwave and wireless components letters*, vol. 16, no. 12, pp. 675–677, 2006.
- [29] N. Qaddoumi, H. Abiri, S. Ganchev, and R. Zoughi, “Near-field analysis of rectangular waveguide probes used for imaging,” in *Review of Progress in Quantitative Nondestructive*

- Evaluation*. Springer, 1996, pp. 727–732.
- [30] M. A. Abou-Khousa, S. Kharkovsky, and R. Zoughi, “Novel near-field millimeter-wave differential probe using a loaded modulated aperture,” *IEEE Transactions on Instrumentation and Measurement*, vol. 58, no. 5, pp. 1273–1282, 2009.
- [31] N. N. Qaddoumi, M. Abou-Khousa, and W. M. Saleh, “Near-field microwave imaging utilizing tapered rectangular waveguides,” *IEEE transactions on instrumentation and measurement*, vol. 55, no. 5, pp. 1752–1756, 2006.
- [32] G. C. Cho, H.-T. Chen, S. Kraatz, N. Karpowicz, and R. Kersting, “Apertureless terahertz near-field microscopy,” *Semiconductor science and technology*, vol. 20, no. 7, p. S286, 2005.
- [33] B. T. Rosner and D. W. Van Der Weide, “High-frequency near-field microscopy,” *Review of Scientific Instruments*, vol. 73, no. 7, pp. 2505–2525, 2002.
- [34] B. L. McLaughlin and P. A. Robertson, “Submillimeter coaxial probes for dielectric spectroscopy of liquids and biological materials,” *IEEE transactions on microwave theory and techniques*, vol. 57, no. 12, pp. 3000–3010, 2009.
- [35] S. Fabiani, D. Mencarelli, A. Di Donato, T. Monti, G. Venanzoni, A. Morini, T. Rozzi, and M. Farina, “Broadband scanning microwave microscopy investigation of graphene,” in *2011 IEEE MTT-S International Microwave Symposium*. IEEE, 2011, pp. 1–4.
- [36] R. J. Gutmann, J. M. Borrego, P. Chakrabarti, and M.-S. Wang, “Microwave scanning microscopy for planar structure diagnostics,” in *1987 IEEE MTT-S International Microwave Symposium Digest*, vol. 1. IEEE, 1987, pp. 281–284.
- [37] B. Feenstra, C. Vlahacos, A. S. Thanawalla, D. Steinhauer, S. Dutta, F. Wellstood, and S. M. Anlage, “Near-field scanning microwave microscopy: measuring local microwave properties and electric field distributions,” in *1998 IEEE MTT-S International Microwave Symposium Digest (Cat. No. 98CH36192)*, vol. 2. IEEE, 1998, pp. 965–968.
- [38] H. Tanbakuchi, F. Kienberger, M. Richter, M. Dieudonne, M. Kasper, and G. Gramse, “Semiconductor material and device characterization via scanning microwave microscopy,” in *2013 IEEE Compound Semiconductor Integrated Circuit Symposium (CSICS)*. IEEE, 2013, pp. 1–5.
- [39] A. Lewandowski, D. LeGolvan, R. A. Ginley, T. M. Wallis, A. Imtiaz, and P. Kabos, “Wideband measurement of extreme impedances with a multistate reflectometer,” in *2008 72nd ARFTG Microwave Measurement Symposium*. IEEE, 2008, pp. 45–49.
- [40] H. Bakli, K. Haddadi, and T. Lasri, “Interferometric technique for scanning near-field microwave microscopy applications,” *IEEE Transactions on Instrumentation and Measurement*, vol. 63, no. 5, pp. 1281–1286, 2014.
- [41] M. Randus and K. Hoffmann, “A simple method for extreme impedances measurement,” in *2007 70th ARFTG Microwave Measurement Conference (ARFTG)*. IEEE, 2007, pp. 1–5.
- [42] —, “A simple method for extreme impedances measurement-experimental testing,” in *2008 72nd ARFTG Microwave Measurement Symposium*. IEEE, 2008, pp. 40–44.
- [43] S. Gu, K. Haddadi, A. El Fellahi, G. Dambrine, and T. Lasri, “Measurement accuracy and repeatability in near-field scanning microwave microscopy,” in *2015 IEEE International Instrumentation and Measurement Technology Conference (I2MTC) Proceedings*. IEEE, 2015, pp. 1735–1740.

- [44] K. Haddadi, C. Brillard, G. Dambrine, and D. Théron, “Sensitivity and accuracy analysis in scanning microwave microscopy,” in *2016 IEEE MTT-S International Microwave Symposium (IMS)*. IEEE, 2016, pp. 1–4.
- [45] J. Reed and G. Wheeler, “A method of analysis of symmetrical four-port networks,” *IRE Transactions on Microwave Theory and Techniques*, vol. 4, no. 4, pp. 246–252, 1956.



## Author's Publications

### Papers in journals with impact factor:

- **A. Baskakova** and K. Hoffmann, "Design of Microstrip Dual-Mode Impedance Transformers," in *IEEE Microwave and Wireless Components Letters*, vol. 29, no. 2, pp. 86–88, Feb. 2019, doi: 10.1109/LMWC.2018.2887313. IF: 2.862
- **A. Baskakova** and K. Hoffmann, "Novel Waveguide Sensors for Contactless Ultrashort-Distance Measurements," in *IEEE Transactions on Microwave Theory and Techniques*, vol. 70, no. 1, pp. 565–575, Jan. 2022, doi: 10.1109/TMTT.2021.3107503. IF: 3.599
- **A. Baskakova** and K. Hoffmann, "W-Band Imaging Sensor Using a Rectangular Waveguide Structure With Choke," in *IEEE Microwave and Wireless Components Letters*, vol. 32, no. 3, pp. 230–233, March 2022, doi: 10.1109/LMWC.2021.3134472. IF: 2.862

### Conference papers:

- K. Hoffmann and **A. Baskakova**, "A new interferometric sensor for scanning near-field microwave microscopy," in *89th ARFTG Microwave Measurement Conference (ARFTG)*, Honolulu, HI, pp. 1–4, 2017;
- **A. Baskakova** G. Stella and K. Hoffmann, "An Interferometric Sensor for Scanning Microwave Microscopy Application," in *2018 Asia-Pacific Microwave Conference (APMC)*, Kyoto, Japan, pp. 1232–1234, 2018;
- **A. Baskakova** and K. Hoffmann, "Investigation of Waveguide Sensors for Ultra-Short-Distance Measurements," in *93rd ARFTG Microwave Measurement Conference (ARFTG)*, Boston, MA, pp. 1–4, 2019;

- 
- K. Hoffmann and **A. Baskakova**, "Simple sensors for ultra-short distance measurements," in *2019 European Microwave Conference in Central Europe (EuMCE)*, Prague, Czech Republic, pp. 158–161, 2019;
  - **A. Baskakova** , "Improved Time Efficiency for Simulation of an Antenna for Near-Field Distance Measurements in CST Studio Suite," in *2019 Antennas Design and Measurement International Conference (ADMInC)*, St. Petersburg, Russia, pp. 26–29, 2019.

## **Financial support acknowledgement:**

The research presented in the listed papers was conducted under financial support of:

- The European Union’s Horizon 2020 research and innovation programme 2016-2020 under the Marie Skłodowska-Curie grant agreement No. 675683.

## **Awards:**

Aleksandra Baskakova received an award for the best interactive forum paper “Investigation of waveguide sensors for ultra-short-distance measurements” presented at 93rd ARFTG Microwave Measurement Symposium, Boston, June 2019.

Aleksandra Baskakova won a competition at the CTU conference “Diplomka ve třech minutách” (Thesis in Three Minutes) English session, Prague, April 2021.

Aleksandra Baskakova

Ph. + 420 775179874

Email: [aleksandra.baskakova@fel.cvut.cz](mailto:aleksandra.baskakova@fel.cvut.cz)

## EDUCATION

---

- 2017 - Present**      **PhD student**  
*Czech Technical University in Prague, Prague, Czech Republic*  
Doctoral thesis: New Microwave Components for Distance and Imaging Measurement
- 2011 - 2013**      **Master of Science in Engineering and Technology**  
*Saint Petersburg Electrotechnical University «LETI», St. Petersburg, Russia*  
Master thesis: Tunable Microwave Filter with Constant Bandwidth

## RESEARCH AND WORK EXPERIENCE

---

- 2021 – Present**      **User Success Engineer**, Dassault Systèmes, Prague, Czech Republic
- 2017 – 2020**      **Early stage researcher**, Microwave measurement group, Department of Electromagnetic Field, Czech Technical University in Prague, Prague, Czech Republic
- 2018**      **Visiting researcher**, Ferdinand Braun Institut (FBH), Berlin, Germany
- 2013 – 2017**      **Researcher**, Microwave Microelectronics Laboratory, Microelectronics and Radioengineering Department, St. Petersburg Electrotechnical University “LETI”, St. Petersburg, Russia
- 2011 – 2012**      **Process engineer**, JSC "CSPA "LENINETZ", St. Petersburg, Russia

## PROJECT EXPERIENCE

---

- 2017 – 2020**      **Horizon 2020 Marie Curie ITN Project CELTA (Convergence of Electronics and Photonics Technologies for Enabling Terahertz Applications)**
- 2013 – 2017**      **Project “Broadband and electrically tunable microwave devices using active circuits and metamaterial transmission lines”; the program “Development of scientific research” The Ministry for Education and Science of the Russian Federation**
- 2013 – 2014**      **FP7 Marie Curie IRSES Project "MultiWaveS" (Multiband Electronically Reconfigurable Microwave Devices and Antennas for a New Generation of Wireless Systems)**

## INFORMATION TECHNOLOGY SKILLS

---

**Electromagnetic simulation:**      AWR Microwave Office, CST Studio Suite, Sonnet  
**CAD Processing**      SolidWorks

## LANGUAGES

---

**Russian:**      Mother Tongue  
**English:**      Fluent